Mémoire

Auteur : Snöink, Jakob
Promoteur(s) : De Becker, Michael
Faculté : Faculté des Sciences
Diplôme : Master en sciences spatiales, à finalité approfondie
Année académique : 2021-2022
URI/URL : http://hdl.handle.net/2268.2/14771

Department of Astrophysics, Geophysics and Oceanography
Faculty of Sciences
University of Liège

Investigation of the Galactic Magnetic Field based on the Radio Emission from Pulsars

Jakob Snöink

A thesis presented for the degree of
Master in Space Sciences

Supervisor:
Michaël De Becker

Reading Committee:
Dominique Sluse
Benoît Hubert
Valérie Van Grootel

5th June 2022

Academic year 2021-2022

Contents

Acknowledgements

First and foremost, I would like to thank my thesis supervisor Dr Michaël De Becker for his guidance and help in the creation of this thesis, but also for his help during the entire master's programme and especially the Erasmus exchange. Secondly, I thank the members of the Reading Committee, Dr Dominique Sluse, Dr Benoît Hubert, and Dr Valérie Van Grootel, for reading and reviewing this thesis.

Apart from people within the university, I must thank various others in the following.

Besonders möchte ich mich bei meiner Familie bedanken für die stetige Unterstützung und zum Teil auch Ablenkung während dieser schwierigen, aber auch spannenden Zeit. Ohne diese hätte ich es mit Sicherheit nicht, oder zumindest nicht auf diese Art, geschafft. Anna, Mama, Merle und Papa, danke für eure Unterstützung. Besonders in den Klausurenphasen habt ihr mich sehr unterstützt und zu Zeiten auch ‚ausgehalten'. Ich möchte mich auch bei meinen Großeltern herzlich bedanken.
Aufgrund der Pandemie und meines Studiums im Ausland war es oft schwierig persönlichen Kontakt zu halten. Ich muss mich auch besonders aus diesem Grund bei Anton, Hæn, Jannik, Julius, Katy, Lisa, Noah und Theresa bedanken. Die „Lockdown"-zeit wäre andernfalls noch deutlich schwieriger geworden. Aber auch das Zurückkommen nach Hannover nach teilweise fast einem Jahr wäre ohne euch nicht das Gleiche gewesen. Ich hoffe in Zukunft wird das Ganze etwas einfacher.
Außerdem muss ich mich bei den „besten ETechniker"n für die gemeinsame Zeit während des Bachelorstudiums und darüber hinaus bedanken. Ohne diese Gruppe wäre das Studium deutlich weniger unterhaltsam und vermutlich auch länger gewesen. Gleichzeitig möchte ich mich für die Zeit im GruLaLa bedanken. Ich habe nicht nur viel gelernt und meine eigenen Verständnislücken entdeckt, sondern auch sehr viel Spaß an der Arbeit im Labor gefunden.

Meine Erwägung, ein Masterstudium im Ausland überhaupt anzufangen wäre ohne meinen Aufenthalt in Oulu, Finnland undenkbar gewesen. Aus diesem Grund möchte ich mich hier bei Dr Lilge bedanken. Mein Auslandssemester in Finnland war nicht nur studientechnisch eine wichtige Erfahrung, sondern auch persönlich ein unbeschreibliches Erlebnis. Außerdem möchte ich die Bedeutung des Erasmus Austauschprogrammes generell betonen und kann die Teilnahme an diesem Programm jedem nur nahelegen. Der Ort spielt hierbei nicht die übergeordnete Rolle, aber ich kann aus eigener Erfahrung sagen, dass diese Erfahrung unersetzbar ist.
Obviously, when talking about my first Erasmus exchange, I must mention the irreplaceable group I got to know in Suomi. Especially the Norway Club will never be forgotten and is a prime example of what student exchange programmes are able to achieve at their best. Thank you to Adrien, Angelica, David, Felix, François, Lili, Maeva, Mojo, Pedro, and Samuel. Oulu became an incredible adventure because of you. On this note, I would also like to thank the University of Oulu for making this exchange happen and for providing great support for the exchange students as well as an excellent study environment. I must also thank Benjamin for providing me with the required information to finish my studies in Hanover as well as in Oulu at the same time.
Regarding my exchange at the Universitat de Barcelona, I would like to thank especially Andrei, Lorenzo, and Luis. Our hikes and trips, apart from starting quite early, were great adventures. I also want to thank all the other people I got to know during this stay. Moltes gracièss.
Finally, I come back to Liège where I was so lucky to meet the Aprigruties during the, for me, probably toughest time of the pandemic. Thank you, Angela, Arianna, Cosmin, Giovanni, Jimena, and Júlia for not

only making this period more enjoyable but also for becoming a magnificent group of friends. I also want to thank Emma, Lyen, Théo, and all the other people I got to meet in Liège.

Enfin, merci à l'Université de Liège de m'avoir accepté pour le programme de master en sciences spatiales.

Danke. Thanks. Merci. Kiitos. Gracias. Gràcies.

S'ha acabat el bròquil!

1 Introduction

A crucial step towards the understanding of our immediate environment beyond the Earth was the realisation that the Earth does not constitute the centre of everything. Not even of our 'own' Solar system. Its orbital movement around the Sun provides, simplified, the means to explain the other large bodies' motions within this system. This places the Sun at roughly the centre of the Solar system. Compared to our host galaxy, the Milky Way, the Sun with its planetary system is however only another, rather small, orbiting object. These interstellar scales are far more difficult to explore through space missions than our 'local' interplanetary scales. Insight into their features and properties nevertheless may directly affect us as we exist within this gigantic system. One way to uncover insights into our Galaxy's structure is the observation of pulsars.

The phenomenon of pulsars was first observed by Dame Jocelyn Bell Burnell in the form of "Unusual signals from pulsating radio sources" (Hewish et al., 1968) for which her supervisor won the Nobel Prize for Physics in 1974 (Nobel Prize Outreach AB 2022.).
As an illustrative first analogy for the perception of the emission of a pulsar, one may consider a light house. The light beam is rotated with an inclination, in this case 90°, with respect to the light house's axis of rotation. The result of this rotational configuration is the perception of the emitted light as consecutive pulses from the observer's point of view which may be accredited entirely to the geometrical arrangement. In the case of a pulsar, the basic geometrical configuration is similar, but several other effects play a significant role as well. Pulsars as objects may be described as rotating neutron stars. These compact stellar remnants result from the collapse of the core of massive stars at the end of their evolution, when they explode as supernovae. Some of the known young pulsars can even be directly connected to recordings of these events as for the probably most famous case of the Crab pulsar whose supernova explosion was reportedly observed by Asian astrologers as far back as 1054 A.D. (see e.g., Clark and Stephenson, 1977; Green and Stephenson, 2003). For known pulsars, pulse periods lie in the range between 1.5 ms to 11 s. The large mass and small radius allow indeed for a rotation as fast as 1000 revolutions/s in the most extreme cases. Since they encompass strong magnetic fields of strengths up to 10^{15}G with huge electric fields close to their surface, pulsars are capable to efficiently accelerate charged particles. Charged particles may thus gain ultrarelativistic energies, leading to an electron-positron pair production avalanche and eventually the observed radiation beam (Manchester, 2004). The highly relativistic nature of the participating particles leads to a strong relativistic beaming with an opening cone depending on the Lorentz factor as depicted in Fig. 1 (De Becker, 2021b).
According to the so-called standard model for the radio emission from pulsars, another peculiarity of radiation by pulsars may be mentioned as its coherent nature, resulting from a group of N electrons, moving coherently and therefore acting as a charge of N times the single electron's charge. The enhancement of the radiated power according to Larmor's formula[1] becomes N^2 compared to a single electron and N compared to the radiated power by N electrons in the incoherent case like for more conventional synchrotron radiation (De Becker, 2021b).

Despite the appearance of their radiation as relatively periodic as may be seen in Fig. 2, pulsars continuously lose energy. This energy loss results in a gradual increase of their spin period. Thanks to this property, their age and magnetic field strength may be obtained. Typical values for the period and its derivative are $P \sim 1\,\mathrm{s}$ and $\dot{P} \sim 10^{-15}$ respectively. These values imply pulsar ages between 10^6 and 10^7yrs, and surface magnetic field strengths of the order of 10^{12}G (Manchester, 2004).

[1] In short, Larmor's formula states that the power radiated by an accelerated charged particle is proportional to the acceleration of the particle squared and to the charge of the particle squared.

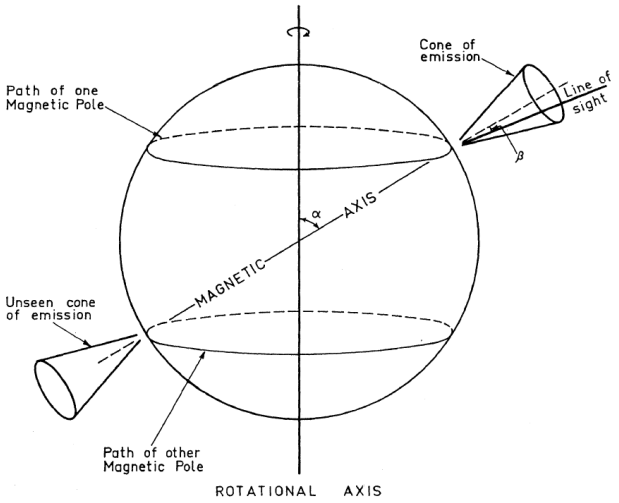

Figure 1: Representation of a pulsar model (Radhakrishnan and Cooke, 1969).

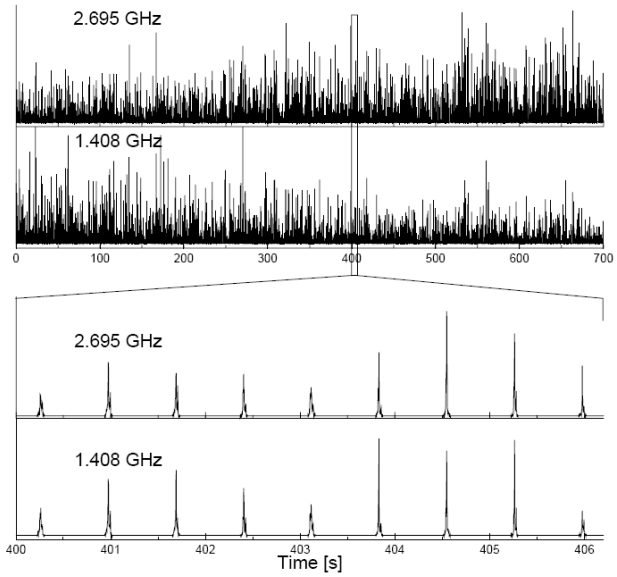

Figure 2: Total power time series of single pulses of PSR B0329+54 measured at 1.4 GHz (Jodrell Bank) and 2.7 GHz (Effelsberg). Top two panels show an 11-min long interval. The long time scale intensity variations between the two telescopes are caused by interstellar scintillation. Bottom two panels show a close-up of a few pulses. Off-pulse regions have been zeroed for clarity. A very good overall correlation is obvious (Karastergiou et al., 2001).

The study of pulsar radiation is particularly useful due to its property of often being highly polarised (Manchester, 1972; Noutsos et al., 2008). Furthermore, radio pulsar may be described as "perfect point sources" (Schnitzeler et al., 2016). The use of these properties is further discussed in section 2.3.2.
Lastly, pulsars are generally distributed throughout the whole Galactic disk (Noutsos et al., 2008). The distribution of "normal" pulsars is found to peak at galactocentric radii of around 4 kpc (Manchester, 2004). This may be compared to the generally assumed galactocentric radius of around 8.5 kpc for the Solar position.

1.1 Pulsar catalogue

Regarding pulsars, the Australia Telescope National Facility (ATNF) catalogue[2] poses as possibly the most extensive collection of well-ordered data. This work does largely make use of this catalogue and a brief description concerning its properties is provided in the following. The details are mainly taken from the

[2] https://www.atnf.csiro.au/research/pulsar/psrcat/

original publication, namely Manchester et al. (2005).
The catalogue contains all spin-powered pulsars, as well as anomalous X-ray pulsars, and soft gamma-ray repeaters in case they show coherent pulsed emission. It does however not include accretion-powered systems. This omission is on the one hand due to their wide range of often unstable periods, and on the other hand due to the existence of other catalogues with a focus on these sources. The included sources are either only powered by their rotational energy or may have an additional source to enable their large luminosity. The additional source does generally not lead to a strong deviation of their properties compared to 'normal' pulsars for the included sources.

The prior catalogue includes 558 radio pulsars (Taylor et al., 1993) and functions as a basis for the ATNF catalogue. As the result, the ATNF catalogue encompassed at the time of Manchester et al. (2005) 1509 pulsars.

In the catalogue, 67 different pulsar parameters are pre-defined and additional ones may be added. Furthermore, most values are listed with their corresponding error. Notably, the distance estimation may be given some further attention. By default, it is derived using the measured Dispersion Measure as discussed in section 2.1 in combination with a model for the Galactic distribution of free electrons as described in section 2.1.1. The availability of a parallax measurement for the regarded source results in the distance parameter being set by its inverse value. The next lower priority is given to distance estimates with associations with another object or measurements of absorption by neutral hydrogen and a model for the differential rotation of the Galaxy. Lastly, if the previous method only provides distance limits, two options are available. In case the distance estimate using the default method lies between the distance limits, the default value is used. If it does not lie in this range, the value of the nearest limit is chosen. This procedure in theory results in the best possible estimate but should not be overlooked when using the data.
Galactocentric coordinates (XX, YY, ZZ) are given in a right-handed system with the solar position at $(0.0, 8.5\,\mathrm{kpc}, 0.0)$. The ZZ axis is directed toward the north Galactic pole.

All pulsars in the catalogue have names based on J2000 coordinates. They are gathered from published papers and freely available for research purposes. Fig. 3 shows all included pulsars in version 1.66 of the catalogue, published on 11/01/2022. This corresponds to a number of 3282 sources. A representation of the included sources as function of the respective month and year, including already version 1.67, is shown in Fig. 4.

The strong increase in their number may notably be attributed to the first observation of the Fast Radio Burst (FRB) dubbed phenomenon in 2007 by Lorimer et al. (2007) and their confirmed abundance as extragalactic objects in 2013. The rise in observational interest in these phenomena also benefited the discovery of pulsars. A notable collection of FRB sources is the CHIME/FRB catalogue (Petroff et al., 2022; CHIME/FRB Collaboration et al., 2021).

Observations of pulsars rely strongly on the radio domain as e.g., the recorded series of pulses in Fig. 2, and the ATNF pulsar catalogue show. These enable on the one hand the investigation of properties of the pulsar itself, notably the surface dipolar magnetic field at the equator, source age, and spin-down luminosity by only using the pulses' period and its rate of change (Kaspi and Kramer, 2016), and on the other hand the study of the pulses' travelled path, i.e., the Interstellar Medium, in particular the Galactic Magnetic Field (Manchester, 2004). The latter is at the core of this work for which the key physical concepts are outlined in the following section.

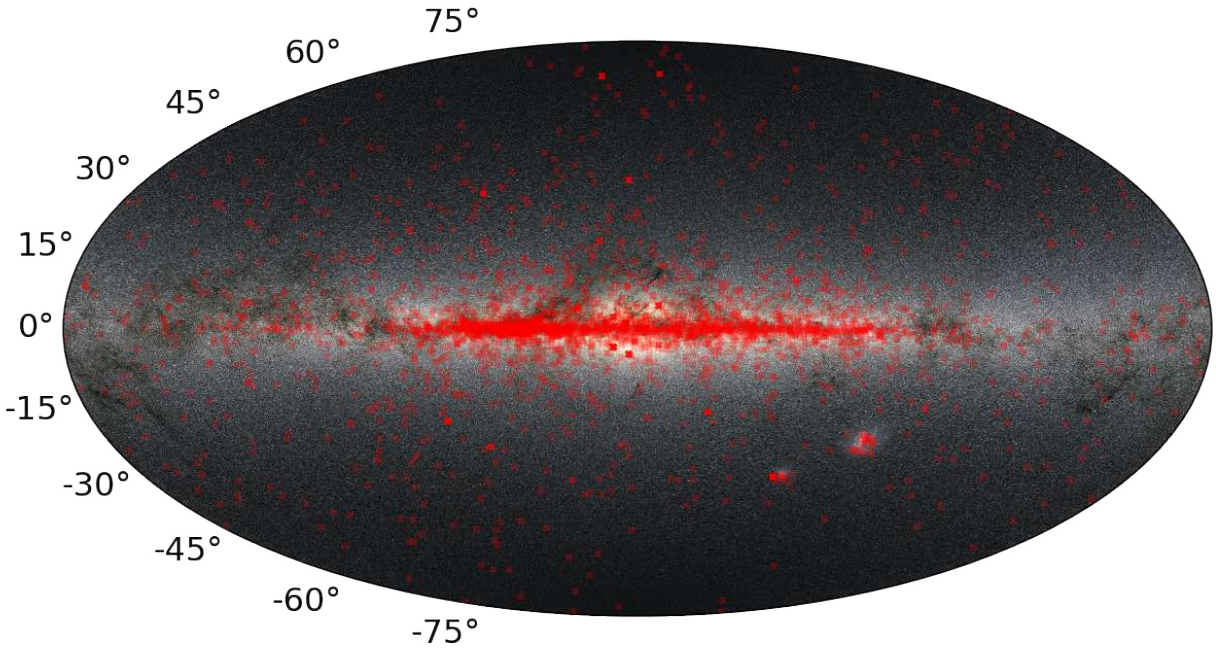

Figure 3: Galactic distribution of pulsars from the ATNF catalogue (Manchester et al., 2005) in galactic longitude and latitude. The background image is modified from an image by NASA/JPL-Caltech/R. Hurt (SSC/Caltech).

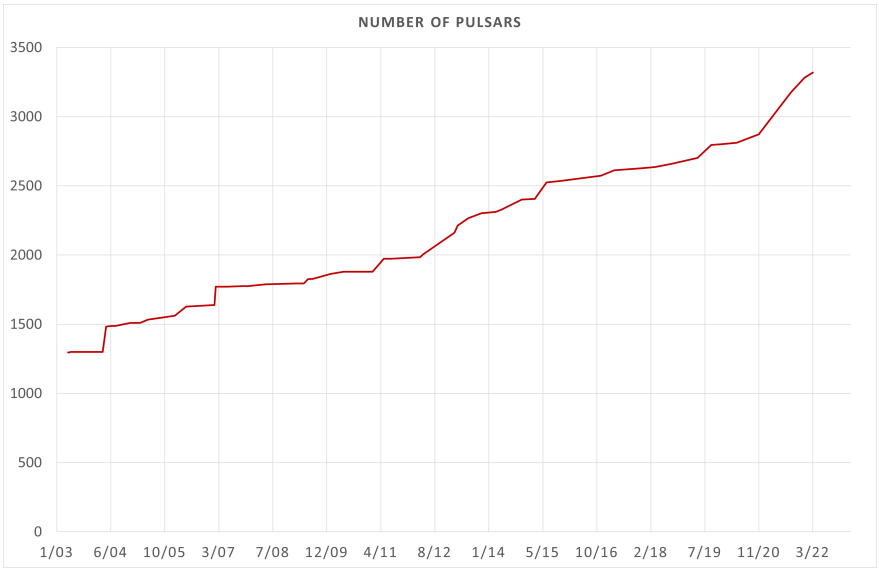

Figure 4: Number of included sources in the ATNF pulsar catalogue as function of the corresponding month and year.

2 Physical concepts

This section provides the physical base of this work. Key quantities regarding the study of the Interstellar Medium (ISM) with a focus on pulsars are introduced, finalised by the motivation of this thesis.

2.1 Dispersion Measure (DM)

In general, dispersion when talking about electromagnetic waves describes the phenomena of dependency of the index of refraction on the frequency (Feynman et al., 2015). Radio waves as electromagnetic waves can be described as an oscillating electric and magnetic field which interacts with the charged particles in the ISM through electrostatic interactions which in turn leads to a delay in the propagation of light as a function of the frequency and the mass of the charged particles. Photons at higher frequencies go past the free electrons without being strongly affected in terms of their velocity, whereas photons at lower frequencies are more delayed. Furthermore, the delay due to electrons is much more significant than the delay caused by protons due to their mass difference of the order of 2,000 (Swinburne University of Technology). An illustrative example of the different contributions to the delay is depicted in Fig. 5.

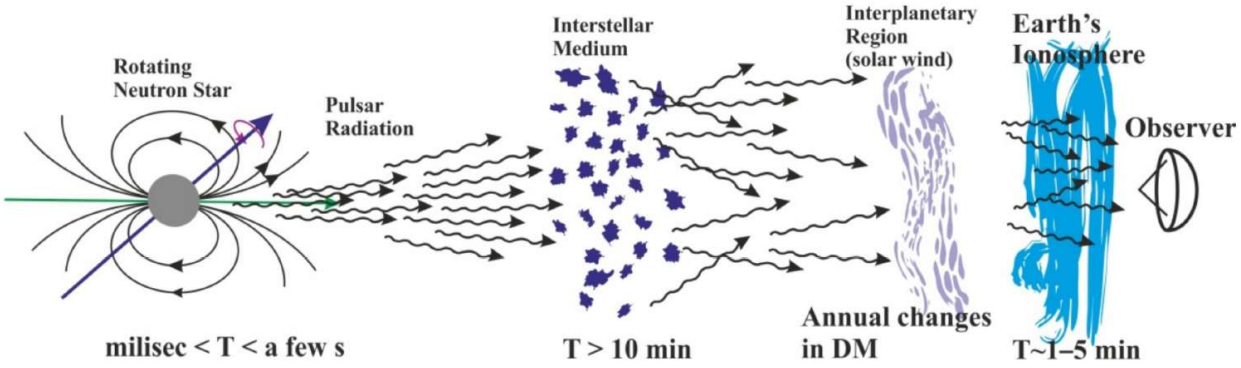

Figure 5: The pulsar radio wave signal is generated in the region of neutron star magnetosphere. The signal propagates through interstellar matter, where the phenomena of dispersion and scattering occur (Błaszkiewicz et al., 2020).

The speed at which a pulse of radiation containing a band of frequencies propagates through space is given by the group velocity v_g and may be defined as the partial derivative of the angular frequency, $d\omega$, over the partial derivative of the wave number, dk. It can be obtained, using the effect of dispersion (Bradt, 2008).

As a starting point for its derivation, one may use the following assumptions. Firstly, a time and space dependence of the variations according to Eq. 1 is chosen.

$$e^{i(\vec{k}\vec{r}-\omega t)} \tag{1}$$

Additionally, the effect of ions is neglected due to their significantly lower mobility with respect to electrons resulting from their mass difference as mentioned earlier. To simplify and demonstrate the general dependencies, an isotropic plasma with no external magnetic field is assumed. The previous assumptions are then included in Maxwell's equations, including the charge and current densities, ρ and $\vec{j}$ respectively, due to the plasma. This basis allows the derivation of the Dispersion Measure DM in the following way.
The velocity vector $\vec{v}$ of a single electron in this environment may be obtained from Newton's law in Eq. 2.

Here, $\vec{E}$ denotes the electric field which exerts a force on the electron with electric charge e and mass m (Rybicki and Lightman, 1979).

$$m\dot{\vec{v}} = -e\vec{E} \tag{2}$$

The velocity vector thus takes the form shown in Eq. 3 with i being the imaginary unit and ω the angular frequency as seen in the time and space dependence in Eq. 1 (Rybicki and Lightman, 1979).

$$\vec{v} = \frac{e\vec{E}}{i\omega m} \tag{3}$$

This derivation can then be introduced into the definition of the current density $\vec{j}$ as $\vec{j} = -ne\vec{v}$, leading to Eq. 4 with the conductivity σ (Rybicki and Lightman, 1979).

$$\vec{j} = \frac{ine^2}{\omega m} \cdot \vec{E} = \sigma\vec{E} \tag{4}$$

Introducing this relation into the equation of charge conservation, $-i\omega\rho + i\vec{k}\vec{j} = 0$ with $\vec{k}$ being the wavenumber vector, results in Eq. 5 (Rybicki and Lightman, 1979).

$$\rho = \frac{\sigma}{\omega} \cdot \vec{k} \cdot \vec{E} \tag{5}$$

The definition of the conductivity σ according to Eq. 4 may then be introduced into the definition of the dielectric constant, $\varepsilon \equiv 1 - \frac{4\pi\sigma}{i\omega}$, which in turn yields Eq. 6 (Rybicki and Lightman, 1979). In this equation, ω_p represents the plasma frequency which can be defined as the plasma's resonant frequency which is clearly related to the electron density n. Its mathematical definition is given in Eq. 7.

$$\varepsilon = 1 - \frac{4\pi ne^2}{\omega^2 m} = 1 - \frac{{\omega_p}^2}{\omega^2} \tag{6}$$

$$\omega_p = \sqrt{\frac{4\pi ne^2}{m}} \tag{7}$$

An exemplary value for the plasma frequency in the interstellar environment, using the typical value of $0.03\,\mathrm{cm}^{-3}$ for the electron density, would be $\omega_p = 2\pi \cdot 1.56\,\mathrm{kHz}$ (Burke et al., 2019).
According to Maxwell's equations with the definitions and derivations of the different quantities and conditions above, $\vec{k}$, $\vec{E}$, and $\vec{B}$, the magnetic field vector, are orthogonal which results in the relation $c^2k^2 = \varepsilon\omega^2$. Inserting Eq. 6 into this equation yields a relation between the wavenumber k, angular frequency ω, and plasma frequency ω_p according to $k = \frac{1}{c}\sqrt{\omega^2 - \omega_p^2}$. For the case of $\omega < \omega_p$, the wavenumber thus becomes imaginary, resulting in an exponential decrease of the wave's amplitude. The plasma frequency may therefore also be called the plasma cutoff frequency, below which no wave propagation is possible. An exemplary use of this phenomena is the ionosphere as a tool to communicate over larger distances due to its reflecting nature below the cutoff frequency. Above the plasma cutoff frequency, the electromagnetic wave undergoes refraction where the index of refraction, η_r, comes into play. It may be defined as the square root of the

dielectric constant which supports the necessity to pursue the previous derivations. The previously defined group velocity, v_g, may be obtained using the form of the wavenumber given before and thus becomes equal to Eq. 8 which is always smaller than the speed of light, c (Rybicki and Lightman, 1979).

$$v_g = c \cdot \sqrt{1 - \frac{\omega_p^2}{\omega^2}} \tag{8}$$

In case of a variable electron density in the considered medium, the radiation takes curved paths compared to straight lines for no such variations. Its motion depends on the index of refraction and thus on its frequency. From the derivation of the group velocity, the dependence on the frequency can be clearly seen. Since it describes the velocity at which the wave's energy and modulation travels, different arrival times for different frequencies directly arise. Mostly, the regarded frequency is significantly larger than the plasma frequency, $\omega \gg \omega_p$. This allows for an expansion of the inverse of the group velocity as shown in Eq. 9, followed by an integration along the path d according to Eq. 10. These steps lead to arrival times according to Eq. 11 where the first term corresponds to the vacuum and the second term to the plasma correction (Rybicki and Lightman, 1979).

$$v_g^{-1} \approx \frac{1}{c}\left(1 + \frac{1}{2}\frac{\omega_p^2}{\omega^2}\right) \tag{9}$$

$$t_p = \int_0^d \frac{ds}{v_g} \tag{10}$$

$$t_p \approx \frac{d}{c} + \left(2c\omega^2\right)^{-1} \int_0^d \omega_p^2 ds \tag{11}$$

In practice, the measured quantity usually corresponds to the rate of change in arrival time with frequency as given by Eq. 12 (Rybicki and Lightman, 1979). It illustrates the impact of the dispersive effect on the arrival time of pulses of electromagnetic radiation as a function of the angular frequency ω. Notably, arrival times increase for pulses of lower frequency which is expressed by the negative sign.

$$\frac{dt_p}{d\omega} = -\frac{4\pi e^2}{cm\omega^3} \cdot DM \tag{12}$$

The Dispersion Measure, DM, in this relation may be defined as the integral over the electron number density, n, along the path travelled by the radiation as given in Eq. 13 (Kulkarni, 2020).

$$DM = \int_0^d n ds \tag{13}$$

Thus, the measurement of this quantity provides an estimation about the electron number density along the line of sight.

Instead of estimating the electron number density, it is possible to use the measured DM in combination with a model of the Galaxy's free electron density distribution, like the *YMW16* model (Yao et al., 2017), to obtain an indication for the pulsar's distance according to DM $= n_e D$ where D represents the distance to the pulsar

(Swinburne University of Technology). However, one must be careful in the disregard of other contributors to the observed dispersion in the chosen frequency range like ions, temperature, or magnetic fields which may lead to a dependency of the dispersive delay on the frequency as well as on the polarisation, and relative motion. The discussion of these effects is out of the scope of this work, and it is referred to Kulkarni (2020) for a detailed review which mainly concerns the observation of the sources, in this case pulsars.

2.1.1 Galactic free electron distribution

The following description concerning models of the Galactic free electron distribution, if not indicated differently, is mainly taken from Yao et al. (2017).

A model of the distribution of free electrons in our galaxy, the Milky Way, provides the possibility of estimating the distances to pulsars through the measurement of the DM in their signal. The components of the model may be obtained through observations of different Galactic components including the distribution of molecular gas and star-formation regions, Hα surveys of local gas, which imply the presence of a "thick" electron disk with a scale height of around 1.5 kpc, and HII regions, which may be interpreted as a "thin" disk component with a scale height of around 70 pc. The models must be calibrated to the observations which is mainly done through the fitting to several pulsars with **independently** determined distances and DM. These distances may be obtained through pulsar parallaxes, associations of the pulsar with globular clusters or supernova remnants (through astrometry or photometry), optical observations of the binary companion (requires an optically identified companion star), or kinematic distances using a Galactic rotation model and absorption spectra.

One of the first attempts to model the Galactic distribution of free electrons is the *LMT85* model (Manchester and Taylor, 1981; Lyne et al., 1985). The authors use two components in their model, namely a thin disk with a decreasing electron number density n_e with Galactocentric radius in the mid-plane, divided in one component with a scale height of around 70 pc, and a second z-independent component where z represents the Galactic coordinate orthogonal to the disk. As an additional component, they take the Gum Nebula which shows a significant modification of the DMs of the pulsar signals from behind it. The model is calibrated with 36 pulsars with independent distances. A newer model is the so called *TC93* model (Taylor and Cordes, 1993; Cordes et al., 1991) which adds the effect of the spiral structure and makes use of more independent distances (74). In addition, and as a result, it takes the dependence of the pulsar's DM on Galactic longitude into account. The authors also use observations of interstellar scattering. The two components, thin disk and thick disk, have a $sech(z)^2$ dependence for the z-component, which imitates the exponential dependence but prevents a cusp at x = 0, and a radial dependence of the electron number density. Finally, the prior model to the used model in this study is the *NE2001* model (Cordes and Lazio, 2002, 2003). This model uses 112 independent distances and scattering measures for 269 pulsars. It provides a "quasi-smooth" distribution of free electrons with large-scale variations in the strength of fluctuations due to interstellar scattering. The authors make use of a combination of several components, namely a thin axisymmetric disk, a thick axisymmetric disk, spiral arms, local components like a local arms, a local hot bubble, and relatively hot "super-bubbles", overdense components like the Gum Nebula, the Vela supernova remnant, the Galactic Loop I, and a small region around the Galactic Centre (GC), clumps to account for pulsars with excess DM or scattering, and voids to take pulsars with DMs below the predicted value from a quasi-smooth distribution into account. Furthermore, they use a $sech(z)^2$ dependency.

The used model (*YMW16* (Yao et al., 2017)), as depicted in Fig. 6, uses the same basic structure as *TC93*

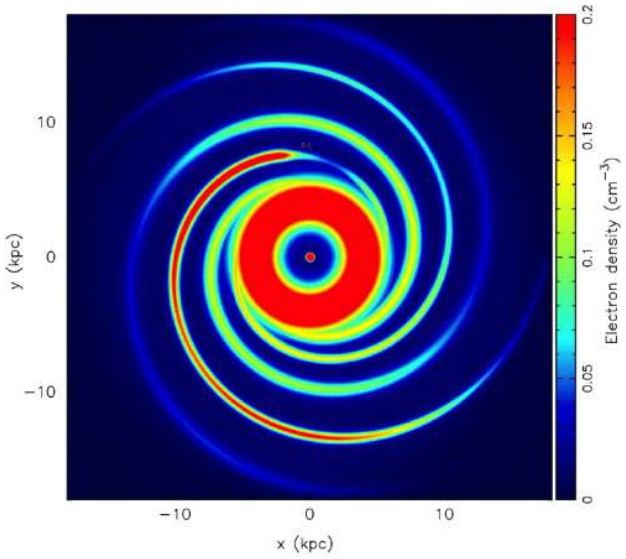

Figure 6: Electron density in the Galactic plane ($z = 0$) for the *YMW16* model. The Galactic Centre is at the origin and the Sun is at $x = 0$, $y = +8.3$ kpc (Yao et al., 2017).

and *NE2001* for the Galactic part. In addition, the authors include a four-armed spiral pattern plus a local arm. Furthermore, several components are added or modified, namely the Local Bubble with two regions of higher electron number density, the Gum Nebula, Loop I, a region of higher electron number density in the Carina arm, and a region of reduced electron number density in the Sagittarius tangential region. They fit the model to 189 independent distances without using observations of interstellar scattering since the effect is usually dominated by few regions with very high electron number density fluctuations which are not feasible to model. No clumps or voids are added, opposite to *NE2001*, but features that are implied by the measurement of several pulsar DMs are included. The Large and Small Magellanic Cloud are accounted for using geometric information and measurements of 27 pulsars. Components for the intergalactic medium and host galaxy are also included for the analysis of Fast Radio Bursts (FRBs). The different properties of the Galaxy are implemented as follows. The thick disk is modelled with a plane-parallel disk with a scale height of around 1600 pc which may be interpreted as the widely distributed "warm ISM" and ellipsoidal cavities near the GC to account for the "Fermi Bubbles" which are thought to be the result of powerful winds from the GC region evacuating large bubbles. Secondly, the thin disk is implemented with a scale height of around 65 pc, representing the "molecular ring", a region of high gas density and massive star formation with a Galactocentric radius of around 4 kpc. The spiral arms follow a logarithmic spiral pattern with an overdense region in the Carina arm and an underdense region in the Sagittarius arm. Next, the GC disk, a region of high-density ionised gas, with a radius of around 160 pc. The next feature is the Gum Nebula which is modelled with an ellipsoidal shell in the z-direction. The Local Bubble region, a relatively low-density cavity around the Sun, is implemented as a cylinder with two regions of enhanced electron density on its boundary. Finally, Loop I is accounted for by a spherical shell with a spherical cap for the ionisation. The result of combining the different components is a model with a high degree of symmetry where the electron number density is dominated by the GC disk and the thin disk component in the inner Galaxy, by the spiral arms in the outer Galaxy, and by the thick disk at high latitudes. Furthermore, an asymmetry is introduced through the spiral arms. All Galactic disk components in this model follow a $sech(z/H)^2$ z-dependence where H is the scale height and show a $sech(R)^2$ cut off at Galactocentric radius $R = 15$ kpc with a scale length of 2.5 kpc. Finally, the model provides the means to determine 95% of the Galactic pulsar distances with a relative error below 0.9, and is estimated to be around 50% better than the *NE2001* model and around 100%

better than the *TC93* model for distances based on the DM.

2.2 Rotation Measure (RM)

A single charge involved in synchrotron radiation radiates elliptically polarised radiation which is either right or left handed depending on whether the line of sight is inside or outside the cone of maximal radiation. Since many particles with a smooth distribution over the pitch angle are involved in the process of radiation, the elliptical component cancels out and the radiation is partially linear polarised (Rybicki and Lightman, 1979). It may be reminded that linear polarisation is observed for pulsar emission (Burke et al., 2019).

The passage of an electromagnetic wave through a magnetised plasma results in a change in the orientation of its polarisation plane (Beck, 2007) as depicted in Fig. 7. This so called Faraday rotation in general describes the rotation of the electric-field vector of a linearly polarised wave. The position angle θ when travelling through a magnetised plasma (Klein and Fletcher, 2015) is given as a function of the wavelength λ (Weisberg et al., 2004). The name derives from its discoverer who published the phenomenon in Faraday (1846).

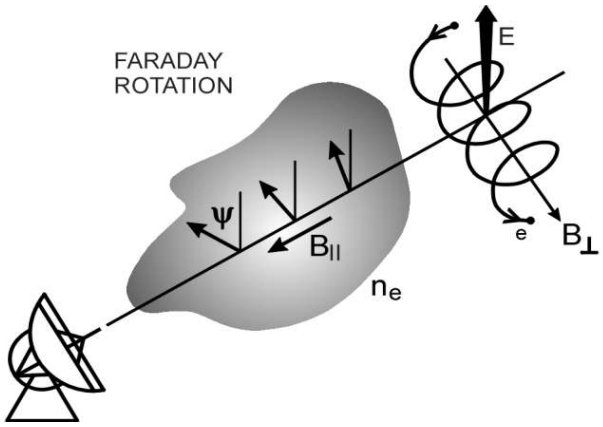

Figure 7: Synchrotron emission and Faraday rotation. Modified from Beck and Wielebinski (2013).

The presence of an external magnetic field influences the movement of charges (Rybicki and Lightman, 1979). In this case, the Lorentz force on a free charge in a magnetic field forces the charge, e.g., a free electron, onto a helical path. The three corresponding forces in this case are the centrifugal, electrical, and Lorentz force which may be defined according to Eq. 14, 15, and 16 respectively (Klein and Fletcher, 2015).

$$\vec{F_c} = -m\omega^2\vec{r} \tag{14}$$

$$\vec{F_{el}} = e \cdot \vec{E}\,(\vec{r}, t) \tag{15}$$

$$\vec{F_L} = \pm\frac{e}{c} \cdot \omega \cdot B_{\parallel} \cdot \vec{r} \tag{16}$$

Linearly polarised waves are a superposition of circularly polarised waves of opposite directions which is represented with the + and − for the right-hand and left-hand circularly polarised wave respectively in the definition of the Lorentz force in Eq. 16. The resulting equation of motion is shown in Eq. 17 and the corresponding path vector $\vec{r}$ in Eq. 18 (Klein and Fletcher, 2015).

$$-m\omega^2\vec{r} = \pm\frac{e}{c}\cdot\omega B_{\parallel}\vec{r} + e\vec{E}\left(\vec{r},t\right) \tag{17}$$

$$\vec{r} = -\frac{e}{m}\left(\frac{1}{\omega^2 \pm \omega\omega_c}\right)\vec{E} \tag{18}$$

This development allows the definition of the cyclotron frequency ω_c according to Eq. 19 (Klein and Fletcher, 2015) which thus corresponds to the gyration of one electron around the magnetic field lines (Rybicki and Lightman, 1979).

$$\omega_c = \frac{eB_{\parallel}}{mc} \tag{19}$$

Due to the present magnetic field, the definition of the dielectric constant in Eq. 6 changes and takes the form as shown in Eq. 20. It may be noted that the two definitions are equal for a line of sight component of the magnetic field equal to zero (Klein and Fletcher, 2015). Thus, the presence of a magnetic field line of sight component and the property of a planar polarised wave being the superposition of a right handed and left handed polarised wave results in a rotation of the wave's plane of polarisation, or Faraday rotation (Rybicki and Lightman, 1979).

$$\varepsilon_{R,L} = 1 - \frac{\omega_p^2}{\omega\left(\omega \pm \omega_c\right)} \tag{20}$$

The corresponding rotation depends on the travelled path and may be obtained by the integral, $\phi_{R,L} = \int_0^d k_{R,L} ds$ where the wavenumber $k_{R,L}$ is given by $k_{R,L} = \frac{\omega}{c}\sqrt{\varepsilon_{R,L}}$. This development yields a rotation equal to $\Delta\theta = \frac{|\phi_R - \phi_L|}{2}$. If one then assumes a frequency significantly larger than the plasma frequency as well as the cyclotron frequency, the equation for the wavenumber becomes equal to Eq. 21. The rotation thus takes the simpler form shown in Eq. 22 (Rybicki and Lightman, 1979).

$$k_{R,L} \approx \frac{\omega}{c}\left(1 - \frac{\omega_p^2}{2\omega^2}\left(1 \mp \frac{\omega_c}{\omega}\right)\right) \tag{21}$$

$$\Delta\theta = \frac{1}{2}\int_0^d \left(k_R - k_L\right) ds = \frac{2\pi e^3}{m^2c^2\omega^2}\int_0^d nB_{\parallel} ds \tag{22}$$

Measurements of the Faraday rotation thus provide the means to probe the magnetic field line of sight component in case the electron density n_e and the distance to the source are known (Han et al., 2006). For this purpose, one may define the *Rotation measure*, RM, as in Eq. 23 where a positive value of the magnetic field line of sight component corresponds to an orientation towards the observer (Schnitzeler et al., 2016). Since the rotation angle depends on the squared wavelength of the regarded radiation (Weisberg et al., 2004), long waves are rotated the most while high-frequency waves are basically unaffected (Noutsos, 2012).

$$RM\left(radm^{-2}\right) = 0.81\int_{\text{source}}^{\text{observer}} n_e\left(cm^{-3}\right) B_{\parallel}\left(\mu G\right) dl\left(pc\right) \tag{23}$$

Since the measurements are usually conducted from the ground, the radiation has to pass through the Earth's atmosphere and is thus affected by its population of free electrons, notably in the ionosphere. This leads to an additional rotation of the polarisation plane which is time and position dependent due to the highly dynamic atmospheric environment. The effect has to be taken into account and subtracted from the measurements. One possibility are continuous Faraday rotation measurements towards geostationary satellites (Sobey et al., 2019). Exemplary values for the RM in the ISM compared to the ionosphere are $60\,\mathrm{radm}^{-2}$ and $0.8\,\mathrm{radm}^{-2}$ respectively (Klein and Fletcher, 2015). It may be noted that the effect due to the atmosphere is typically one order of magnitude smaller than the effect due to the ISM.

Another source of rotation is the pulsar's magnetosphere which is expected to be mainly populated by electron-positron pairs and to co-rotate with the neutron star in the inner region. However, its contribution is rather small for pulsars with large RMs (Gueroult et al., 2019).

2.3 Galactic magnetic field (GMF)

Magnetic fields affect the ISM in several different ways. Some examples are mentioned in the following. They contribute to the total pressure which balances the ISM against gravity, affect gas flows in different galactic components, are essential for the onset of star formation by removing angular momentum from protostellar clouds during their collapse, enable the distribution of energy from supernova explosions in the ISM, and are responsible for the density and distribution of cosmic rays in the ISM (Beck, 2007). Furthermore, processes like magnetic reconnection may heat the ISM and the halo gas, influencing the thermal structure of the galaxy. In addition, magnetic fields play an important role in the dynamics of the spiral arms (Beck and Wielebinski, 2013).

2.3.1 Alternative methods

Several other techniques exist for the determination of the GMF in addition to pulsar measurements. The most prominent ones are briefly introduced in the following, including the corresponding most important discoveries regarding the GMF. It should be noted that the following list of techniques is non-exhaustive. A brief summary of the described techniques including their advantages and disadvantages as well as dependencies is shown in Fig. 8.

The first discussed method is starlight polarisation. Initially non-polarised starlight passes through regions of magnetically aligned dust and becomes linearly polarised as the result (Clemens et al., 2012). The observations are in general related to magnetic fields in clouds where dust is more present. In addition to scattering, the dust grains also have an absorbing effect. Radiation from sources farther away thus suffers from larger extinction as well as larger polarisation (Han, 2013). This technique only provides information on the field orientation but not on its sign (Heiles, 1996). Thus, information on the orientation of the transverse magnetic field in the ISM in proximity of the Sun can be obtained (Han et al., 2006), i.e., in the sky plane. In case of several stars in proximity of a cloud, it is also possible to obtain information on the magnetic field orientation in the cloud. However, since many clouds are present in the Galactic disk, the technique does not allow for an association deep inside the disk. Therefore, this method is not feasible for probing the large-scale magnetic structure in the disk but may be used for halo fields (Han, 2013).
Thanks to this method, the existence of a magnetic field aligned along the Galactic plane is found. Furthermore, the magnetic field's configuration towards the Galactic Anticenter, around Galactic longitudes of 140°, is constrained. The region is found to be very homogeneous concerning the alignment with the Galactic disk

Observable	GMF Property Probed	Dependencies	Pros	Cons
Starlight polarization	$B_\perp$ orientation	dust grain properties and distribution	3D information	sampling limited to a few kpc
Faraday rotation (extragalactic)	$B_\parallel$ direction and strength	thermal electron density	good full-sky sampling (42k sources); full LOS through Galaxy	no 3D info along LOS
Faraday rotation (Galactic)	$B_\parallel$ direction and strength	thermal electron density	3D sampling along the LOS through the Galaxy	mostly in Galactic plane; currently insufficient sampling (1k)
Faraday tomography (extragalactic)	$B_\parallel$ direction and strength	thermal electron density	probes variations along the LOS through the Galaxy	low physical resolution, not a probe of the Milky Way
Faraday tomography (Galactic)	$B_\parallel$ direction and strength	thermal electron density	probes variations in 3D along the LOS	no physical distances associated with Faraday depth variations
Diffuse synchrotron emission (radio)	$B_\perp$ orientation and strength (squared)	cosmic-ray density; thermal electron density	goes as $\lvert\mathbf{B}\rvert^2$; full-sky coverage; probes turbulent Faraday effects	no 3D info along LOS; polarization horizon of a few kpc due to Faraday depolarization effects
Diffuse synchrotron emission (microwave)	$B_\perp$ orientation and strength (squared)	cosmic-ray density	goes as $\lvert\mathbf{B}\rvert^2$; full-sky coverage; full LOS through the Galaxy; no Faraday rotation	no 3D info along LOS; total intensity contaminated by Bremsstrahlung and AME.
Diffuse dust emission	$B_\perp$ orientation	dust grain density, properties, environment, and alignment	full-sky coverage; full LOS through the Galaxy; 3D information with extinction surveys (e.g., Gaia) no Faraday rotation	probes only close to Galactic plane $\lvert z\rvert \lesssim 100\,\mathrm{pc}$

Figure 8: Table 1 from Jaffe (2019), showing the tracers of the large-scale GMF with their pros, cons, and dependencies

with high polarisation values. A well aligned magnetic field is also noticed along the 'North Polar Spur' up to Galactic longitudes of around 30°. Lastly, the magnetic field inside dense molecular clouds is constrained to the order of a few mG (Beck and Wielebinski, 2013).

Another technique makes use of spectral lines with Zeeman splitting. This effect occurs in the presence of a magnetic field where a single spectral line is split into three components. The separation of the different lines is determined by the energy separation of the "sub-sublevels". These levels are identified by the so-called magnetic quantum number which in turn is determined by the magnetic field strength. The prior description is also referred to as the "normal Zeeman effect". The non-observation of a central line when looking along the magnetic field on the other hand is referred to as the "longitudinal Zeeman effect" as depicted in Fig. 9. It may also be noted that the separation between different lines depends on the squared wavelength, resulting in a greater effect for longer wavelengths (Robinson, 2007). Since the effect largely relies on the presence of spectral lines, it is frequently used in high-mass star-formation regions to probe the magnetic field (Vlemmings, 2008). This technique may be used to detect the line of sight strength of magnetic fields (Han et al., 2006). Furthermore, completely split emission lines give insights into the total magnetic field strength (Han, 2017). Insights into the direction of the field component along the line of sight may also be obtained. A major limitation stems from the fact that the method is only sensitive to fields inside clouds or clumps, corresponding to scales of pc or even AU (Han, 2013).

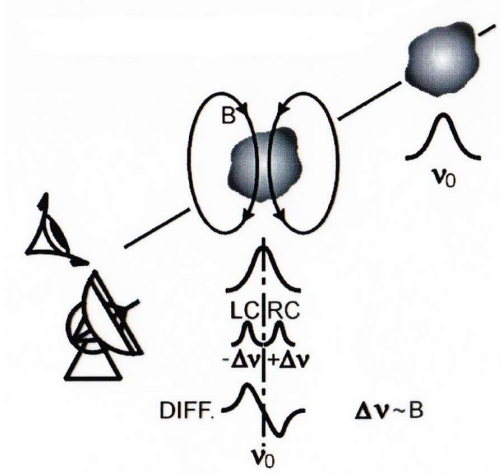

Figure 9: The longitudinal Zeeman effect, splitting of a spectral line into two components with opposite circular polarisation (Beck and Wielebinski, 2013).

A notable application is the environment of HI gas clouds. Thereby, the mean total field in the cold neutral interstellar gas is constrained to approximately $6 \pm 2\,\mu\text{G}$. This finding implies that the magnetic field dominates over the thermal motion in these regions. It is however in equipartition with the turbulences (Beck and Wielebinski, 2013).

The background synchrotron radiation from our galaxy may also be used to draw information on the magnetic field. It is the result of mainly cosmic ray electron interactions with the GMF. This radiation is intrinsically linear polarised orthogonal to the magnetic field. Its observation thus provides information on the orientation of the orthogonal magnetic field component in the sky plane. Complications arise from the fact that the magnetic field is mostly not well ordered and emissions due to the small-scale irregular magnetic field are completely depolarised (Han, 2017). The depolarisation increases even more for lower frequencies (Han, 2013). In case the emission region also contains organised magnetic fields, a partial polarisation is achieved. Furthermore, the observations must also be corrected for Faraday rotation (Han, 2017). Using this approach,

one may obtain information on the transverse direction of the magnetic field specific to the emission region as well as an approximation of its strength (Han et al., 2006). The method allows for an estimation of the magnetic field in the halo. This is however difficult in the Galactic disk due to the presence of many emission regions and the arising complication of separating these (Han, 2013).

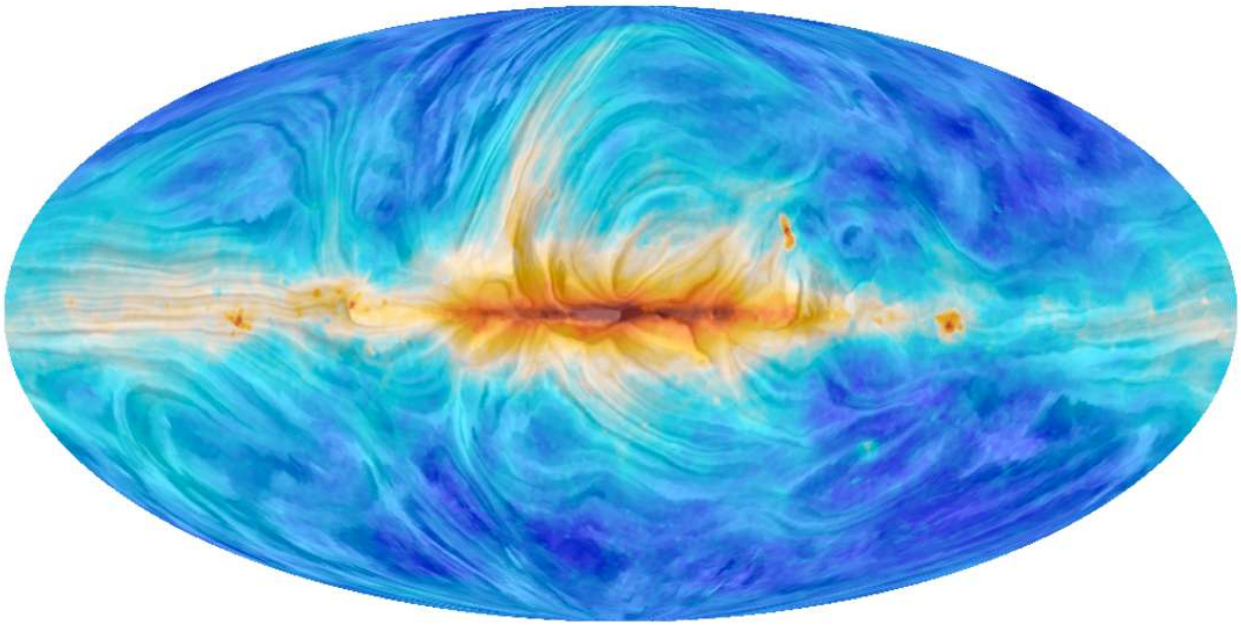

Figure 10: All-sky view of the angle of polarisation at 30 GHz, rotated by 90° to indicate the direction of the GMF projected on the plane of the sky. The colours represent intensity, dominated at this frequency by synchrotron emission (Planck Collaboration et al., 2016).

Measurements of the total synchrotron emission allow the derivation of the equipartition strength of the total field. The values in the local neighbourhood are found as $6 \pm 2\,\mu$G. Whereas the strength at the smaller Galactocentric radius of 3 kpc corresponds to $10 \pm 3\,\mu$G (Beck, 2001). The larger values are in general expected for smaller radii. In addition, an exponential scale length of the total field is found as approximately 12 kpc (Beck and Wielebinski, 2013). The Voyager 1 spacecraft noticed a smooth increase in the field strength when entering interstellar space. The measured emission corresponds to a field strength of $4.8 \pm 0.4\,\mu$G (Burlaga and Ness, 2016). It may be noted that this value is close to the derived equipartition value. The previously described findings utilise measurements of the total synchrotron emission which introduces the difficulty of separation between thermal and non-thermal radiation. The following findings are done eliminating this complication by using linear polarised emission. An arising complication of this method is the, in section 2.2 described, Faraday rotation which must be considered in order to obtain physical results. Towards the so called "Fan region" ($l \approx 140°, b \approx 10°$), a polarisation maximum is found. In this region, the line of sight lies perpendicular to the local spiral arm. Several signatures of expanding supernova remnants are observed through their compressing effect on the magnetic field. One of them is the "North Polar Spur" around the Galactic longitude of 30°. Furthermore, small-scale effects like turbulences in the polarisation intensity are seen towards the inner Galaxy ($90° > l > -90°, |b| < 30°$). These effects point to Faraday effects on small scales. Observations by the Planck satellite allow a visualisation of the data as can be seen in Fig. 10. Thus, it is expected that most magnetic field indicators are related to large-scale features like distant loops or filaments. The fields are relatively organised. Observations of the GC imply rather strong fields as well as a

more complex structure. One feature are the so called "strings". These indicate vertical magnetic structures, compared to the largely aligned field along the Galactic plane (Beck and Wielebinski, 2013). Measurements of the magnetic field strength in the central region differ quite significantly. For instance, the radio synchrotron spectrum indicates strengths of 50 to 100 µG (Crocker et al., 2010), whereas Zeeman splitting of OH masers imply values as high as 2 to 4 mG (Yusef-Zadeh et al., 1996).
Ferrière (2009) takes observations of external galaxies into account. These have the immediate advantage of probing the magnetic field under different angles and notably face-on. Thereby, an approximately poloidal magnetic field close to equipartition with cosmic rays is expected. The strength of this large-scale field should be of the order of 10 µG. The large values of the order of 1 mG are anticipated for rather localised filaments. Furthermore, similarly high values are derived for dense interstellar clouds with a largely horizontal magnetic field orientation. Finally, Schnitzeler et al. (2016) obtain a small inclination angle of around 12° for the large-scale magnetic field in the central region with respect to the plane of the sky.

Another technique concerns polarised thermal emissions from dust grains in clouds. The aligned dust grains possess a typical temperature of the order of few tens to few hundred kelvins. As a result, polarised thermal radiation in the mm to far-infrared range is emitted. The polarisation is linear with the electric field vector along the long axis of the dust grain (Han, 2017). The technique is applied to detect the transverse orientation, i.e., orthogonal to the line of sight, of magnetic fields in molecular clouds (Han et al., 2006). Probing the large-scale magnetic field is not possible with this method because the field orientations of all clouds are aligned with, i.e., parallel to, the Galactic plane (Han, 2013).

Finally, one may make use of supernova remnants. These expand into the surrounding medium. This expansion results in a compression of the tangential component of the local magnetic field with respect to the shell. The increased magnetic field strength poses as the source of synchrotron radiation. Thereby, information on the orientation of the magnetic field may be obtained (Jaffe, 2019).
West et al. (2016) derived the presence of an off-plane, vertical component of the GMF. It may be however noted that the discovery could also be connected to a yet unknown property of supernova remnants.

Many of the previously described techniques make extensive use of the presence of clouds. A major limit of them arises directly from the missing knowledge and/or association of these clouds. This applies especially to the Galactic disk as explained before.

2.3.2 Pulsars as probes of the Galactic Magnetic Field

The ratio between the two previously in sections 2.1 and 2.2 described quantities of the DM and RM respectively, provides the means to estimate an 'electron-density-weighted average magnetic field strength' and its net direction parallel to the line of sight. This ratio may be defined according to Eq. 24, where n_e represents the electron density and dl the differential distance element. RM is defined with positive values for a net direction of the average magnetic field towards the observer and with negative values for the opposite case (Sobey et al., 2019). It may be however noted that this 'simple' formula does only apply in case the assumption of the magnetic field strength and the electron density not being correlated holds. In case of a correlation between the two quantities, the value of $\langle B_{\parallel} \rangle$ is overestimated and the anti-correlated variations are underestimated (Beck and Wielebinski, 2013). Notably, the two quantities may be assumed to be uncorrelated for low densities $\left(\lesssim 10^{-3}\mathrm{cm}^{-3}\right)$ (Passot and Vázquez-Semadeni, 2003).

$$\langle B_{\parallel} \rangle = \frac{\int_0^d n_e B_{\parallel}\, dl}{\int_0^d n_e\, dl} = 1.232\,\mu\mathrm{G} \cdot \left(\frac{\mathrm{RM}}{\mathrm{rad} \cdot \mathrm{m}^{-2}} \right) \left(\frac{\mathrm{DM}}{\mathrm{pc} \cdot \mathrm{cm}^{-3}} \right)^{-1} \tag{24}$$

The availability of RMs and DMs along similar line of sights also allows to probe the magnetic field on a smaller scale. In this case, the quotient of the difference in RMs over the difference in DMs comes to use according to Eq. 25. Here, $d0$ and $d1$ represent the path to the nearer and farther pulsar respectively. The differences are written as $\Delta RM = RM_{d1} - RM_{d0}$ and $\Delta DM = DM_{d1} - DM_{d0}$. The major additional advantage of this technique is the independence of the electron density model. It must be however noted that the derivation of the distance through the DM introduces a dependence on the model (Han, 2017).

$$\langle B_{\parallel} \rangle_{(d0-d1)} = 1.232\,\mu\mathrm{G} \cdot \frac{\Delta RM}{\Delta DM} \tag{25}$$

As a third option, the use of linear trends in the RM with distance may be taken. This technique is notably introduced by Han et al. (2018). Pulsars along similar line of sights are selected and the average magnetic field parallel to the line of sight is calculated from the fitted RM values. This technique allows for an "averaging" over small-scale features of the ISM and thus provides the means to probe the large-scale GMF.

In addition to the use of pulsars inside the Milky Way, extragalactic radio sources may also provide useful insight into the GMF. As explained in section 2.2, several environments contribute to the observed RM. Concerning the use of extragalactic radio sources, the influences from the intergalactic space, intervening galaxies, interplanetary space, and the ionosphere is generally assumed to be rather small. The latter contribution may also be subtracted from the measurements by utilising known RMs. As the result, one is left with only intrinsic and Milky Way contributions (Beck and Wielebinski, 2013). Notably, a study by Schnitzeler (2010) finds the Rotation Measurements being dominated by the Milky Way's contribution at low Galactic latitudes of 1 to 10°. Complications for extragalactic sources arise from the fact that different measurements may refer to the same object but different regions, e.g., the lobe or the nucleus of a radio galaxy. Thus, observations must be used with care concerning the observed region (Beck and Wielebinski, 2013).

A brief description of insights into the GMF using Galactic pulsar RMs is provided in the following. An early study by Manchester (1974) makes use of RMs in the local arm. Thereby, the longitudinal component is found to be uniform on large scale. More precisely, it shows the same sense and strength out to 1 kpc from the Sun. Values are obtained to correspond to $2.2 \pm 0.4\,\mu\mathrm{G}$ as well as a direction towards the Galactic longitude of $94° \pm 11°$. The direction indicates a clockwise oriented magnetic field viewed from the Galactic North Pole for the local region. Thomson and Nelson (1980) make use of a larger number of RMs. In so doing, a reversal in direction towards the inner spiral arm is found. A more recent value from pulsar measurements for the regular field in the local spiral arm corresponds to $1.4 \pm 0.2\,\mu\mathrm{G}$ (Beck and Wielebinski, 2013). Considering an even larger number of RMs, Lyne and Smith (1989) find that the field at smaller Galactocentric radius, i.e., closer to the GC, shows reversed orientations and enhanced strength. Measurements of pulsars in the inner Norma arm show strengths of the regular magnetic field around $4.4 \pm 0.9\,\mu\mathrm{G}$ (Beck and Wielebinski, 2013). Furthermore, the use of extragalactic sources, e.g., towards the Galactic Anticenter, suggests more reversals in the outer parts of the Galaxy.

Through observations towards the GC, Roy et al. (2008) obtain the highest value of the RM in that direction of $|RM| \approx 1000\,\mathrm{radm}^{-2}$. RMs towards the GC are in general mostly found to be positive. This implies a field

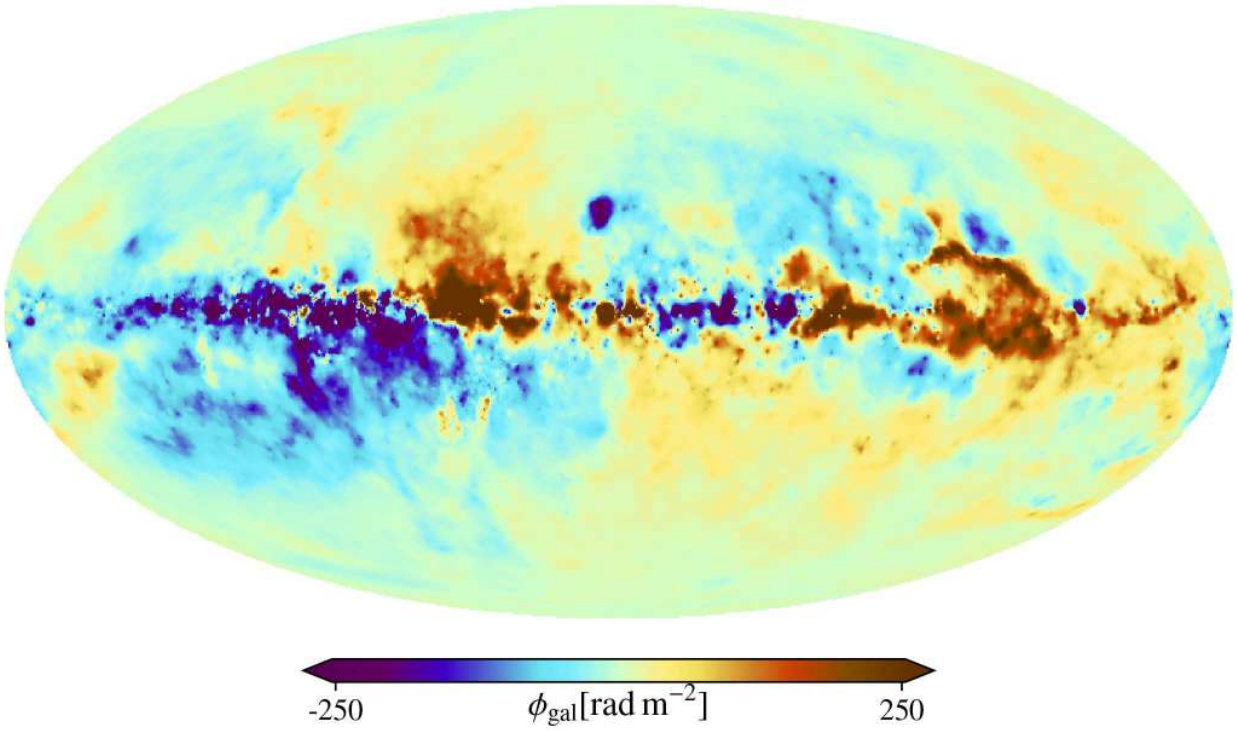

Figure 11: All-sky map of rotation measures in the Milky Way, constructed from the RM data of 55190 polarised extragalactic sources of the VLA NVSS survey and many other catalogues. Red: positive RMs, blue: negative RMs (Hutschenreuter et al., 2022). Galactic longitude 0° (Galactic Centre) is in the map centre. Galactic longitude increases from right to left, Galactic latitude increases from bottom to top (Beck and Wielebinski, 2013).

aligned with a possible central bar. As seen in Fig. 11, the RMs towards the inner Galaxy ($-60° < l < 60°$) and away from the Galactic plane show opposite signs above and below the plane, as well as west and east of the centre (Beck and Wielebinski, 2013). At approximately the same region, Predehl et al. (2020) derived the existence of two bubbles of hot gas. These are observed in X-ray and expand to ± 14 kpc above and below the GC (Beck and Wielebinski, 2013). Lastly, Shanahan et al. (2019) find values of the RM at the tangent of the Sagittarius arm as high as 4219 radm^{-2}.

Large-scale reversals of the GMF are found between the local Carina-Orion arm and the outer Perseus arm, as well as in the inner Scutum-Crux-Sagittarius arm around $R \approx 1 - 2$ kpc (Beck and Wielebinski, 2013). In total, 6 to 8 such reversals are expected between the arm and interarm regions of the Milky Way (Han et al., 2018). Large HII regions also result in field reversals. These are however on a smaller scale (Mitra et al., 2003) but may affect observations in certain regions significantly. In those cases, observations do not provide significant insight into the large-scale magnetic field (Nota and Katgert, 2010).

2.3.3 Models

Since it is not possible to determine the complete Milky Way magnetic field structure, one must make use of models. These may then be compared to the properties obtained through the observed tracers, e.g., RMs (see e.g., Brown et al., 2007; Han et al., 2018) or starlight polarisation (see e.g., Heiles, 1996; Frisch et al., 2012). Taking the assumption that the Galaxy is not unique but resembles other spiral galaxies in the

observable universe, one may use observations of those galaxies to make general assumptions on the Milky Way's magnetic field structure. Concerning external galaxies, the interested reader may be referred to Beck and Wielebinski (2013) for a thorough review. Furthermore, insights into the Galactic structure and its dynamics may be utilised as constraints. In the following, a short, non-exhaustive introduction into GMF models is provided. Reviews of different GMF models and techniques are provided in e.g., Kachelrieß et al. (2007); Jansson and Farrar (2012a); Jaffe (2019).

Starting with the most obvious feature of spiral galaxies like the Milky Way, one may assume a general, large-scale spiral structure as the basis of the GMF. Here, three different configurations are considered which divide the models into three categories. First, the axisymmetric spiral (ASS) with symmetry under rotation by π around the GC. Secondly, the bisymmetric spiral (BSS) with an anti-symmetry under rotation by π around the GC. Lastly, the mixed spiral structure (MSS) as a combination of the former two (Van Eck et al., 2011). Detailed descriptions of the three models can be found in Beck et al. (1996). It may be noted that there is no proof for a 'simple' BSS or ASS configuration (Men et al., 2008). A more recent form of the disk magnetic field is described in Brown et al. (2007) and is in parts based on the *NE2001* (Cordes and Lazio, 2002, 2003) thermal electron density model (Jansson and Farrar, 2012a). In this GMF model, the disk field is constrained to the x-y-plane and only defined for the Galactocentric radii between 3 kpc and 20 kpc. The inner region, $3\,\mathrm{kpc} \leq r \leq 5\,\mathrm{kpc}$, represents the "molecular ring" with a purely azimuthal field configuration. In the remaining section, $5\,\mathrm{kpc} \leq r \leq 20\,\mathrm{kpc}$, eight logarithmic spiral regions constitute the large-scale regular field. Here, the field strength decreases as the inverse of the radius (Jansson and Farrar, 2012a).

The previously described models cover only the disk magnetic field. To get a more realistic and complete description of the GMF, one must however include more components. Jansson et al. (2009) show that the disk and halo field may be separated and to study the two contributions individually. In fact, they even obtain a better fit for the GMF using this approach. Jansson and Farrar (2012a) thus assume a purely toroidal azimuthal component to represent the halo magnetic field. They notably obtain better results than for an axisymmetric or bisymmetric spiral. Furthermore, it may be noted that the magnetic field amplitudes in their model differ in the northern and the southern part of the Galaxy.

In addition to the disk and halo fields, another out-of-plane component may be included. This component resembles an X-shape away from the plane (Krause, 2007) and may thus be dubbed "X-field" component. The magnetic field configuration can be assumed as axisymmetric and poloidal, i.e., without any azimuthal component (Jansson and Farrar, 2012a). Despite the disk, halo, and "X-field" components which can be considered as large-scale components, one should also consider more random field configurations. The two commonly chosen additional configurations are on the one hand the small-scale random fields (see e.g., Haverkorn et al., 2008; Jaffe, 2019) and on the other hand a "striated"/ordered random field (see e.g., Jansson and Farrar, 2012a; Jaffe et al., 2010)

Exemplary configurations for the three types of fields are shown in Fig. 12. The small-scale random field is expected to be due to e.g., supernovae or outflows with a coherence length $\lambda \lesssim 100\,\mathrm{pc}$ (Haverkorn et al., 2008; Ma et al., 2020) and poses as a simplification of the ISM's turbulences (Jaffe, 2019). Coherence length in this context describes the scale over which the field appears spatially ordered (Arshakian et al., 2009). In comparison, the large-scale field's coherence length may be assumed to be between $\sim$1 and 10 kpc (Ma et al., 2020). An entirely homogeneous magnetic field thus corresponds to the extreme case of an infinitely large coherence length (Pais et al., 2020). The "striated" random fields present an orientation along some axis over large scale with varying strength and sign/orientation on small scale. These variations may be

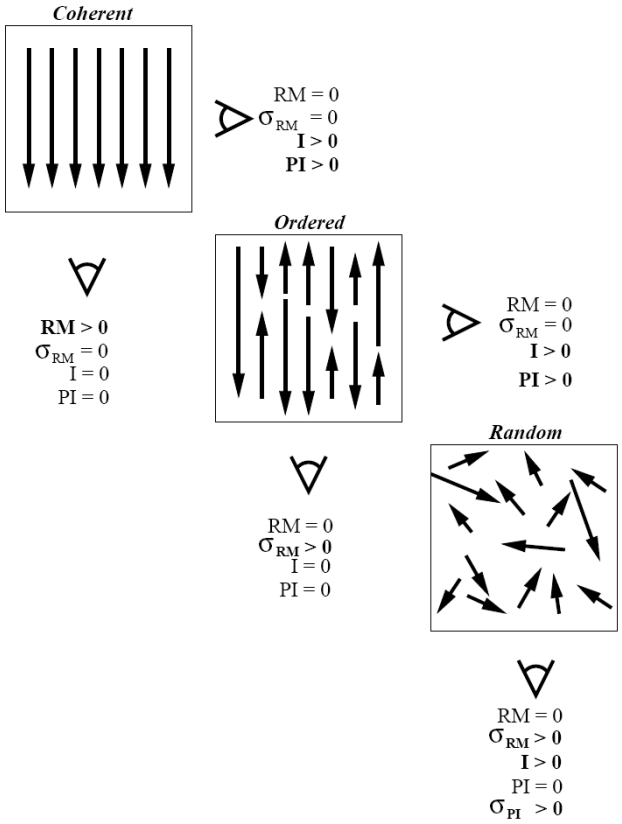

Figure 12: Cartoon illustrating the three components of the magnetic field and how they relate to the three observables of total synchrotron intensity (I), polarised synchrotron intensity (PI) and the Faraday RM (Jaffe et al., 2010).

attributed to bubbles of hot plasma which carry trapped, randomly oriented fields away from the disk, to differential rotation of small scale random fields, or to both. Thus, the latter field component is assumed to be everywhere aligned with the large-scale field as well as having the same relative magnitude everywhere (Jansson and Farrar, 2012a).

Following the definition of the different field components, one ends up with a fitted GMF configuration as depicted in Fig. 13. The disk field is shown in the upper part. The innermost arrow represents the magnetic field in the molecular ring region whereas the remaining arrows correspond to the spiral arm regions. Moreover, two slices of the toroidal halo field at $z \pm 1\,\mathrm{kpc}$ representing the northern and southern hemisphere respectively are shown in the lower part of Fig. 13. Notably, a larger extent of the field in the southern hemisphere is observed. Due to the added toroidal halo and "X-field", an asymmetry in the disk field arises. Furthermore, large-scale reversals between the Scutum Crux and the Perseus arm as well as between the Perseus and Norma arm may be observed. It may be noted that the molecular ring field mainly results from the halo and "X-field". Lastly, the "X-field" causes the GMF in the x-y-plane to have a varying pitch angle with radius (Jansson and Farrar, 2012a).

The described model certainly presents a simplification of the GMF and predictions concerning regions far away from the Solar position should be taken very carefully (Jansson and Farrar, 2012a). For instance, Moss et al. (2012) find a possible significant difference between the two sides of the Galactic disk in terms of GMF configuration notably due to dynamo action with long term reversals. In addition, the short-scale random field component is expected to be of approximately the same order as the large-scale field. Therefore, RM fluctuations across the Galactic plane may be observed and require improved constraints on the GMF.

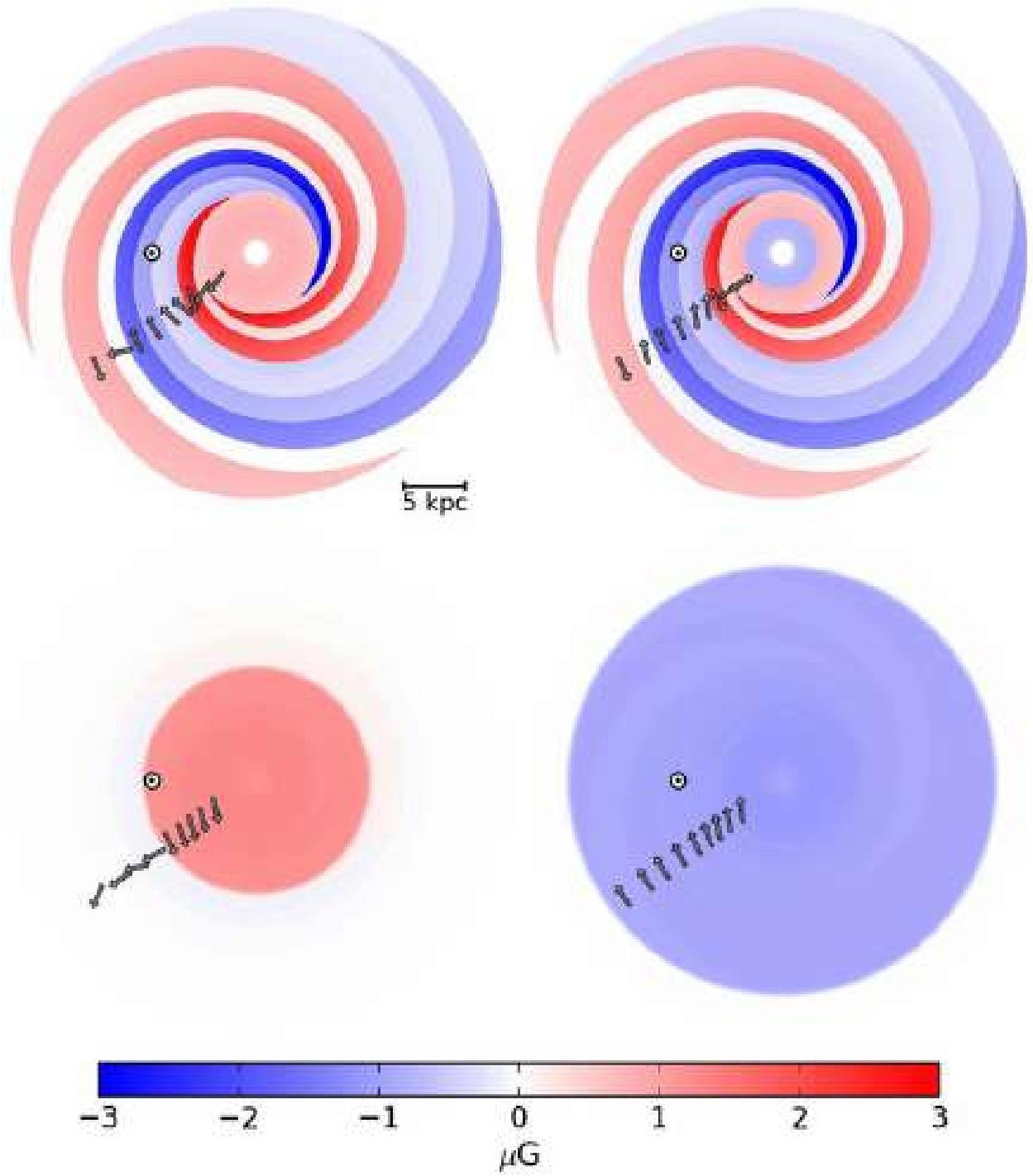

Figure 13: Top view of slices in the x–y plane of the GMF model. Top row, from left, slices at $z = 10\,\mathrm{pc}$ and $z = -10\,\mathrm{pc}$. Bottom row, slices at $z = 1\,\mathrm{kpc}$ and $z = -1\,\mathrm{kpc}$, respectively. The colour scheme shows the magnitude of the total regular field, with negative values if the azimuthal component is oriented clockwise. The location of the Sun (in arm number 5) at $x = -8.5\,\mathrm{kpc}$ is marked with a circle. From the top panels it is clear that the magnetic field just above and below the mid-plane are very similar, but not identical, due to the superposition of the z-symmetric disk field component with the z-asymmetric toroidal halo component. At $|z| = 1\,\mathrm{kpc}$ the field is dominated by the halo component, but still exhibits signs of the superposition with the X-field, and even the disk field (Jansson and Farrar, 2012a)

Regional anomalies of the ISM like the Gum Nebula or North Polar Spur also result in a deviation from the smooth RM variations. Finally, uncertainties in pulsar distances further complicate the derivation of the GMF (Noutsos et al., 2008). It is thus clear that further constrains on the GMF are required to improve existing and potential new models. Some exemplary models are shown in Fig. 14.

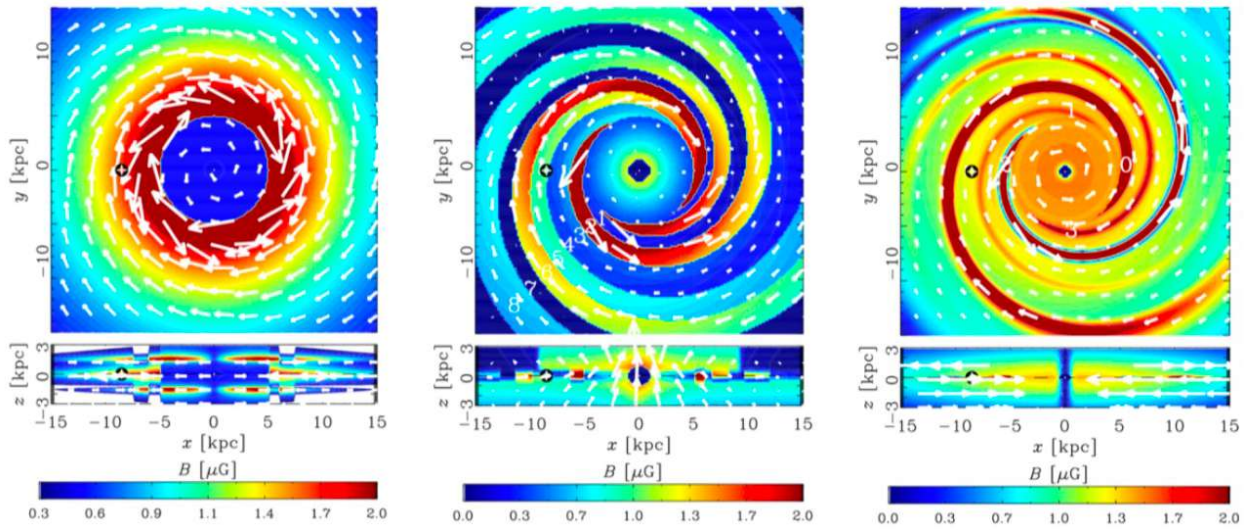

Figure 14: Graphical representation of three example models for the coherent magnetic field component in the Milky Way: on the *left* is from Sun et al. (2008); in the *middle* is from Jansson and Farrar (2012b); on the right is Jaffe et al. (2013). The colour represents the strength of the coherent magnetic component, the white arrows show its direction. The top panel of each shows a cut through the Galactic plane at $z = 0$ with the Sun position marked by the black plus, while the bottom panel of each shows a vertical cut intersecting the Sun and the GC (Boulanger et al., 2018).

Models using a thermal electron model combined with an assumed cosmic ray distribution find an approximate value for the average regular GMF strength as $\langle B_{regular} \rangle \approx 1 - 2\,\mu\text{G}$. Furthermore, the strength of the average random GMF in the solar neighbourhood is obtained as $\langle B_{random} \rangle \approx 3 - 5\,\mu\text{G}$. The best fit category of models in this case is found to be the axisymmetric spiral with a pitch angle of approximately 12° (Beck and Wielebinski, 2013).

2.4 Motivation

The previous sections place the Galactic pulsar population in the appropriate physical context and describe key measurable quantities used to obtain insights into the GMF. It is thus now timely to introduce three key questions at the core of the motivation of this master thesis. These questions are listed below, followed by a brief description of the outline of this work.

- **How is the Galactic Magnetic Field strength constrained by pulsar measurements?**
- **What kind of information about the structure of the Galactic Magnetic Field can be obtained from pulsar measurements?**
- **Are field reversals present in the Galactic disk according to observations of pulsar signals?**

At this point, the reader may ask for the relevance of these specific questions. Actually, the main answer is intimately related to the content of section 2.3.3. Addressing the three outlined questions is of major importance to model the GMF. As shown in section 2.3, the GMF is still a highly-debated and not well-understood topic. The importance of the magnetic field in the interstellar environment is emphasised by its strong contribution to the ISM energy density as shown in Fig. 15a. In fact, its almost equipartition with the cosmic rays' energy density contribution indicates a relation between the two. This connection is related to the property of cosmic rays being charged particles and thus being confined by the magnetic field in the Galaxy. A sketch showing the propagation of cosmic rays compared to neutral γ rays is shown in Fig. 15b.

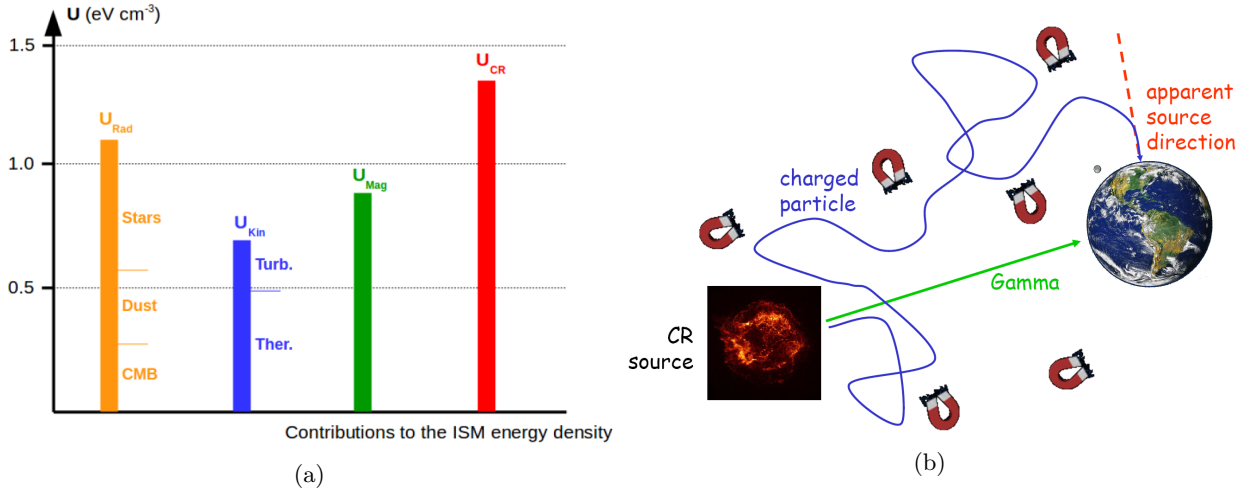

(a) (b)

Figure 15: (a) Comparison of the main contributions to the ISM energy density (De Becker, 2021a). (b) Propagation of cosmic rays (charged particles) in the ISM (Ribó, 2021).

The outline of this work commences with the introduction of important concepts, like the DM and RM, as well as the complex subject of the GMF and its study, in section 2. Following this theoretical section, the applied procedure to the used pulsar catalogue is introduced in section 3. This includes several filtering criteria, but also geometric consideration including notably the use of Galactic Dynamics criteria to define various Galactic regions within the Milky Way. Furthermore, different coordinate systems are exploited to obtain a beam-like division of these regions. Finally, this section introduces three different techniques to retrieve complementary information on the GMF. In the following section, section 4, these methods are applied to the different Galactic regions. The corresponding results are then presented in detail. These results are discussed

and placed in the appropriate physical context in section 5 . This discussion includes the comparison to other studies published in the framework of the indicated evolving scientific field. Section 6 formulates the main conclusions and summarises the key points of this work. Lastly, an indication of prospects is provided in section 7.

3 Procedure

This section outlines the methodology used in this thesis to provide insights on the Galactic Magnetic Field (GMF). First, techniques to exclude non-reliable values are introduced, followed by a subdivision of the Galaxy in multiple regions. Then, to make use of different sight lines, a binning procedure is presented. Finally, different methods for the examination of the GMF are established. It may be noted that the whole procedure is implemented in a fully-automatised python script. A review of the methodology is provided in Appendix A.

3.1 Filtering techniques

As explained in section 2.3.1, the use of pulsar RMs to constrain the GMF is especially appealing for sources lying within the Galactic disk. To study these objects, certain filtering methods must be implemented. Those methods are described and explained in the following. It may be noted that a major focus lies on the geometric aspects. Furthermore, the impossibility of seeing our own Galaxy face-on results in some assumptions being largely based on the observation of other galaxies. For a review of these observations, the interested reader may be referred to Beck and Wielebinski (2013).

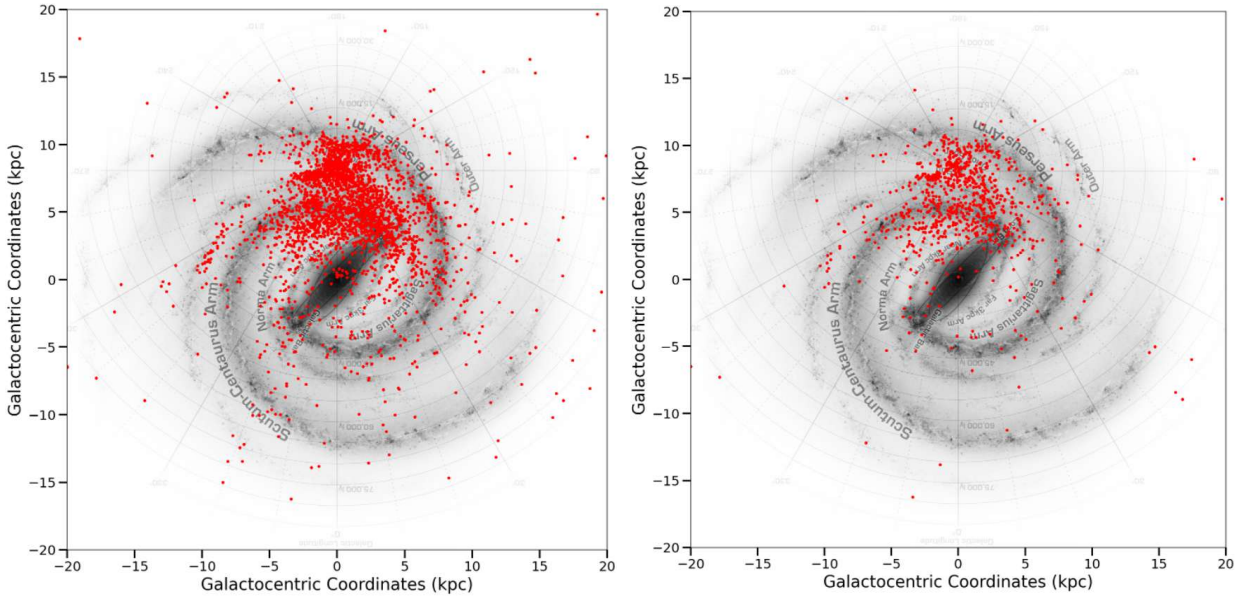

(a) Full catalogue

(b) Reduced catalogue

Figure 16: Representation of the reduction in the number of objects due to the applied filtering methods.

First, some more general filtering measures are applied to exclude non-reliable pulsar measurements. All sources with no given Galactocentric x-coordinate (XX) or y-coordinate (YY) are excluded. The same procedure is used for the distance, DM, RM, Right Ascension (RA), and Declination (DEC). In addition, values for the RM with large uncertainties are excluded. On the one hand, an uncertainty of more than $35\,\mathrm{radm}^{-2}$ as used in Han et al. (2018), and on the other hand a limit on the relative error of 50% are employed. This part of the procedure is applied in the same manner for every employed method and results in a reduction in the number of objects from 3282 (full catalogue) to 925. It may be noted that the major reduction results from the exclusion of sources without available measurements of the DM or RM, namely an

exclusion of 1962 sources. Fig. 16 a and b show the full and reduced catalogue respectively. Both figures and all following figures of similar type make use of a modified background image by **NASA/JPL-Caltech/R. Hurt (SSC/Caltech)** which may hereby be indicated for the entirety of this work.

3.2 Geometric division

Studying the Galactic pulsar population within physically relevant regions suggests the use of known Galactic components. The Milky Way is expected to consist of multiple different components of different stellar composition and origin. While certain features like the presence of the thick disk are still subject to debate (see e.g. Fuhrmann, 2011; Bovy et al., 2012), a basic structure is generally agreed upon as briefly introduced in the following, focusing on the regarded features in this work. For a more thorough review of the Milky Way's structure and its origin, the interested reader may be referred to the review by Helmi (2020).

Naturally, one may start with the component encompassing the Sun, namely the thin disk. It constitutes the most central part of the Galaxy with a radial extension of around 14 kpc (Robin et al., 2003). The ISM in this region resembles the young stellar disk population with a radial scale length of $h_R \approx 4500\,\mathrm{pc}$ and scale height of $h_z \approx 140\,\mathrm{pc}$ (Figueras Siñol, 2021).
The GC region is included in the bar/bulge region. Orientation as well as extension of these regions are not completely agreed upon. The presence of a bar however is common for spiral galaxies like the Milky Way as found by e.g., Eskridge et al. (2000) who found that only 27% of their sample of spiral galaxies do not show a bar in the near-infrared. In terms of size, the radius of the bar is assumed to lie within the order of 2 to 3 kpc. Due to its misalignment with the disk, one may assume the inner approximately 2 kpc to be affected by the bar. Furthermore, a scale height of the order of 300 pc is assumed (Rich, 2013).
Like the thin disk, the thick disk also shows a disk-like geometry with larger vertical extent than the former. Robin et al. (2003) estimate its radial scale length and scale height from the Besançon model of stellar population synthesis (originally described in Robin et al. 2003) as $h_R \approx 2500\,\mathrm{pc}$ and $h_z \approx 800\,\mathrm{pc}$ respectively. Finally, the Galactic halo is another major component of the Milky Way galaxy. It contains the most metal-poor and likely oldest stars in the Galaxy. For the sake of simplicity, it may be assumed to have a spherical shape. When studying its dynamics and more exact properties, one should however consider its varying shape with distance from the GC (Helmi, 2008). The interested reader is referred to Helmi (2008) for a general review on stellar halos with a focus on the Milky Way's. Sobey et al. (2019) determined the Galaxy halo magnetic field scale height as $h_z \approx 2\,\mathrm{kpc}$ in the first and second Galactic quadrant, i.e., for Galactic longitudes between $30° \leq l \leq 180°$, using pulsar measurements.

Following the outlined Galactic structure, one may divide the Milky Way in several regions for separate analysis using the techniques described in section 3.4. The regions are referred to by ascending integer numbers as well as by specific labels as described in the following and briefly summarised in Tab. 1.

The first region is roughly constrained by the thin disk Galactic component. Its vertical extension corresponds to the thin disk's assumed scale height of 140 pc, translating to $-140\,\mathrm{pc} \leq ZZ \leq 140\,\mathrm{pc}$. To exclude the central bar/bulge region, an inner boundary is set to 2 kpc in radius from the GC. Furthermore, an outer boundary is chosen as the radius of 14 kpc, corresponding to the edge of the disk. This region is straightforward named 'thin disk'.

As the second region, a larger vertical distance from the Milky Way's plane is chosen. It is expected to be dominated by the thick disk component. Thus, a vertical extension is chosen as $140\,\mathrm{pc} \leq ZZ \leq 800\,\mathrm{pc}$.

Starting at one scale height of the thin disk from the Galaxy's plane up to one scale height of the thick disk from the same plane. As for the first region, the central bar/bulge region is excluded from the analysis. This region is referred to as the 'thick upper disk'.

Region three corresponds to region two, mirrored at the Galaxy's plane. It is dubbed 'lower thick disk'.

Regions four and five consist of the thick and thin disk components above and below the Milky Way's plane, respectively. Thus, they encompass part of region one and region two, or three, respectively. In terms of vertical extension, this corresponds to $0 \leq ZZ \leq 800\,\mathrm{pc}$ and $-800\,\mathrm{pc} \leq ZZ \leq 0$. These regions are named 'upper disk' and 'lower disk' respectively.

Two regions dedicated to the halo magnetic field are dubbed region six and seven, or 'upper halo' and 'lower halo'. The former is located above the Galactic plane whereas the latter is below the plane. From prior pulsar observations, the extensions are chosen according to the derived halo magnetic field scale height. Thus, the occupied vertical ranges become $800\,\mathrm{pc} \leq ZZ \leq 2\,\mathrm{kpc}$ and $-2\,\mathrm{kpc} \leq ZZ \leq -800\,\mathrm{pc}$ respectively, with the assumed thick disk dominated area at the inner and the halo scale height at the outer boundary. As in the previous regions, the central region is excluded through the introduction of a spherical volume.

Finally, the last selected region, region eight, corresponds to the previously always excluded central bar/bulge region. Its radial extension is chosen to 2 kpc with a vertical extension of $-300\,\mathrm{pc} \leq ZZ \leq 300\,\mathrm{pc}$. Studying this region may give insight into the central Galactic region. The non-division into subregions results from the uncertainty and difficulty to constrain the structure in this region. To not omit part of the central bar/bulge region, an additional region is defined with the same radial extension as region eight, but an entirely spherical shape with radius $R = 2\,\mathrm{kpc}$. Due to its origin in the definition of region eight, it is dubbed region eight plus.

Number	Region	Radius	Height	Extra
1	Thin disk	$2\,\mathrm{kpc} < R \leq 14\,\mathrm{kpc}$	$-140\,\mathrm{pc} \leq ZZ \leq 140\,\mathrm{pc}$	Exclude bar/bulge
2	Thick upper disk	$2\,\mathrm{kpc} < R \leq 14\,\mathrm{kpc}$	$140\,\mathrm{pc} \leq ZZ \leq 800\,\mathrm{pc}$	Exclude bar/bulge
3	Thick lower disk	$2\,\mathrm{kpc} < R \leq 14\,\mathrm{kpc}$	$-800\,\mathrm{pc} \leq ZZ \leq -140\,\mathrm{pc}$	Exclude bar/bulge
4	Upper disk	$2\,\mathrm{kpc} < R \leq 14\,\mathrm{kpc}$	$0\,\mathrm{pc} \leq ZZ \leq 800\,\mathrm{pc}$	Exclude bar/bulge
5	Lower disk	$2\,\mathrm{kpc} < R \leq 14\,\mathrm{kpc}$	$-800\,\mathrm{pc} \leq ZZ \leq 0\,\mathrm{pc}$	Exclude bar/bulge
6	Upper halo	$2\,\mathrm{kpc} < R \leq 14\,\mathrm{kpc}$	$800\,\mathrm{pc} \leq ZZ \leq 2\,\mathrm{kpc}$	Exclude bar/bulge
7	Lower halo	$2\,\mathrm{kpc} < R \leq 14\,\mathrm{kpc}$	$-2\,\mathrm{kpc} \leq ZZ \leq -800\,\mathrm{pc}$	Exclude bar/bulge
8	Bar/Bulge	$0\,\mathrm{kpc} < R \leq 2\,\mathrm{kpc}$	$-300\,\mathrm{pc} \leq ZZ \leq 300\,\mathrm{pc}$	-
8+	Bar/Bulge extended	$0\,\mathrm{kpc} < R \leq 2\,\mathrm{kpc}$	$0\,\mathrm{kpc} < R < 2\,\mathrm{kpc}$	-

Table 1: Definition of used Galactic regions.

3.3 Binning

Using RMs to study the GMF allows to study the field component parallel to the line of sight. Thus, it is straightforward to employ a separation or division of the Milky Way into different sight lines. The ATNF catalogue provides the expected position of the different pulsars in terms of RA and DEC, in galactocentric coordinates (XX, YY, ZZ), as well as in Galactic coordinates (longitude, latitude). Galactic longitude and latitude can be seen in Fig. 17.

The latter coordinates are best suited for the purpose of defining different sight lines since they provide a solid-angle geometry for the different bins. This may be seen in Fig. 18a. It may also be noted that the geometric configuration results in pulsars with vastly different azimuthal position at large distance from the

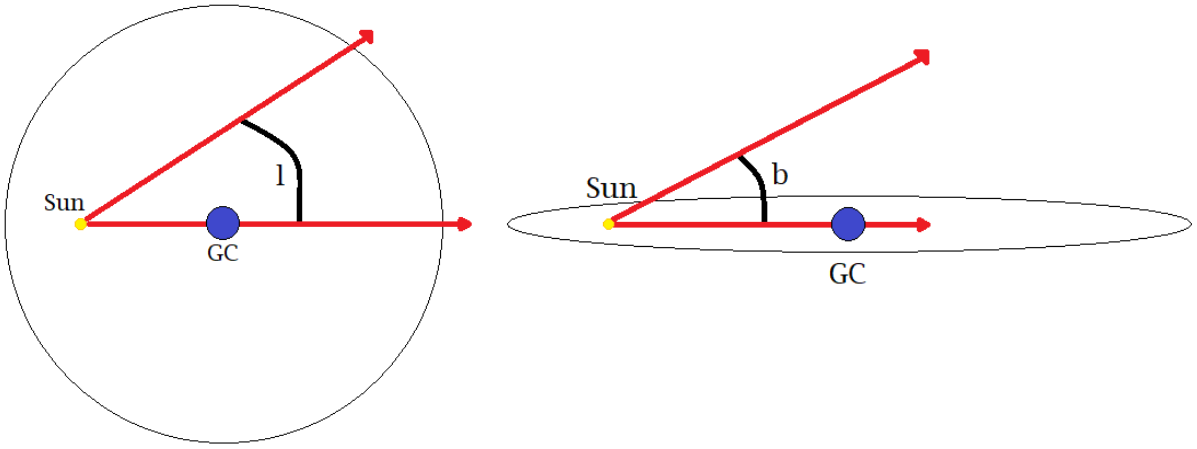

(a) (b)

Figure 17: Representation of Galactic longitude l (a) and Galactic latitude b (b).

Solar position to fall into the same longitudinal bin. Thus, the results from these sources must be treated carefully. Fig. 18a demonstrates the increase in area with distance for an exemplary bin in Galactic longitude and latitude. The increase of the area follows the relation $\left(\frac{r'}{r}\right)^2$ which leads to an exemplary increase of $\frac{A1}{A0} = 9$ for $r = 1\,\mathrm{kpc}$ and $r' = 3\,\mathrm{kpc}$. It may be noted that these radial distances still correspond to rather small distances from the solar position and severely more extreme cases are present for larger separations between r and r'. The limitation of the vertical extension proceeds through the Galactocentric z-coordinate (ZZ). Due to the limit in z-coordinate, the transverse distance in the longitudinal direction is of higher importance concerning the possible separation between two pulsars within the same bin. This transverse separation is plotted over the distance from the solar position in Fig. 18b and may be taken as a length scale over which the averaging takes place. Especially for the thin disk region, the limit in vertical extension results in the same vertical range for larger distances. Thus, the sight line architecture does not correspond to the geometry shown in Fig. 18a anymore for larger distances since the latitudinal extension decreases with distance.

The reasons for the z-limit are listed in the following. Sight lines at larger Galactic latitude are effectively suppressed with increasing distance. Due to the possible large vertical separation of the sources at these coordinate ranges, the questionable validity of them being in the studied region, e.g., the thin disk, as well as showing a large vertical separation from the sources at the region's central z-value, gives reason to exclude them from the analysis already at this early stage. The difference in the number of pulsars due to the filtering methods can be seen in Fig. 16 a and b where each red point represents one pulsar. Only the pulsars with information on their position are included. The first figure includes 3282 sources whereas the second one only includes 925. It may be noted that the largest reduction results from the exclusion of sources without available DMs and/or RMs.

After proceeding with the geometrical limitations, a binning is applied to the processed catalogue using a longitudinal extension of the individual bins of 1°. As a result, the Milky Way is binned into 360 regions. When utilising the measurements corresponding to a single pulsar only (see Method a, section 3.4.1), the whole path from the observer to the source effectively influences the measured DM and RM. Accounting for

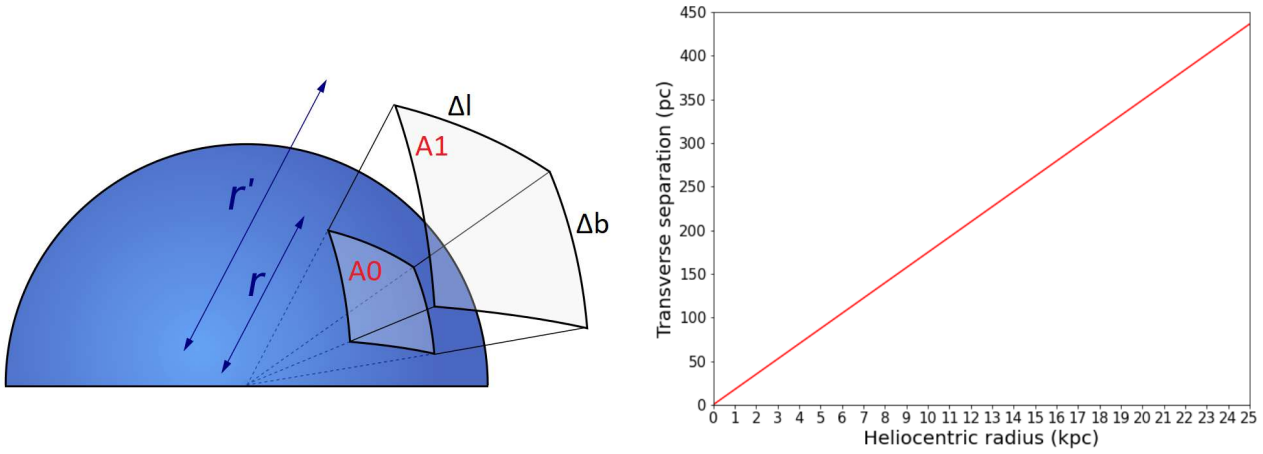

(a) (b)

Figure 18: (a) Rectangular solid angle geometry for the case of two areas (A0 & A1) at different radius with Galactic longitudinal and latitudinal bin extension as Δl and Δb respectively. (b) Maximum transverse separation within one bin of $\Delta l = 1^\circ$ versus distance from the observer, in this case the solar position.

this, only pulsars located on the nearer side of the Galaxy with respect to the Sun are included in the analysis. In other words, pulsars in the central bar/bulge region and behind it, as seen from the Solar position, are ignored. This procedure effectively introduces a longitudinal limit in shape of the full exclusion of the affected longitudinal range starting from the spherical Bar/Bulge region as shown in Fig. 19.
For methods that do not make use of the full path to the source (Methods b and c, section 3.4.2 and 3.4.3), no such measures are required. In these cases, the regions in front and behind the central bar/bulge region are separated and analysed independently as visualised in Fig. 19.

To enable the analysis with distance from the observer, a sorting algorithm is introduced and employed on the different bins. For Method c, the different bins are then divided into different ranges in distance to probe the magnetic field in a more local context.

3.4 Magnetic field estimation

In the following description, the means and concepts to estimate the GMF make strong use of the principles and equations outlined in section 2.3.2.

3.4.1 Single pulsar measurement (Method a)

The magnetic field may be determined by several diverse ways, using varying scales. The most straightforward way uses single pulsar measurements. It allows to determine the line of sight magnetic field averaged over the whole distance between the observer, in this case the Earth, and the pulsar. DM and RM enable this estimation through Eq. 24. It may be recalled that positive values of the determined quantity correspond to an average magnetic field along the line of sight directed towards the observer, whereas negative values correspond to the opposite case. This method does not require a binning of the Galaxy and allows for the highest number of eligible sources.
The results may be presented in diverse ways where the Solar position at the origin of the measurements should always be emphasised. For illustrative purposes, each pulsar measurement can be depicted by a dot

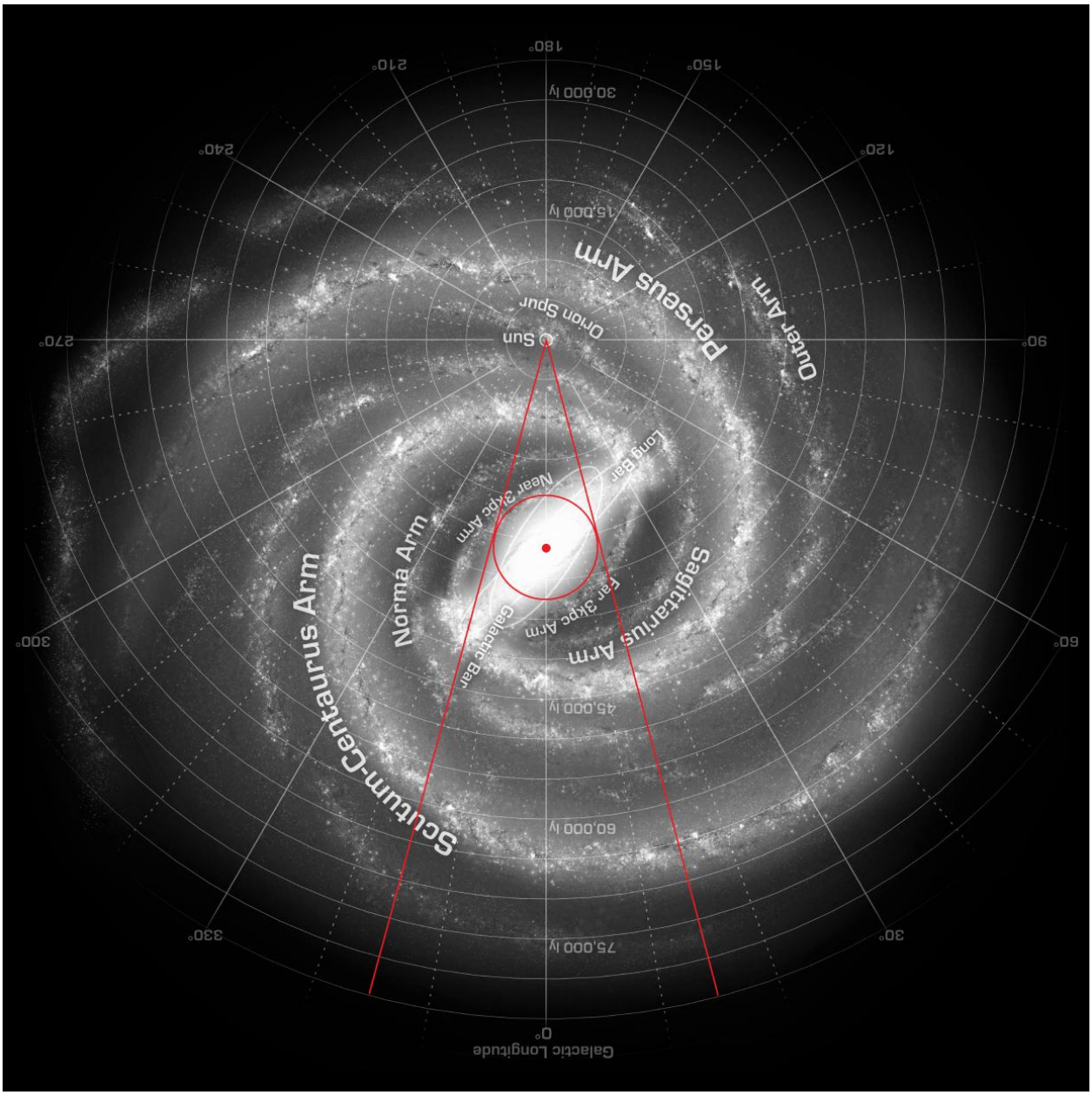

Figure 19: Excluded regions in longitude for the different methods.

in Galactocentric coordinates with an added colour scale indicating the calculated average magnetic field strength parallel to the line of sight. In the case of the thin disk component (Region 1) the result of utilising this technique is shown in Fig. 20. It may be noted that the commonly used background image positions the Sun at a Galactocentric radius of 8 kpc whereas this work, and the ATNF pulsar catalogue, uses a radial position of 8.5 kpc.

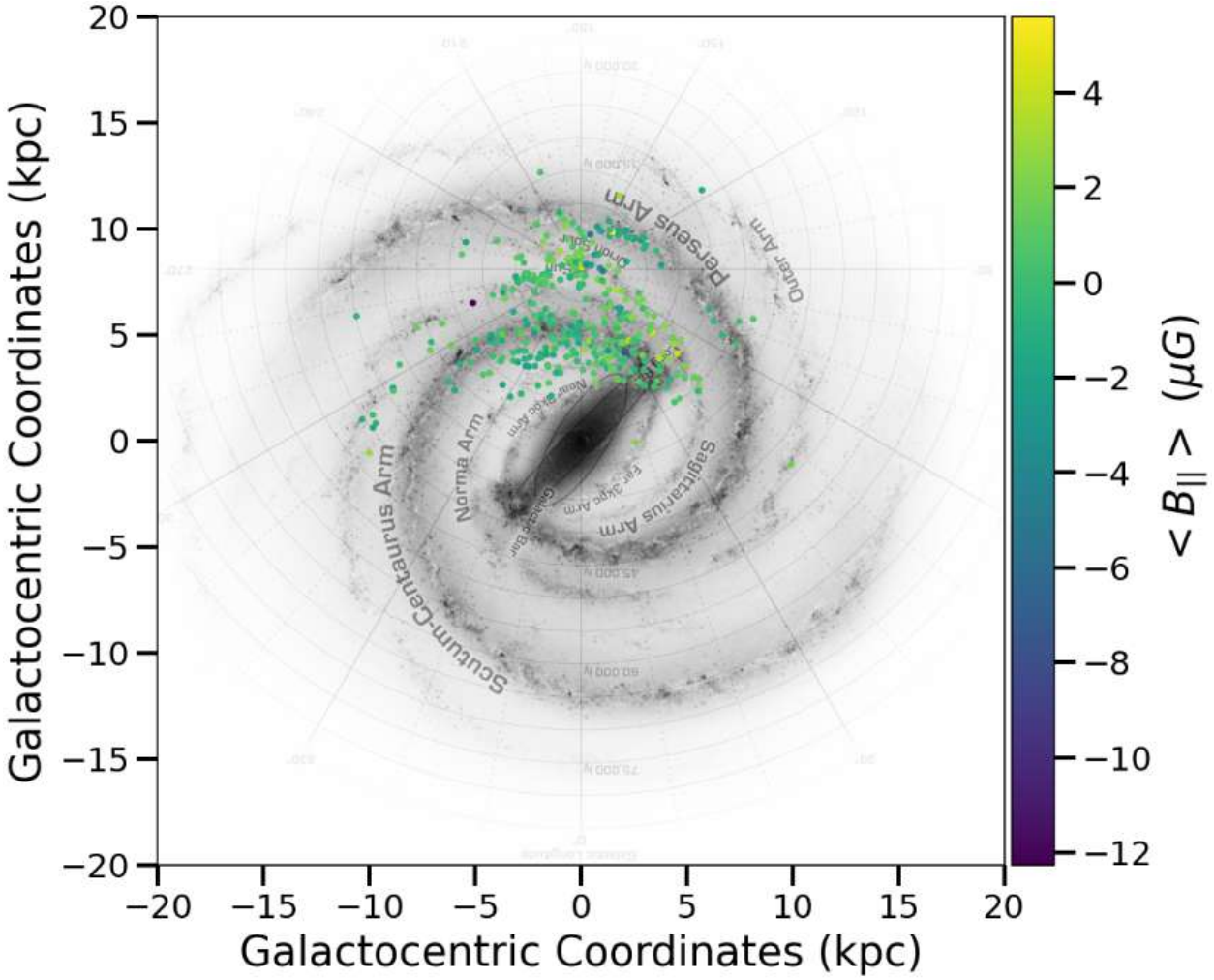

Figure 20: Representation of retrieved results with dots for Region 1 using Method a. The colour-coding indicates the averaged line of sight (with respect to the observer) magnetic field strength.

Instead of representing individual sources with dots, one may introduce vectors pointing in the direction of the magnetic field. Geometrically it is immediately clear that their direction must coincide with the line of sight path between the pulsar and the observer. In combination with the orientation of the pulsars according to the orientation of the average magnetic field, this results in an arrangement of vectors pointing to or away from the Solar position.

A representation of the results of this method for the thin disk component (Region 1) can be seen in Fig. 23b. In this representation, sight lines with estimated magnetic field strengths of more than 10 µG are excluded for illustrative purposes. All vectors start or end at the Solar position marked by the red dot. Fig. 21 uses the same results but, for the sake of illustration, only the closest source for each bins is drawn. It may be

however noted that this requires the application of a binning in Galactic longitude. The GC is located at (0,0) in both figures.

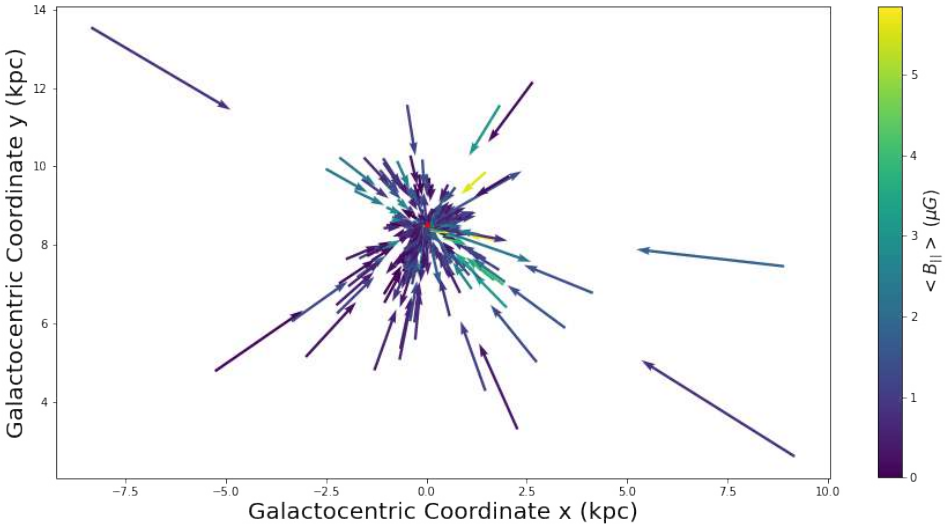

Figure 21: Representation of retrieved results with vectors for Region 1 using Method a. The vectors show the direction of the averaged line of sight magnetic field with respect to the observer. The colour-coding shows the corresponding strength. Here, only the closest pulsar for each bin is selected.

3.4.2 Two-pulsar measurement (Method b)

In addition to only utilising the information of one pulsar measurement, one may also study the magnetic field on a smaller scale by using subsequent pulsar in distance. The method employs the estimation of the average line of sight magnetic field between the two selected pulsars according to Eq. 25. Subsequent sources are chosen from the previously described binning of the Galaxy including the sorting algorithm in each bin by distance. It may be noted that only bins with at least two objects can be utilised for the method.

3.4.3 Multiple pulsar measurement (Method c)

To compensate for small-scale fluctuations, a linear-trend fitting is applied to the observed RMs with respect to their distance within individual bins. This method has the negative side-effect of averaging over large scales in distance and thus essentially losing information. Especially for sources at large distance it must therefore be applied with care and the separation of the individual pulsars must be taken into account. Since the main goal of this method is the search for monotonous trends in the magnetic field structure, a comparably homogeneous region with respect to this structure must be selected. Thus, Method c is only applied to the thin disk region (Region 1). Concerning the mentioned criterion and resulting region limitation, notably the alignment requirement of at least three sources along the same sight line and within the same distance range plays a key role.

4 Results

This section describes and illustrates the obtained results of applying the in section 3 defined methodology to the Milky Way galaxy.

Applying the boundaries of the in section 3.2 described regions as well as the binning as described in section 3.3 results in a further reduction of the sources within the different regions. The corresponding numbers are summarised in Tab. 2 starting with the vertical z-coordinate limit, followed by the radial limits, the possible exclusion of the bar/bulge region, the number of obtained sight lines, and finally the number of additional sight lines with magnetic field strength estimates above 20 µG. In case a measure is not applied or no sources are present, for the 'ultra-high' category, a '-' is inserted in the corresponding cell. In the following subsections, the results for each defined region and method are described and illustrated. It may be noted that notably the utilised definition of Region 4 and 5 results in sources belonging to the Galactic plane being present in both regions. Thus the total number of sources does not add up. This circumstance is however purposely chosen to avoid a possible artificially created asymmetry purely resulting from the geometric division into the different regions.

Number	Region	Method	#Objects				
			z	R	bar/bulge	#sight lines	ultra-high
1	Thin disk	a	412	410	410	410	-
		b			-	186	22
		c			-	28	-
2	Thick upper disk	b	182	181	-	54	3
3	Thick lower disk	b	184	182	-	53	-
4	Upper disk	a	392	391	384	384	-
		b			-	179	15
5	Lower disk	a	404	400	394	394	-
		b			-	188	8
6	Upper halo	b	53	53	-	7	1
7	Lower halo	b	63	60	-	6	-
8	Bar/Bulge	a	597	2	-	1	1
		b			-	0	-
8+	Bar/Bulge extended	a	-	5	-	4	1
		b			-	0	-

Table 2: Reduction in number of sources per region.

4.1 Thin disk

The defined thin disk region is one of only three sectors where the single pulsar measurement technique (Method a) can be applied. This is due to the Sun being located in the thin disk and thus the full line of sight path lies within the volume occupied by the thin disk region. Fig. 22a and Fig. 22b depict the reduction in the number of sources due to the definition of the region's vertical and radial boundaries respectively as included in Tab. 2 compared to the reduced catalogue as shown earlier, in Fig. 16b.

Geometrically, this region represents the Galactic thin disk. Its definition in terms of vertical and radial extension results in a reduction of the number of sources to 412 or rather 410. Thereby only the sources inner to the defined Galactic edge are included. Furthermore, the potentially complex and chaotic central Galactic region is avoided. The latter measure does however only constitute a minor decrease in the number of sources.

Fig. 22b depicts the Galactic distribution of pulsars within the region. The included sources are mainly located in the 'solar' half of the disk when dividing the Galaxy along the Galactocentric x-coordinate axis at the Galactocentric y-coordinate equal to 0. In this system, the Sun is located at position $(0, 8.5\,\mathrm{kpc})$. Regions corresponding to the Galactic arms show higher concentrations in terms of sources which may be attributed to the expected birth of stars, as neutron star predecessors, in the arm regions. Finally, the density of sources decreases with distance from the Solar position.

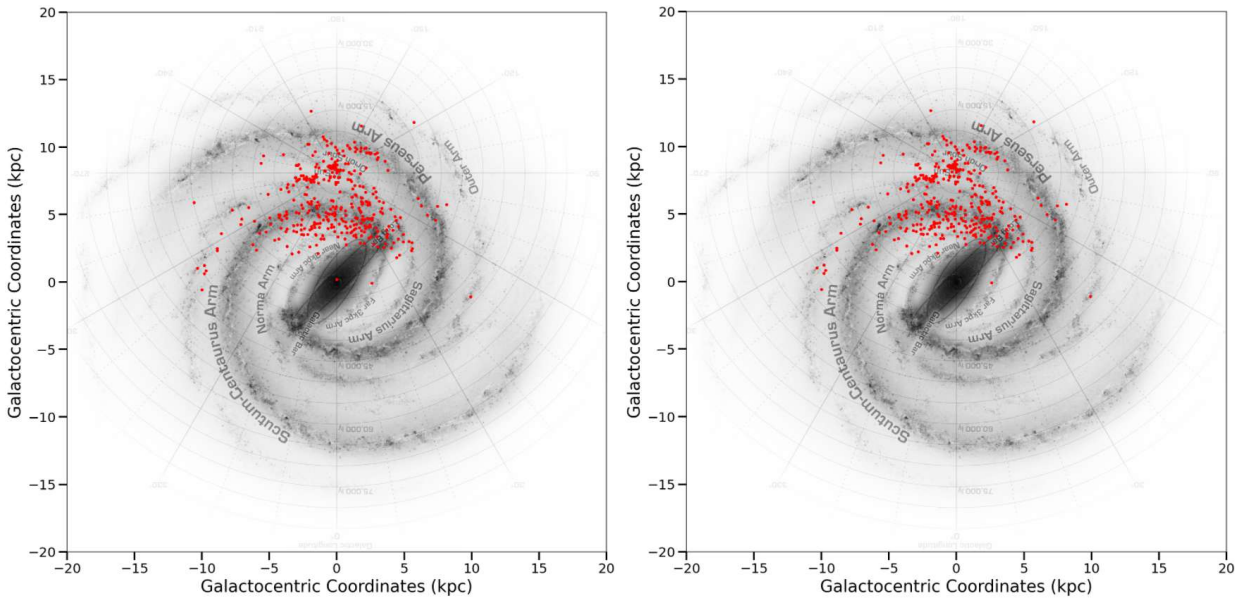

(a) (b)

Figure 22: Distribution of sources in the thin disk region after applying the vertical (a) and radial limits (b).

4.1.1 Single pulsar measurement

For the application of Method a, all sight lines/sources that constitute the output of the geometric and general filtering treatment are included. Thus, the used number of sight lines corresponds to 410. In Fig. 23a, the distribution of obtained absolute values of the average line of sight magnetic field is shown. It may be noted that a limit for the maximum value of $|\langle B_{\parallel}\rangle|$ is set to $20\,\mu\mathrm{G}$. The reasoning for this chosen value is of illustrative nature as well as to separate 'special' cases from the average distribution of magnetic field strength estimates. In the regarded case of Region 1 and Method a, no sight lines with values larger than $20\,\mu\mathrm{G}$ are obtained. The distribution in Fig. 23a shows a peak in the number of sight lines near $|\langle B_{\parallel}\rangle|$ equal to zero. Followed by a strong decrease for $|\langle B_{\parallel}\rangle|$ larger than $3\,\mu\mathrm{G}$.

The subsequent subfigure (Fig. 23b) depicts the orientation of the average line of sight magnetic field through vectors either towards the solar direction starting from the pulsar's location or vice versa. Corresponding values of $|\langle B_{\parallel}\rangle|$ are illustrated by a colour-coding with the colourbar shown at the right of the Galactocentric plot. Here, the larger number of sources towards smaller Galactocentric radii catches the eye. Furthermore, the mixture of orientations and magnetic field strength values is mostly heterogeneous and anisotropic.

Fig. 23c shows sight lines already included in Fig. 23b with the additional lower limit of $3\,\mu\mathrm{G}$. Thus, the relatively higher magnetic field strength values are included. Most pulsar locations are concentrated along two to three longitudinal ranges. Moreover, values for $|\langle B_{\parallel}\rangle|$ present a preference towards the lower boundary

of 3 µG. It may be noted that only one sight line provides a $|\langle B_{\parallel}\rangle|$ estimate of more than 10 µG.
In Fig. 23d almost all sources already present in Fig. 23b are shown again. Thus, most sight lines probed using Method a provide relatively low $|\langle B_{\parallel}\rangle|$ results, namely between 0 and 3 µG in terms of absolute values. The limiting value of 3 µG is notably also used by Noutsos et al. (2008). In addition, it should be noted that the arrangement of orientations and estimates presents a very mixed, anisotropic structure.

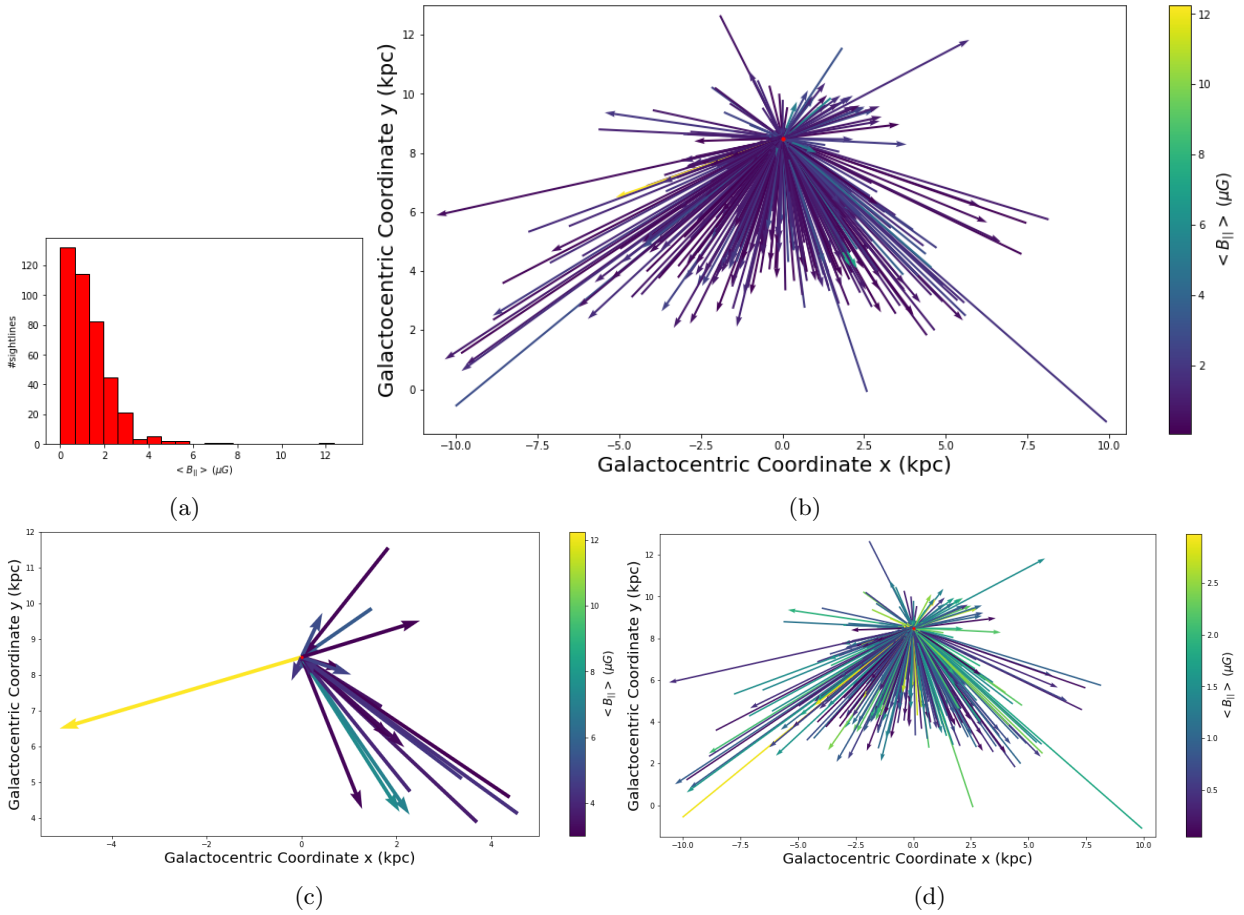

Figure 23: Determined values for the line of sight average magnetic field strength for Region 1, Method a (a) and geometric configuration (b) with separated higher ($\langle B_{\parallel}\rangle \geq 3$ µG)(c) and lower ($\langle B_{\parallel}\rangle < 3$ µG)(d) values.

4.1.2 Two-pulsar measurement

To make use of Method b, one must select sight lines including the longitudinal alignment of a minimum of two sources with respect to the Solar position. Applying this extended binning procedure results in 186 valid sight lines. It may be noted that this number is less than half the number of sight lines available for Method a when studying the same defined region.
As for Method a, Fig. 24a depicts the distribution of sight lines against their respective average line of sight magnetic field strength value. The number of sight lines decreases in this case less quickly with $|\langle B_{\parallel}\rangle|$ than for Method a. Compared to Method a, higher magnetic field strength estimates are obtained with this smaller scale approach.
The used 'differential' sight lines are shown in Fig. 24b. Here the upper limit of $|\langle B_{\parallel}\rangle| < 20$ µG is introduced again. Overall, the arrangement of vectors presents dispersed/chaotic orientations towards the inner Galaxy.

Besides, the longer differential sight lines approximately aligned with the Galactocentric x-axis, corresponding to longer distances between subsequent pulsars within a bin, are roughly aligned to the azimuthal direction with respect to the Galaxy.

In Fig. 24c, only the higher values of the magnetic field, above 3 µG, are shown. High values towards the inner Galaxy are observed for relatively small distance between the respective pulsars. Moreover, a preference for the number of differential sight lines towards decreasing Galactocentric y-coordinate in combination with increasing Galactocentric x-coordinate is observed.

Like for Method a, most sight lines obtained using Method b provide $|\langle B_\parallel \rangle|$ estimates within the range of absolute values between 0 and 3 µG as shown in Fig. 24d. Also, most sight lines are located towards the inner Galaxy as well as showing an anisotropic overall structure. Only a few sight lines lie in the longitudinal range that constitutes the half of Galactocentric y-coordinate values larger than 8.5 kpc. It may be reminded that the Solar position is illustrated by a red dot at $(0, 8.5\,\mathrm{kpc})$ in Galactocentric coordinates.

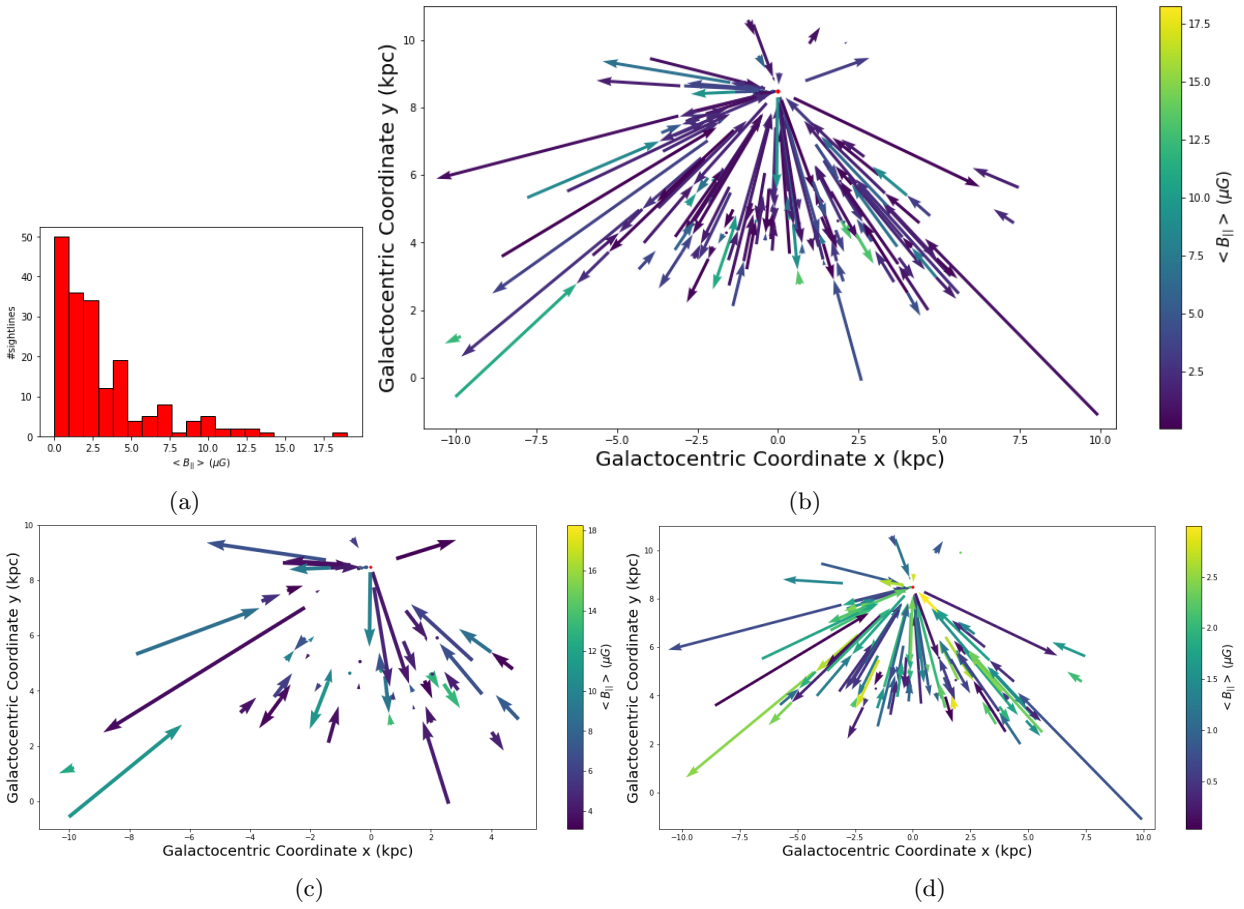

Figure 24: Determined values for the line of sight average magnetic field strength for Region 1, Method b (a) and geometric configuration (b) with separated higher ($\langle B_\parallel \rangle \geq 3\,\mu\mathrm{G}$)(c) and lower ($\langle B_\parallel \rangle < 3\,\mu\mathrm{G}$)(d) values.

The previously excluded twenty-two sight lines with magnetic field strength values above 20 µG are depicted in Fig. 25. Many of these sight lines are concentrated towards decreasing Galactocentric y-coordinate and increasing Galactocentric x-coordinate with respect to the Solar position, marked by a red dot. It may also be noted that none of them lies within radial proximity of around 1 kpc of the Sun. Finally, the highest $|\langle B_\parallel \rangle|$ estimates occupy relatively small regions, i.e., are found for subsequent pulsars of relatively small separation

within the respective bins. The discussion of these likely 'non-physical' values of the average line of sight magnetic field is postponed to section 5. One sight line gives an exceptionally high estimate of around 382 µG.

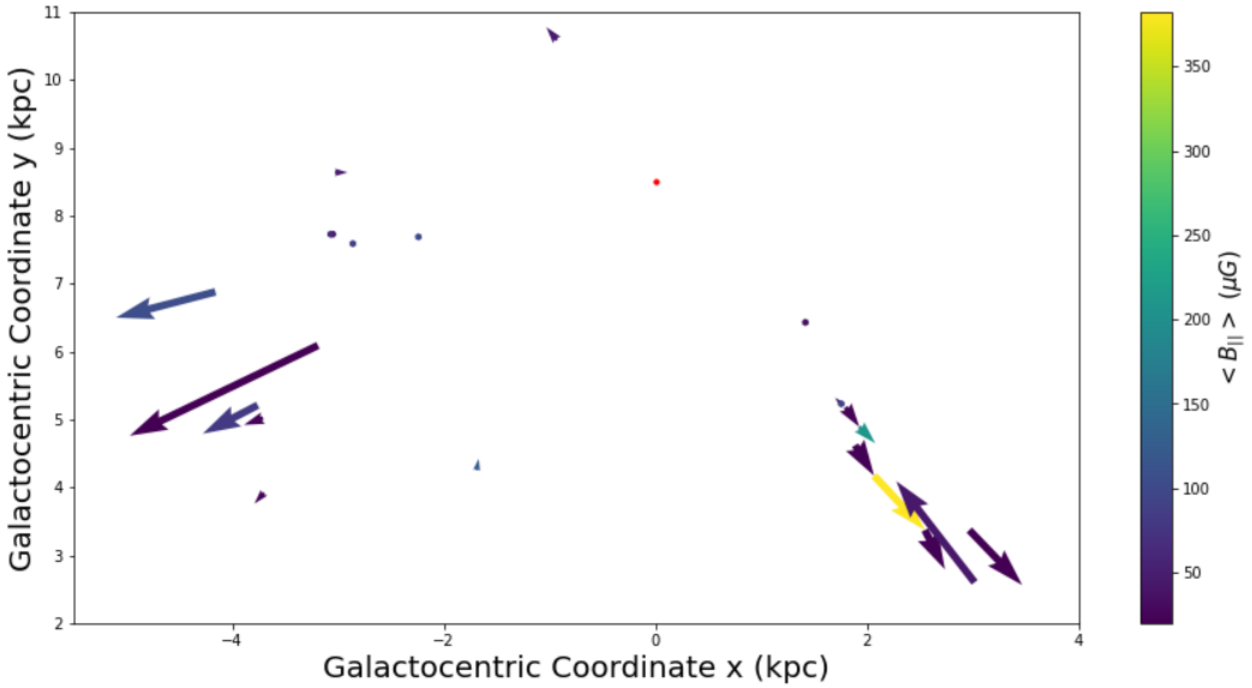

Figure 25: Determined values for the line of sight average magnetic field strength $> 20\,\mu G$ for Region 1, Method b.

4.1.3 Multiple pulsar measurement

When applying Method c, one may define certain distance intervals to make a sampling of a smaller region possible and avoid an averaging over regions as large as the Galaxy itself. Therefore, four distance ranges with respect to the Solar position are used for the thin disk region. These are listed in Tab. 3 with the total number of obtained sight lines. 15 of the 28 sight lines are disregarded in the presentation of results. Their discussion is postponed to section 5. The most representative ones are then shown in Fig. 26 to 29 with corresponding linear trends of the RM over distance. The latter ones can be attributed to the respective sight line through the introduced colour-coding. Moreover, estimated average magnetic field strengths parallel to the corresponding sight line resulting from the introduced linear trend are given above the respective linear trend figure. It may however be noted that the use of this method concentrates on the orientation of the magnetic field rather than its strength. Moreover, reminding section 3.4.3, Method c is only applied to Region 1, the thin disk region.

The sight lines in Fig. 26 coincide with the expected position of the Scutum-Centaurus arm and/or the Sagittarius arm. Most sight lines resemble the spiral structure of the Milky Way. Results concerning the orientation of the magnetic field, with + representing the direction towards the observer and − the opposite, are listed in Tab. 4 and 5 for the sight lines in Fig. 26a and 28a respectively. Moreover, an indication of the implication on the large-scale magnetic field's direction is given by CW and CCW corresponding to a clockwise and counterclockwise orientation respectively. The special case of sight line 5 in Tab. 4 is further discussed in section 5.

Distance intervals	#sight lines
[0,2,5,9,15]	28

Table 3: Used distance intervals and obtained number of sight lines for Region 1 with Method c.

Number	Colour	$\lvert \langle B_{\parallel} \rangle \rvert$	sign	field configuration
1	purple	2 µG	+	CCW
2	yellow	15 µG	-	CW
3	dark purple	3 µG	+	CCW
4	light green	2 µG	+	CCW
5	blue	2 µG	(-)	(CW)
6	green-blue	2 µG	+	CCW
7	turquoise	5 µG	-	CW

Table 4: Determined $\lvert \langle B_{\parallel} \rangle \rvert$, including its indicated direction, and the corresponding orientation of the large-scale magnetic field for Region 1 with Method c, 1/2.

Number	Colour	$\langle B_{\parallel} \rangle$	sign	field configuration
1	-	6 µG	-	CCW
2	-	1 µG	-	CCW
3	-	5 µG	+	CW
4	green	8 µG	-	CCW
5	turquoise	1 µG	-	CCW
6	green-blue	1 µG	+	CW

Table 5: Determined $\langle B_{\parallel} \rangle$, including its indicated direction, and the corresponding orientation of the large-scale magnetic field for Region 1 with Method c, 2/2.

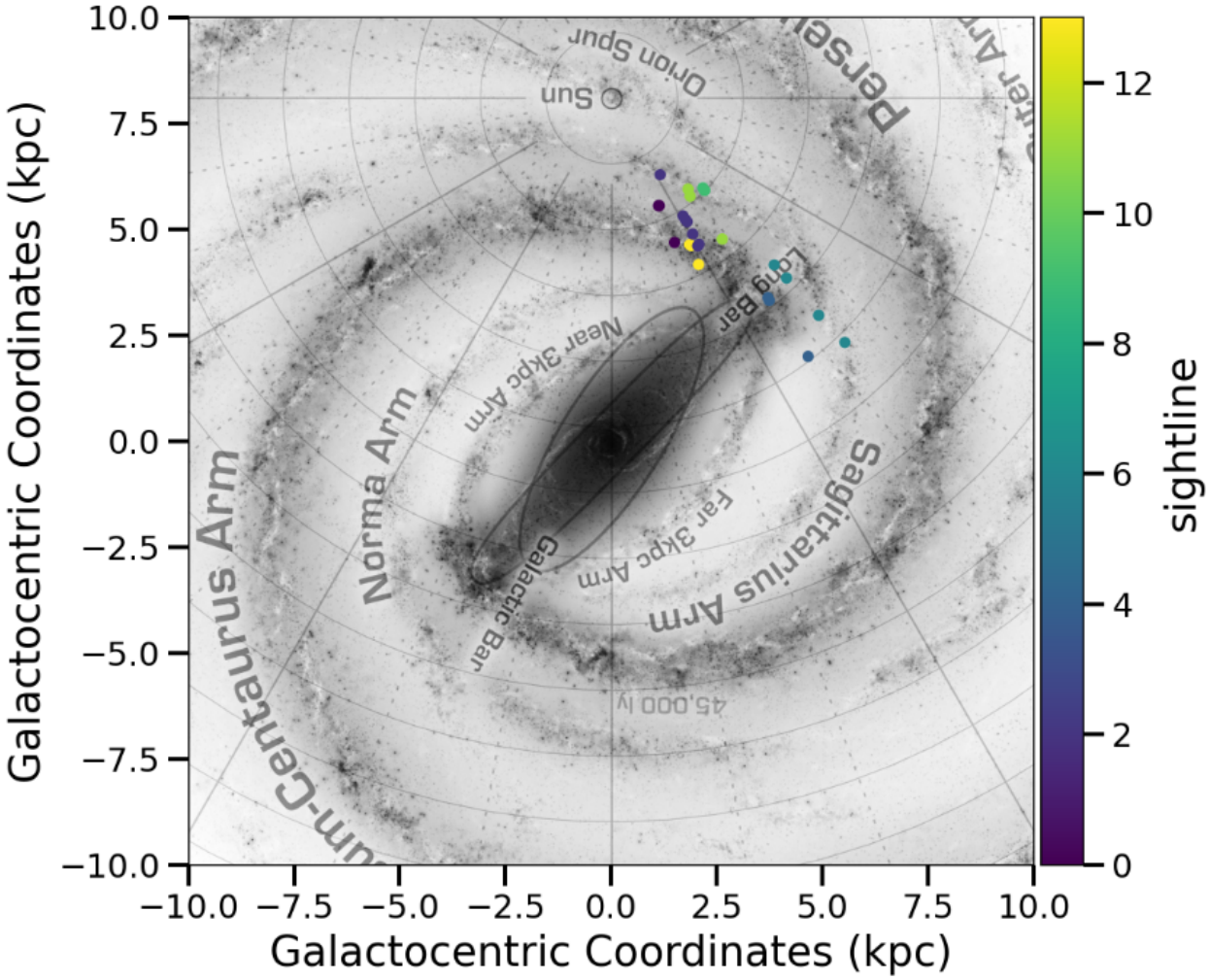

(a)

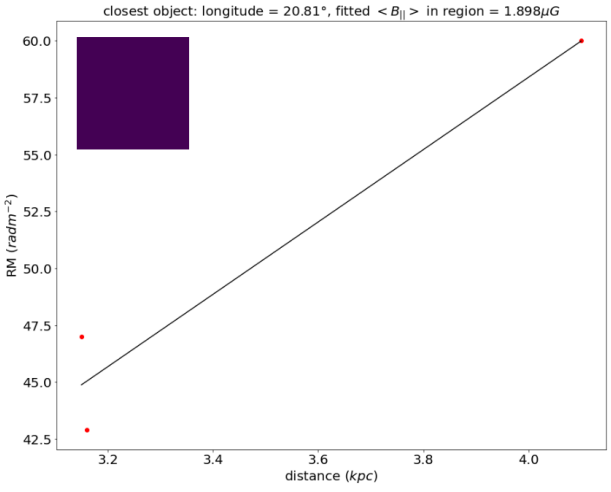

(b)

Figure 26: Linear trends in the RM for Region 1, Method c, 1/2.

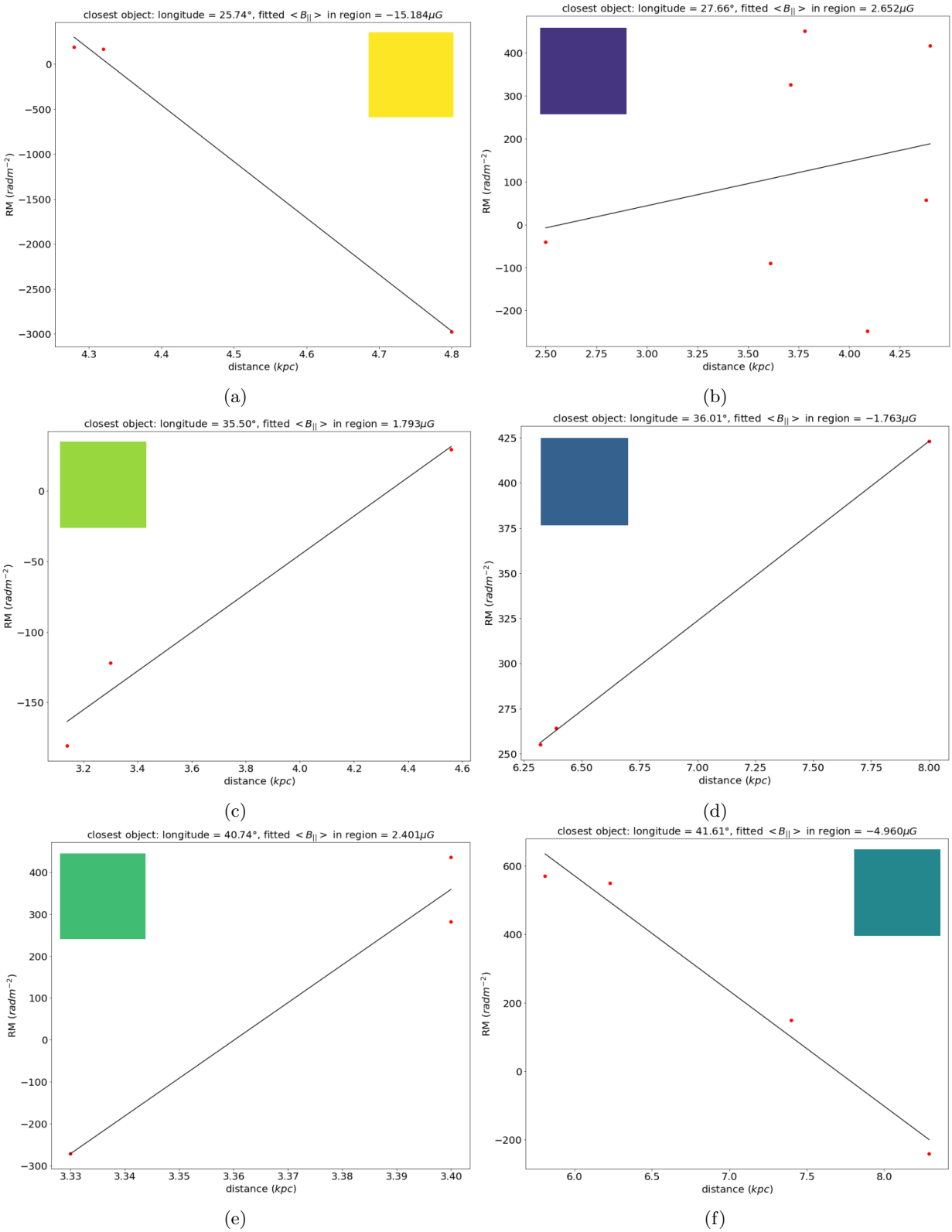

Figure 27: Continuation of: Linear trends in the RM for Region 1, Method c, 1/2.

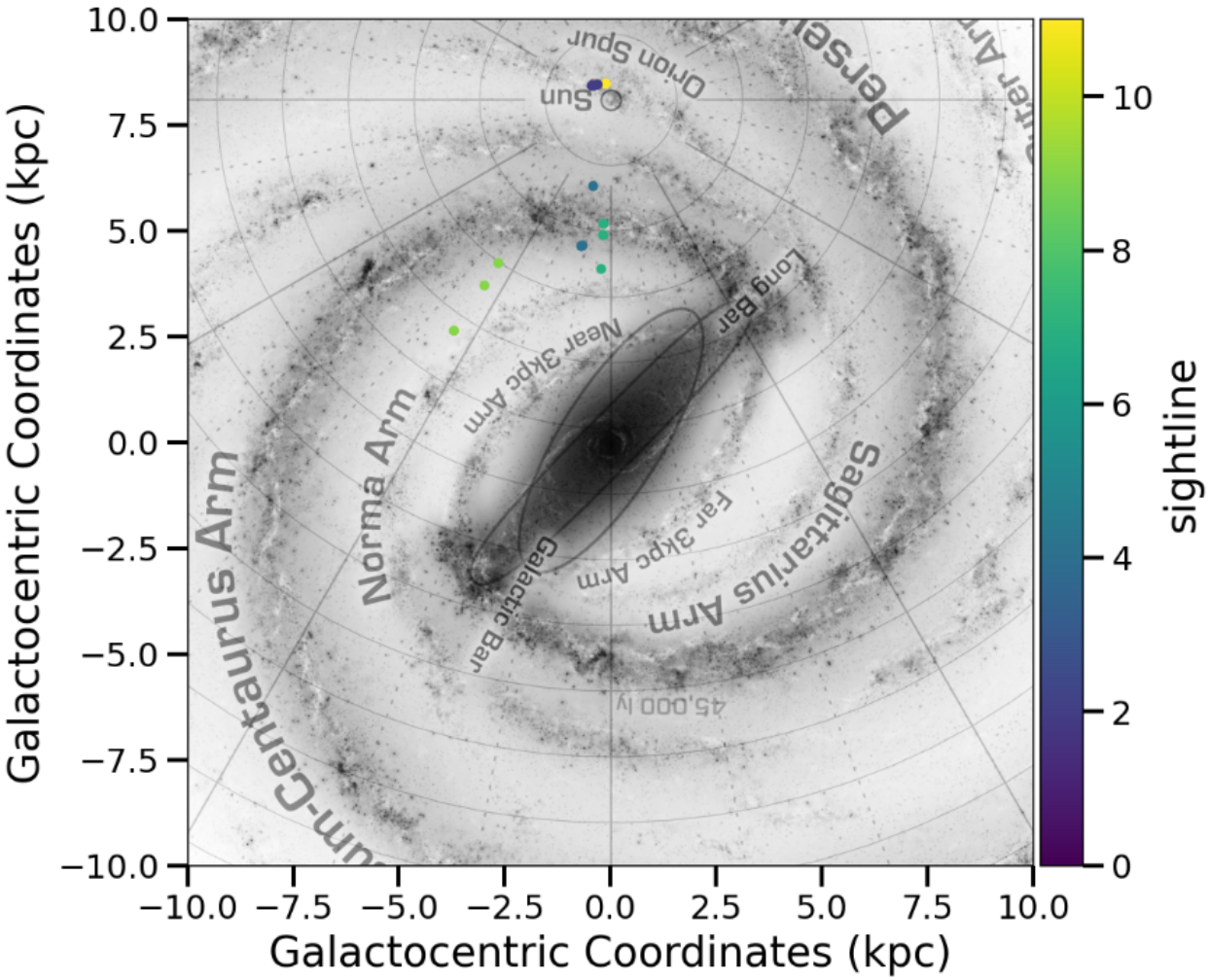

(a)

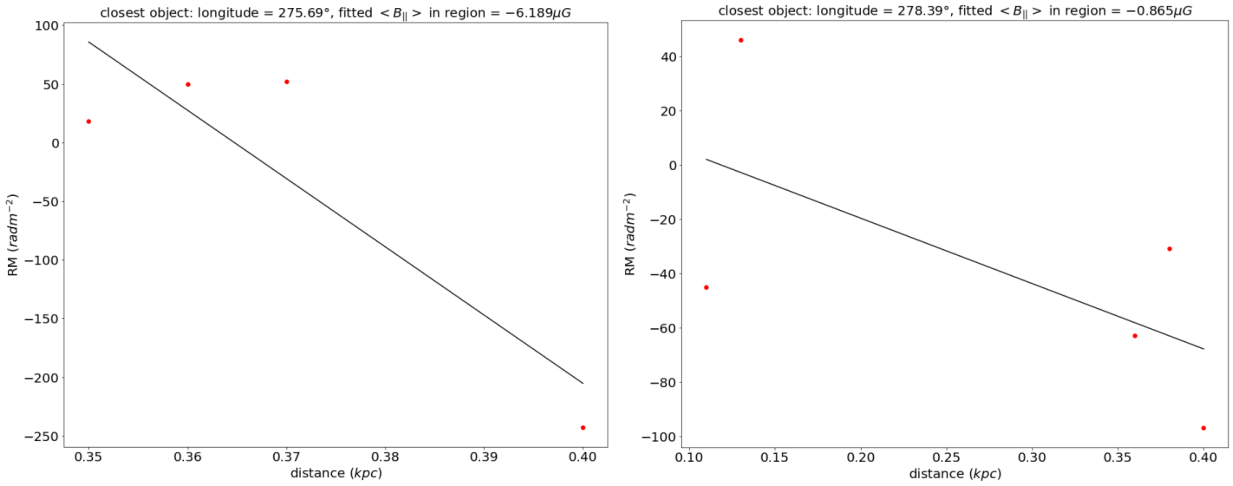

(b) (c)

Figure 28: Linear trends in the RM for Region 1, Method c, 2/2.

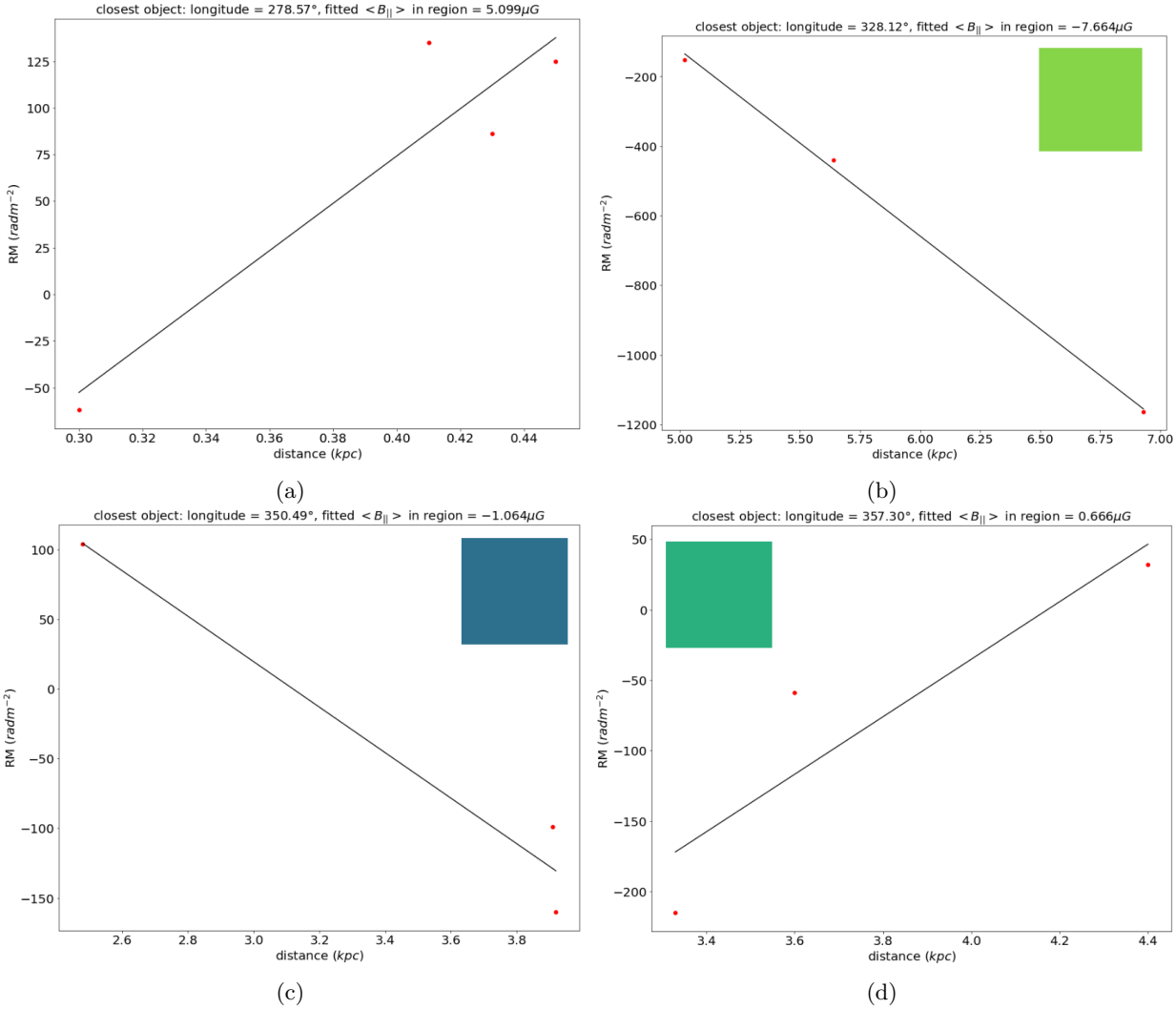

Figure 29: Continuation of: Linear trends in the RM for Region 1, Method c, 2/2.

4.2 Thick upper disk

The second region corresponds to the Galactic thick upper disk. In total, 181 valid sources are located within this region. Their distribution projected on the Galactic plane is shown in Fig. 30b. The 'non-solar' half of the Galaxy in terms of Galactocentric y-coordinate is only occupied by a small number of sources. Overall, a concentration of pulsars around the Solar position, which is shown by a red dot, may be observed. Moreover, most sources lie within a longitudinal cone-like area as seen from the Sun towards the inner Galaxy. Since the Solar position is estimated to be outside of the studied region, it is not possible to apply Method a.

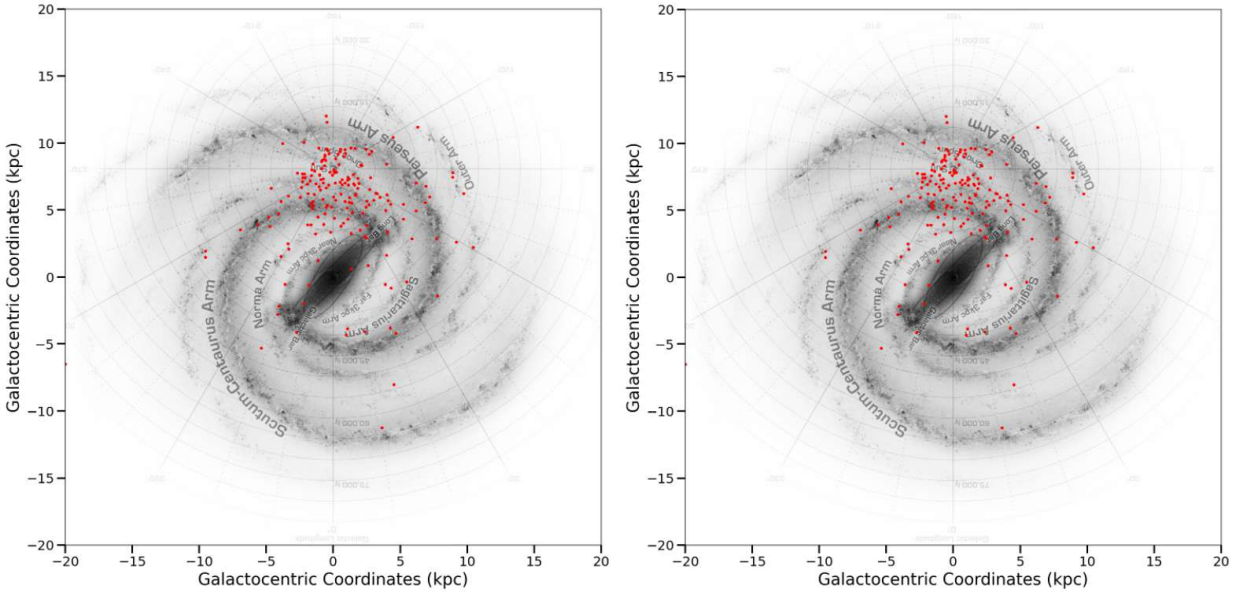

(a) (b)

Figure 30: Distribution of sources in the thick upper disk region after applying the vertical (a) and radial limits (b).

4.2.1 Two-pulsar measurement

The alignment requirement for Method b results in a reduction of the number of sources in this region to 54 sight lines.

As for the other methods and regions, Fig. 31a shows the distribution of $|\langle B_{\parallel} \rangle|$ estimates with respect to the number of sight lines. In this case, it may be noted that this distribution does not peak at the lowest $|\langle B_{\parallel} \rangle|$ value. The 'peak' is followed by a slow and non-steady decrease in the number of sight lines with increasing magnetic field strength values.

The geometrical arrangement of sight lines is depicted by Fig. 31b. Most sight lines are located towards the inner Galaxy. A slight preference towards increasing Galactocentric x-coordinates can be seen. Regarding 'differential' $|\langle B_{\parallel} \rangle|$ estimates, most sight lines are concentrated in rather narrow longitudinal ranges.

Within the higher range of $|\langle B_{\parallel} \rangle|$ estimates in Fig. 31c, the general geometry is less anisotropic with some preferential orientation for similar longitudinal sight lines.

Lastly, the lower range of magnetic field strength estimates in Fig. 31d encompasses notably an exceptionally long sight line towards decreasing Galactocentric x- and y-coordinates. Furthermore, several concentrations of anisotropic orientations and varying $|\langle B_{\parallel} \rangle|$ estimates along certain sight lines can be seen.

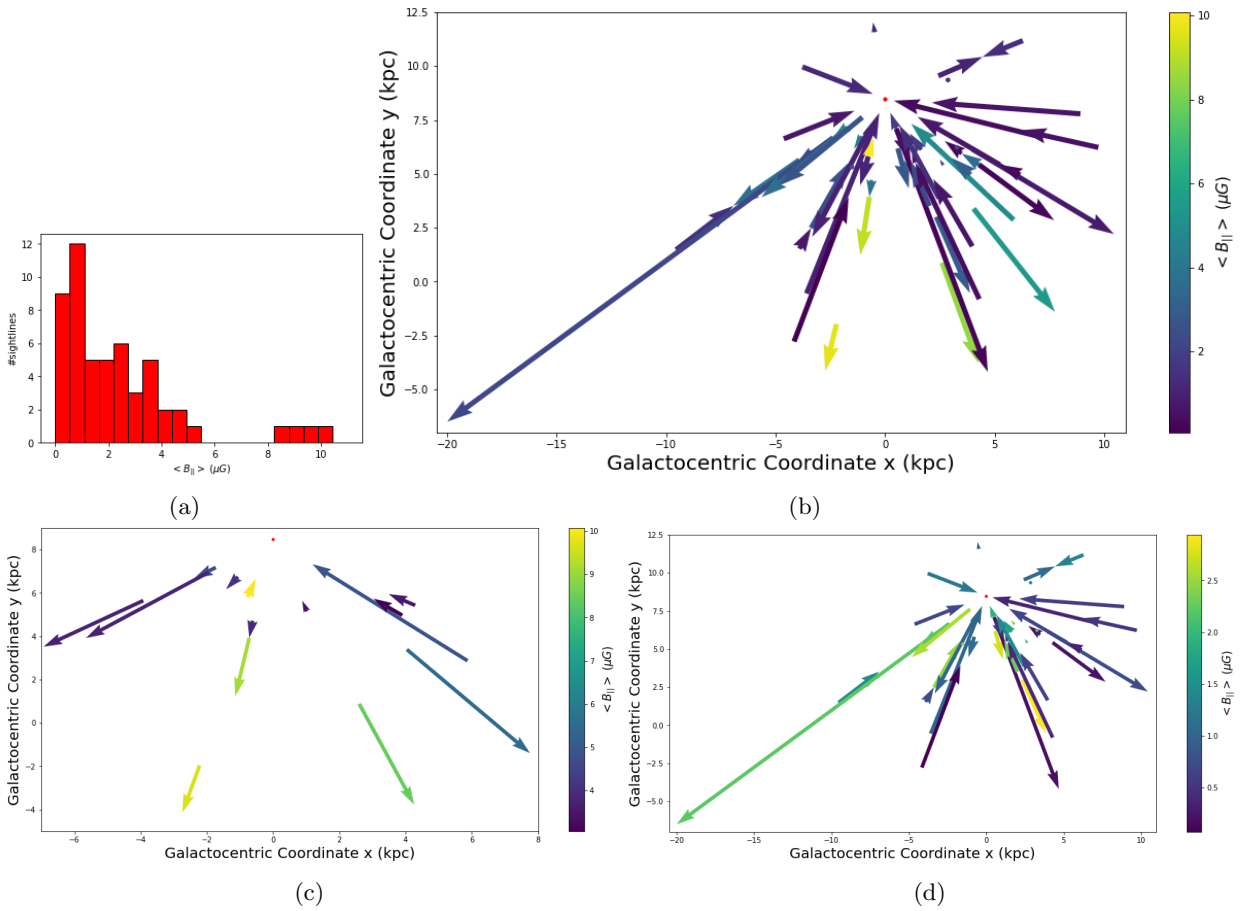

Figure 31: Determined values for the line of sight average magnetic field strength for Region 2, Method b (a) and geometric configuration (b) with separated higher ($\langle B_{\parallel} \rangle \geq 3\,\mu\text{G}$)(c) and lower ($\langle B_{\parallel} \rangle < 3\,\mu\text{G}$)(d) values.

Three in the illustration of applying Method b to Region 2 excluded sight lines are shown in Fig. 32. These sight lines correspond to magnetic field strength estimates above 20 µG. However, it may also be noted that two of them still lie below 25 µG in this case. Finally, the highest value is located rather far from the Solar position at $(0, 8.5\,\text{kpc})$.

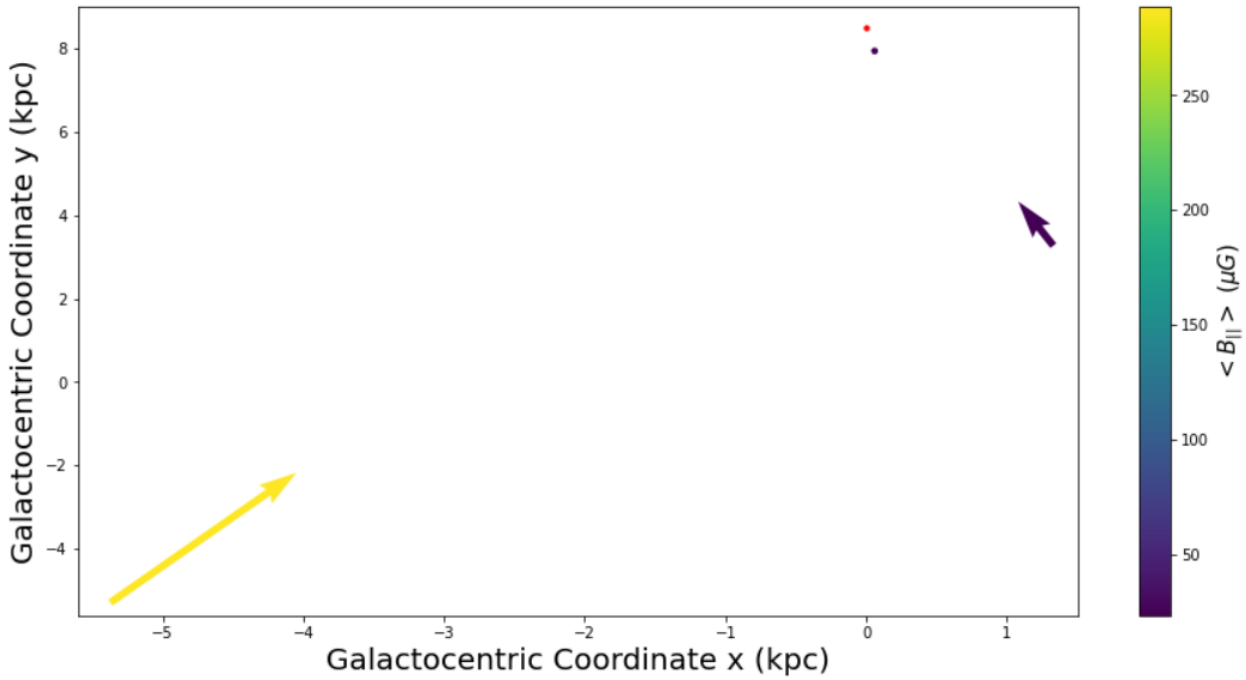

Figure 32: Determined values for the line of sight average magnetic field strength $> 20\,\mu G$ for Region 2, Method b.

4.3 Thick lower disk

The lower half of the defined thick disk is represented by region three. It includes a total number of 182 sources after applying the filtering algorithms. Sources are also located in the 'non-solar' half of the Galaxy. In addition, the included pulsars are concentrated around the Solar position and towards the inner Galaxy between Sun and GC. The geometric configuration leads to the impossibility of using Method a. Thus, this method is excluded as for the previous region.

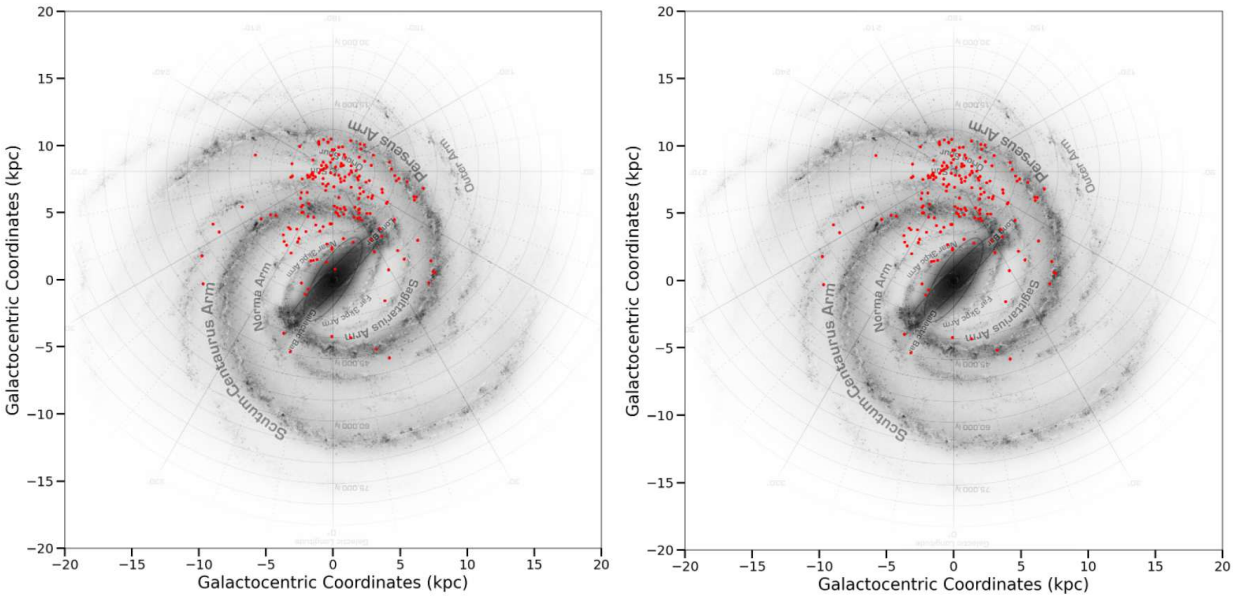

(a) (b)

Figure 33: Distribution of sources in the thick lower disk region after applying the vertical (a) and radial limits (b).

4.3.1 Two-pulsar measurement

Applying the extended binning procedure results in 53 valid sight lines. Fig. 34a shows that most $|\langle B_{\parallel}\rangle|$ estimates fall into the range of 0 to 5 µG.

A geometric representation of the obtained sight lines is depicted in Fig. 34b. Certain longitudinal ranges show higher concentrations of sight lines whereas others present a complete absence of sources.

Fig. 34c includes the range of $|\langle B_{\parallel}\rangle|$ estimates between 3 µG and 20 µG. Lower valued sight lines within this range are preferentially located towards increasing Galactocentric x-coordinate and decreasing y-coordinate with respect to the Solar position.

As in the previous regions, the lower valued sight lines in Fig. 34d present a similar arrangement to the geometric configuration of the total number of sight lines. Certain sight lines are again more populated with anisotropic orientations and varying $|\langle B_{\parallel}\rangle|$ estimates.

Finally, no sight lines with $|\langle B_{\parallel}\rangle|$ estimates larger than 20 µG are observed.

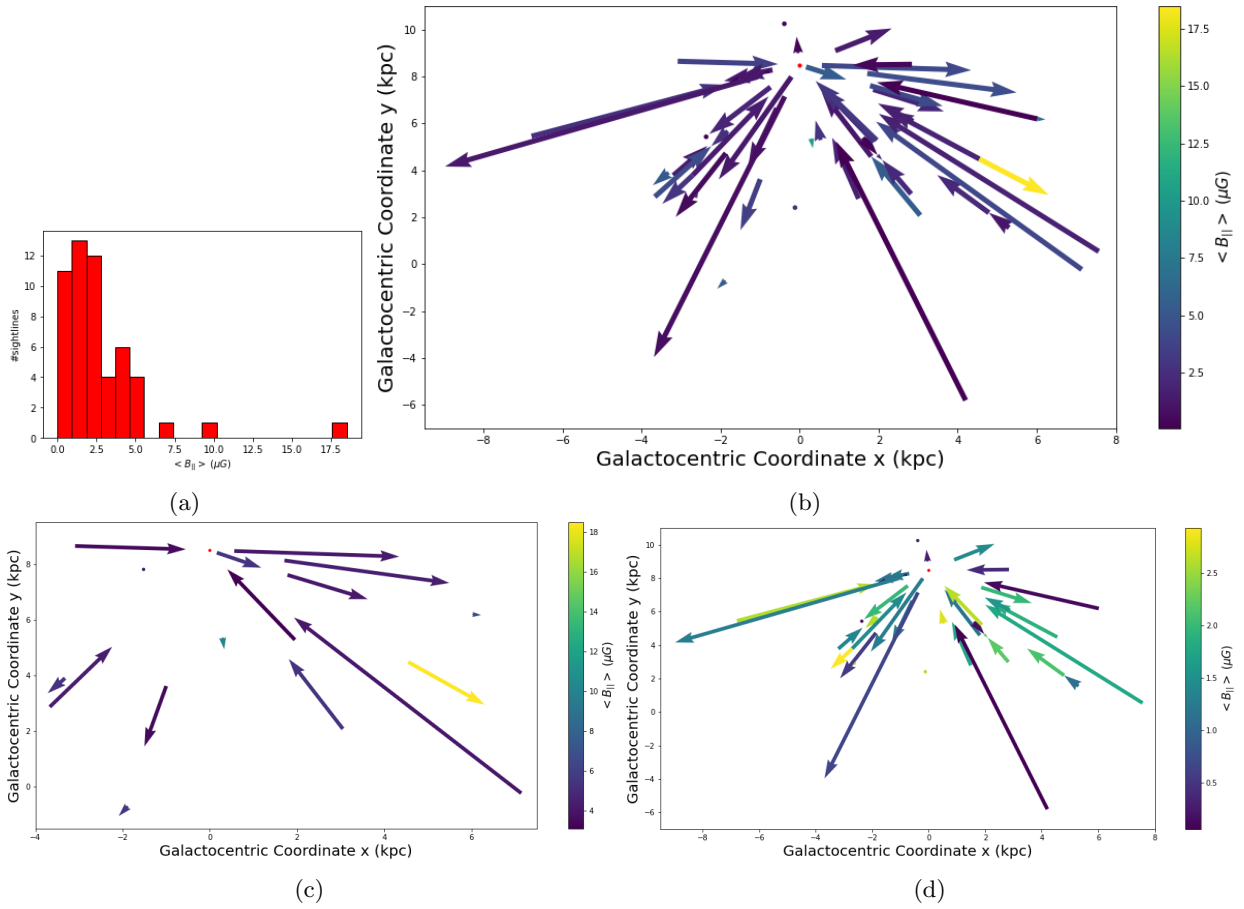

Figure 34: Determined values for the line of sight average magnetic field strength for Region 3, Method b (a) and geometric configuration (b) with separated higher ($\langle B_{\parallel} \rangle \geq 3\,\mu\mathrm{G}$)(c) and lower ($\langle B_{\parallel} \rangle < 3\,\mu\mathrm{G}$)(d) values.

4.4 Upper disk

The fourth region encompasses the upper half of the thin disk as well as the thick upper disk region. 391 sources are included in this region. The overall arrangement resembles a cone-like distribution, widening towards the GC but stopping before the central region.

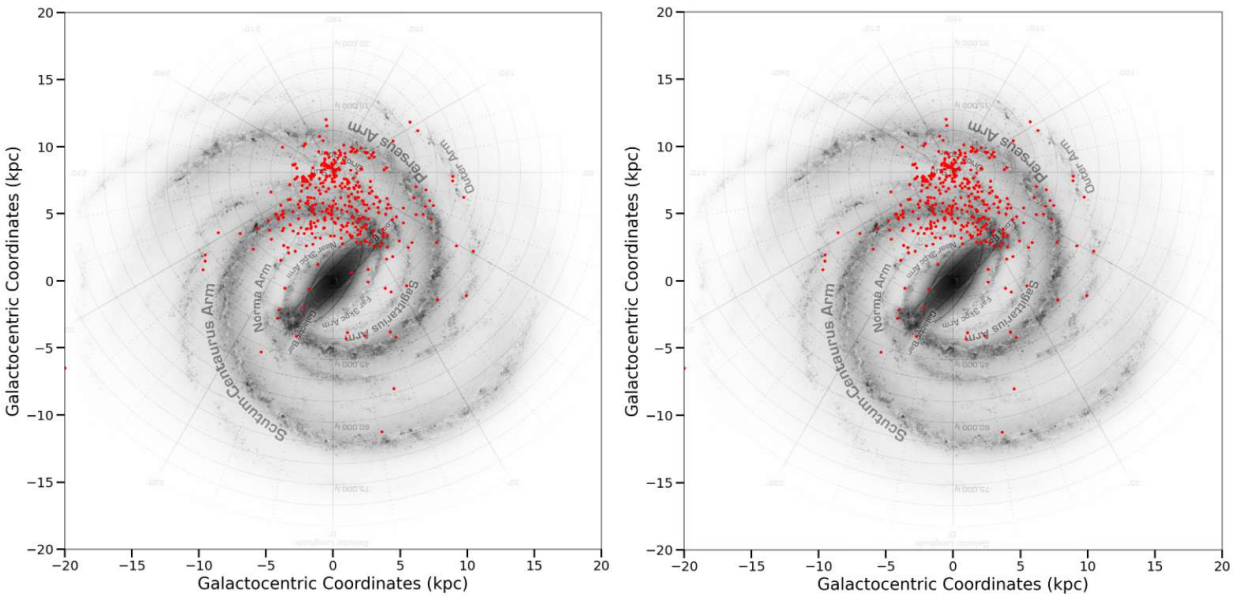

(a) (b)

Figure 35: Distribution of sources in the upper disk region after applying the vertical (a) and radial limits (b).

4.4.1 Single pulsar measurement

To apply Method a, one must first exclude the sources behind the central bar/bulge region. Thereby, the number of sources becomes 384. The number of sources within each $|\langle B_{\parallel}\rangle|$ range is represented by Fig. 36a. Their number decreases approximately exponentially with increasing $|\langle B_{\parallel}\rangle|$ after peaking between 0 and 1 µG. Furthermore, no sight lines with $|\langle B_{\parallel}\rangle|$ estimates above around 7 µG are obtained with this method.
Geometrically in Fig. 36b, most sight lines are in the quadrant towards increasing Galactocentric x-coordinate and decreasing y-coordinate and the diagonally-halved quadrant towards decreasing x-coordinate and decreasing y-coordinate with respect to the Solar position. Towards the same directions, sight line lengths or distances of the sources from the Sun are relatively long whereas sources towards the other directions are more closely spaced.
Only a few sources within the $|\langle B_{\parallel}\rangle|$ range of 3 µG to 20 µG are observed as shown in Fig. 36c. All of these are located towards increasing x-coordinate values. Furthermore, different orientations along similar sight lines are found.

Lastly, Fig. 36d depicts the lower range of line of sight average magnetic field strength estimates. Overall, the arrangement is anisotropic in terms of orientations and dispersed/mixed in terms of values. However, a tendency towards lower $|\langle B_{\parallel}\rangle|$ estimates may be observed. Considering this remark, it should be reminded that the estimates result from the averaging over an extensive line of sight distance. Thus, reversals may even out each other.

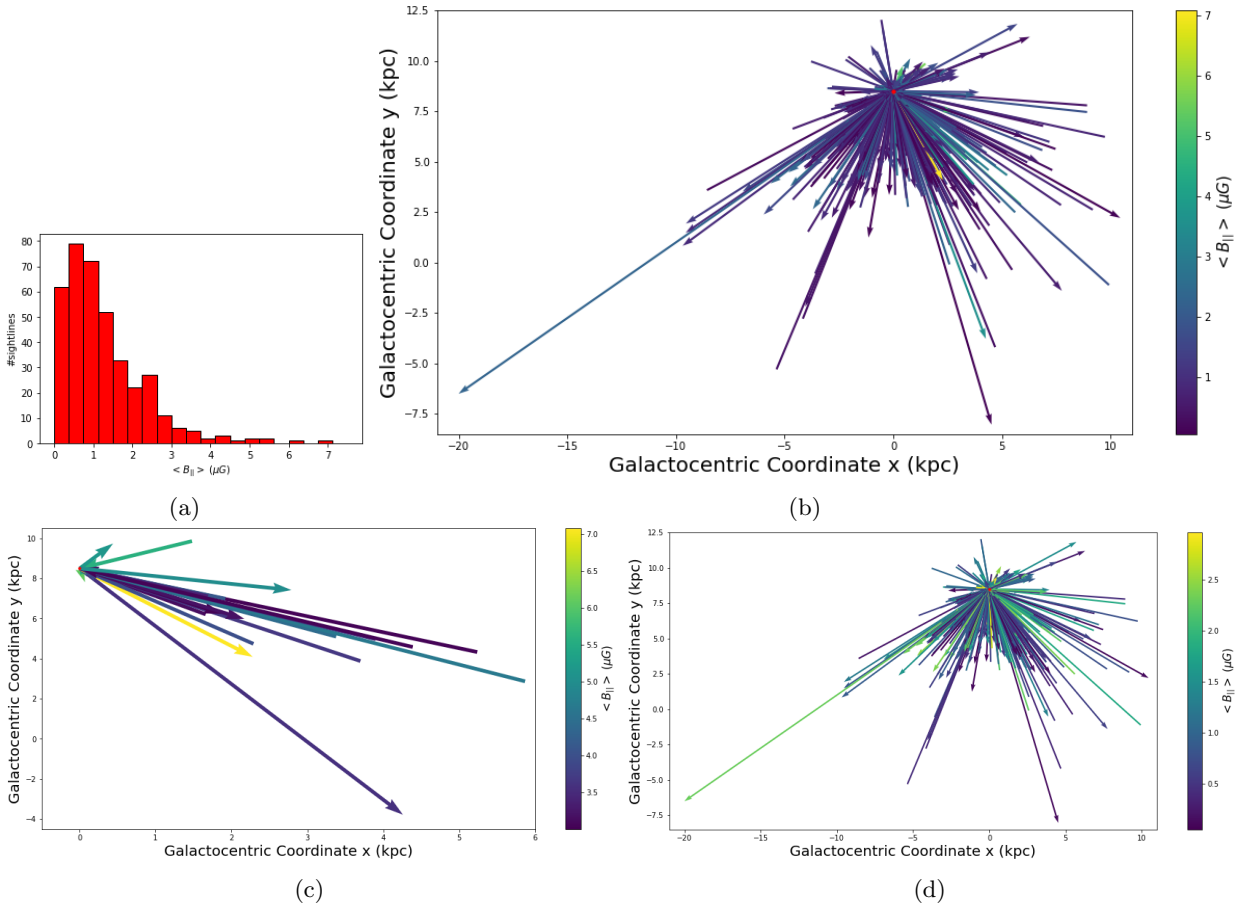

Figure 36: Determined values for the line of sight average magnetic field strength for Region 4, Method a (a) and geometric configuration (b) with separated higher ($\langle B_{\parallel} \rangle \geq 3\,\mu\mathrm{G}$)(c) and lower ($\langle B_{\parallel} \rangle < 3\,\mu\mathrm{G}$)(d) values.

4.4.2 Two-pulsar measurement

When applying Method b, the number of sources is reduced to 179 as shown in Fig. 37a. The distribution of magnetic field strength estimates peaks at the lowest shown value, around 0. Furthermore, some values reside within the upper range of $|\langle B_{\parallel}\rangle|$ values, namely above 15 µG.
Like for Method a, a significantly long sight line is found towards decreasing Galactocentric x- and y-coordinate in Fig. 37b. Other sight lines are preferentially aligned towards the quadrants towards decreasing y-coordinate. The sight lines towards increasing y-coordinate are fewer and shorter.
As can already be seen from Fig. 37a, in Fig. 37c a considerable number of sight lines with magnetic field strength estimates above 3 µG is observed. Their overall orientation is anisotropic. Some sight lines correspond to particularly short distances between the two subsequent pulsars.
Fig. 37d depicts the lower range of $|\langle B_{\parallel}\rangle|$ estimates. It may be noted that the long sight line from Fig. 37b corresponds to magnetic field strength values within this range. The general arrangement is anisotropic.

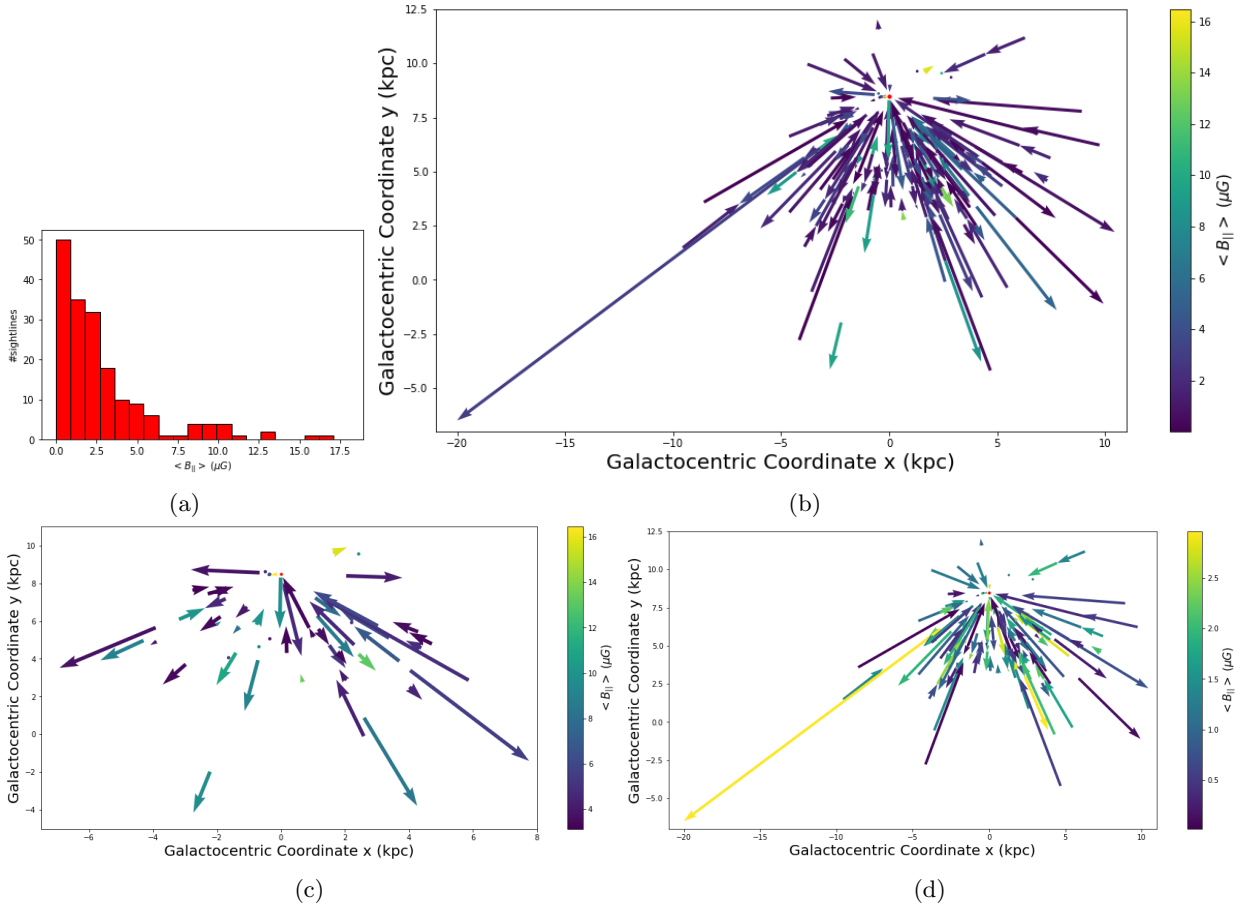

Figure 37: Determined values for the line of sight average magnetic field strength for Region 4, Method b (a) and geometric configuration (b) with separated higher ($\langle B_{\parallel}\rangle \geq 3$ µG)(c) and lower ($\langle B_{\parallel}\rangle < 3$ µG)(d) values.

In addition to the $|\langle B_{\parallel}\rangle|$ estimates between 0 and 20 µG, 15 sight lines with higher estimates are obtained for this region. These are shown in Fig. 38. The sight lines are preferentially located towards increasing Galactocentric x- and decreasing y-coordinate, as well as towards decreasing x- and decreasing y-coordinate. It may be noted that the highest value in the upper disk region with Method b corresponds to more than

400 µG.

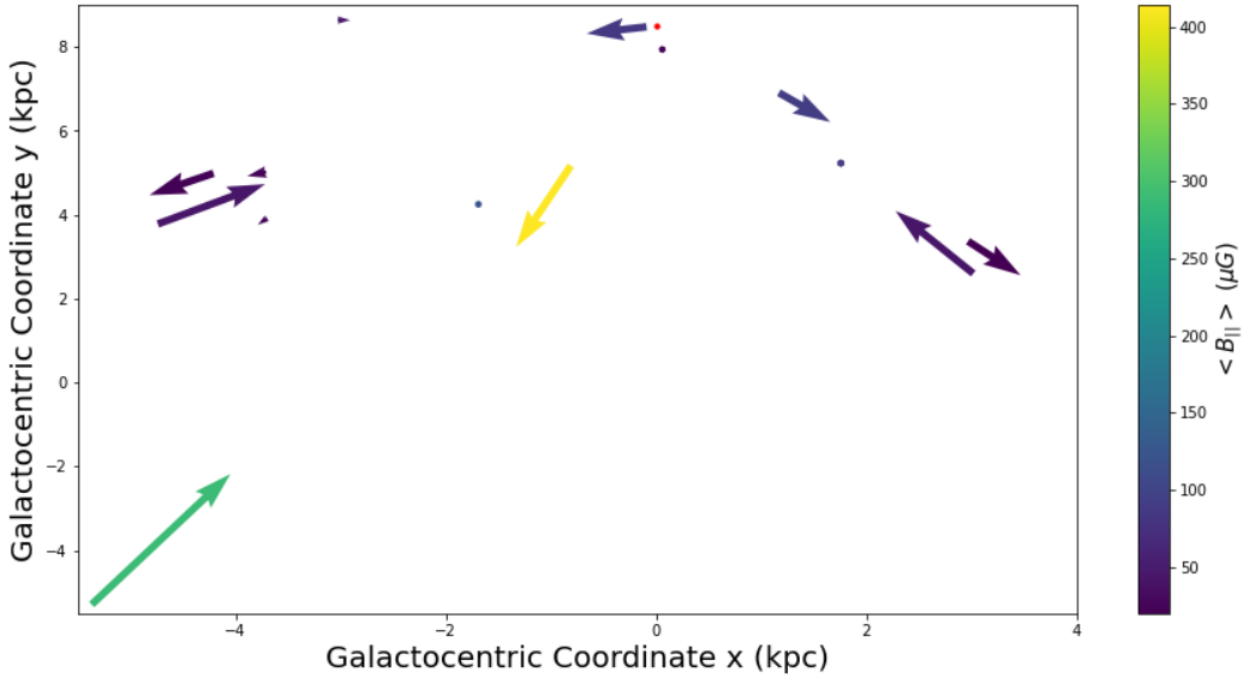

Figure 38: Determined values for the line of sight average magnetic field strength > 20 µG for Region 4, Method b.

4.5 Lower disk

The lower disk, or fifth, region includes the lower half of the thin disk region as well as the thick lower disk region. The assumption of the Sun being located within the Galactic plane at Galactocentric z-coordinate equal to zero enables the application of Method a to this region. Applying the vertical and radial limits results in 404 and 400 sources respectively. The obtained distribution of sources projected on the Galactic plane is shown in Fig. 39b. Sources are concentrated around the Solar region and show a trend of following the spiral arm structure of the Galaxy.

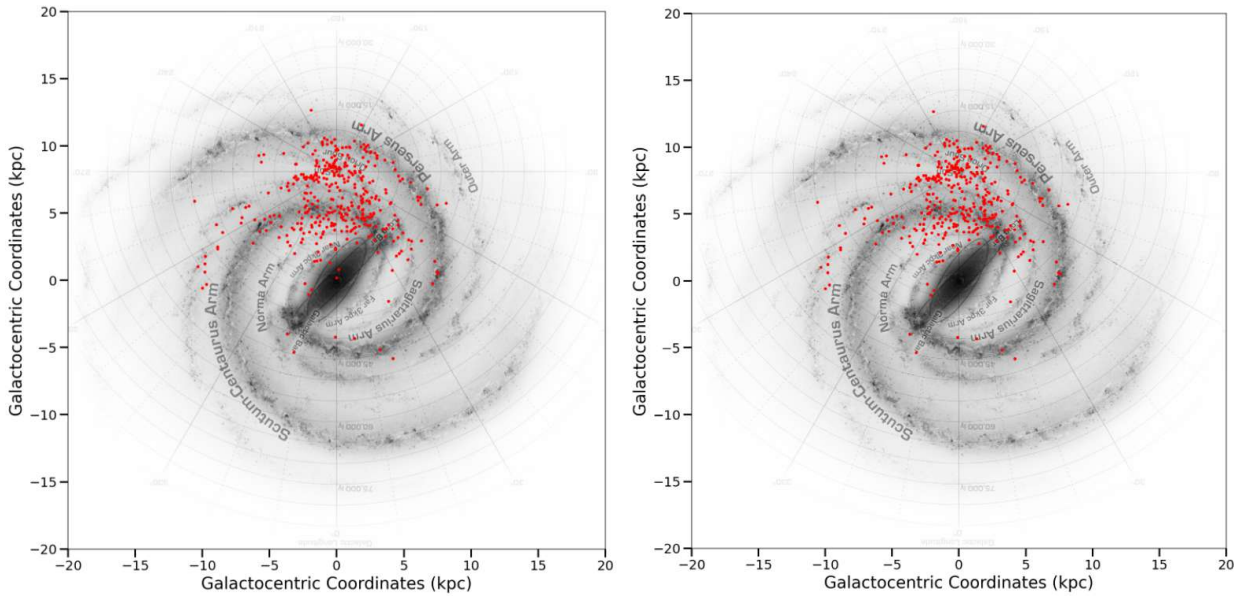

(a) (b)

Figure 39: Distribution of sources in the lower disk region after applying the vertical (a) and radial limits (b).

4.5.1 Single pulsar measurement

To apply Method a, one must first exclude the sight lines going through the bar/bulge region. Doing so leads to a decrease of the valid sight lines/sources to 394. Fig. 40a depicts the number of sight lines with respect to their average magnetic field strength value parallel to the path between the observer and the respective source. Estimates are concentrated within the lower range. Furthermore, only few sight lines show estimates with strengths above 6 µG.

The geometrical arrangement in Fig. 40b reflects the distribution of sources within the Galaxy. Orientations of the magnetic field are generally anisotropic, and no clear structure can directly observed.

Fig. 40c only includes the sight lines with $|\langle B_{\parallel} \rangle|$ estimates larger than 3 µG. The largest magnetic field strength value for this region and method corresponds to around 12 µG. Many of the sight lines with similar locations in the Galaxy show same orientations. More sight lines within the upper range of magnetic field strength estimates are found towards increasing Galactocentric x-coordinate.

Most of the sight lines shown in Fig. 40b are also shown in Fig. 40d since they correspond to the lower range of $|\langle B_{\parallel} \rangle|$ estimates. Obtained $|\langle B_{\parallel} \rangle|$ values are mixed and no clear structure within them can be immediately seen. Orientations are more anisotropic towards the GC at $(0, 0)$ compared to other directions.

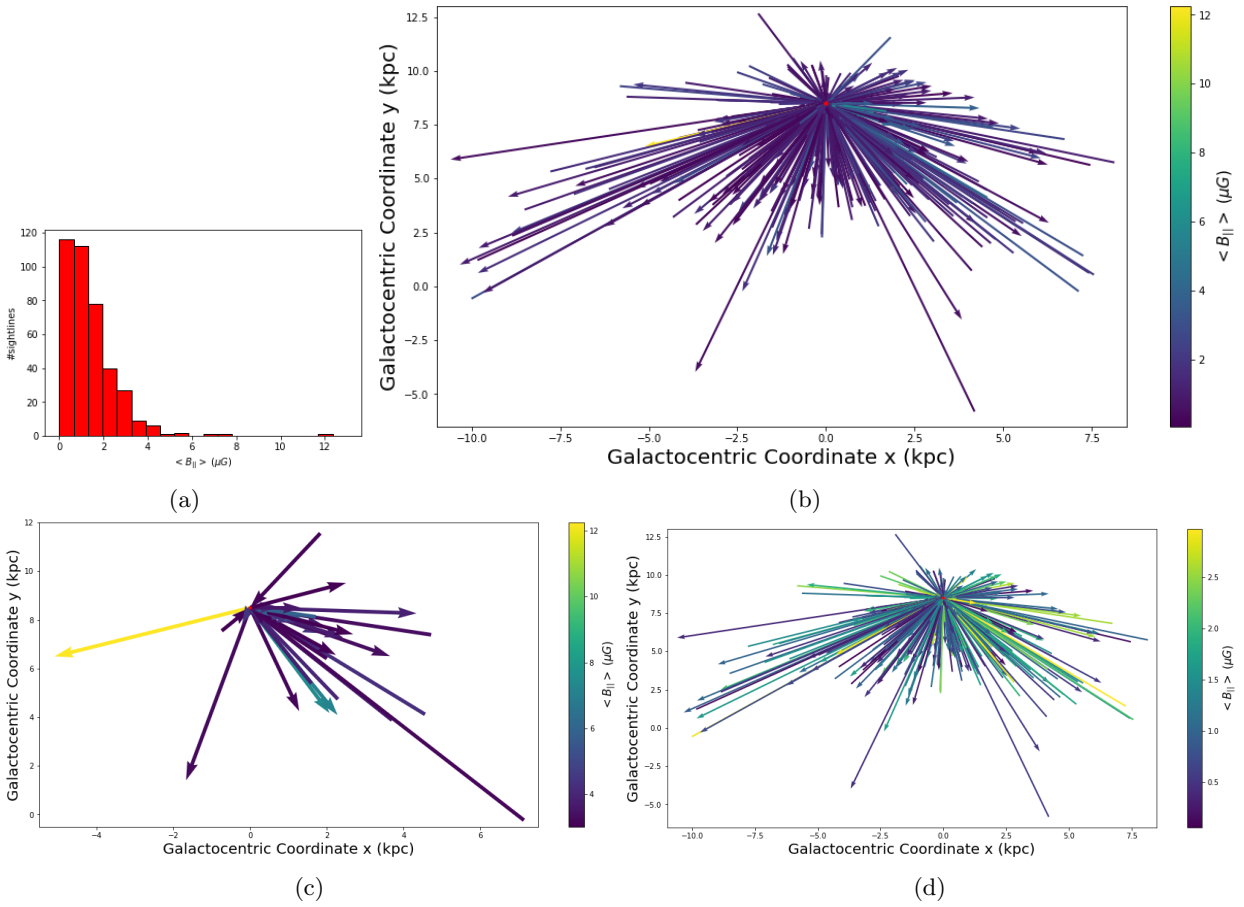

Figure 40: Determined values for the line of sight average magnetic field strength for Region 5, Method a (a) and geometric configuration (b) with separated higher ($\langle B_{\parallel} \rangle \geq 3\,\mu\mathrm{G}$)(c) and lower ($\langle B_{\parallel} \rangle < 3\,\mu\mathrm{G}$)(d) values.

4.5.2 Two-pulsar measurement

Due to the binning for Method b, less sight lines are included than for Method a. Their number thereby becomes 188. Fig. 41a shows the number of sight lines with respect to the $|\langle B_{\parallel}\rangle|$ estimates. Most sight lines show magnetic field strength estimates within the lower range up to around 5 µG. It may be noted that higher values than for applying Method a are reached.
Fig. 41b depicts the geometrical arrangement of all used sight lines up to values of the 'differentially' obtained magnetic field strength estimates of 20 µG. Shorter vectors with anisotropic orientations can be especially found towards the inner Galaxy. Only few sight lines are observed towards the Galactic Anticenter. Furthermore, many short vectors in terms of distance between two pulsars are present and concentrated in relatively small regions.
Sight lines with corresponding magnetic field strength estimates within the upper range between 3 and 20 µG are presented in Fig. 41c. These include several relatively small-scale estimates. Furthermore, many longitudinal ranges show large anisotropy in terms of $\langle B_{\parallel}\rangle$ orientations. The highest obtained values are around 18 µG.
Finally, Fig. 41d shows the geometrical arrangement of sight lines with $|\langle B_{\parallel}\rangle|$ estimates up to 3 µG. Most sight lines are located towards decreasing Galactocentric y-coordinate with respect to the assumed Solar position at $(0, 8.5\,\mathrm{kpc})$. The sight lines present a large variety of lengths and orientations with again, no clear structure.

In addition to the 'differentially' obtained $|\langle B_{\parallel}\rangle|$ estimates with values below 20 µG, eight sight lines with higher magnetic field strength estimates are found and shown in Fig. 42. These sight lines are comparably point-like in terms of length or distance between subsequent pulsars. The highest estimate corresponds to around 382 µG. All but two 'extreme' sight lines are located towards decreasing Galactocentric x-coordinate with respect to the assumed Solar position.

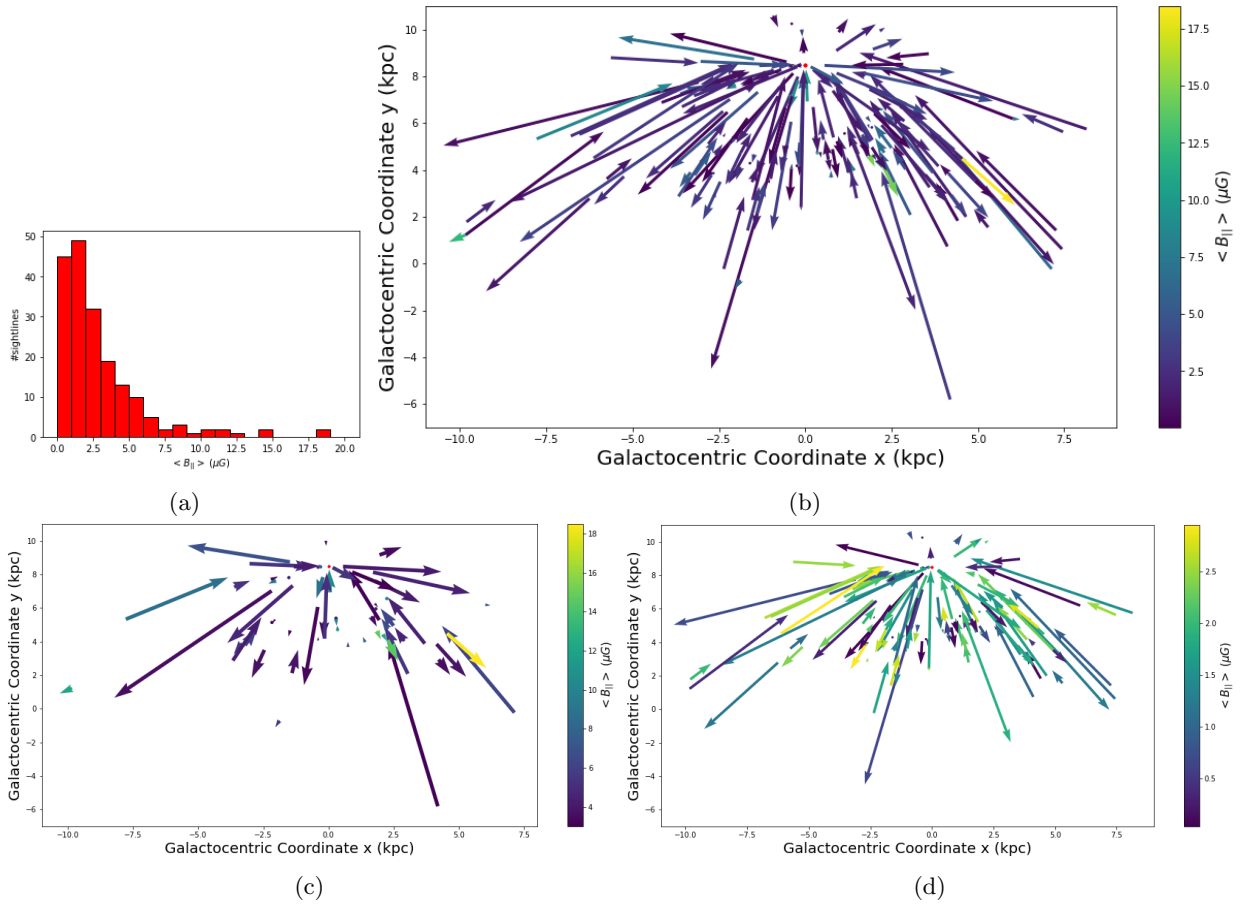

Figure 41: Determined values for the line of sight average magnetic field strength for Region 5, Method b (a) and geometric configuration (b) with separated higher ($\langle B_{\parallel} \rangle \geq 3\,\mu\mathrm{G}$)(c) and lower ($\langle B_{\parallel} \rangle < 3\,\mu\mathrm{G}$)(d) values.

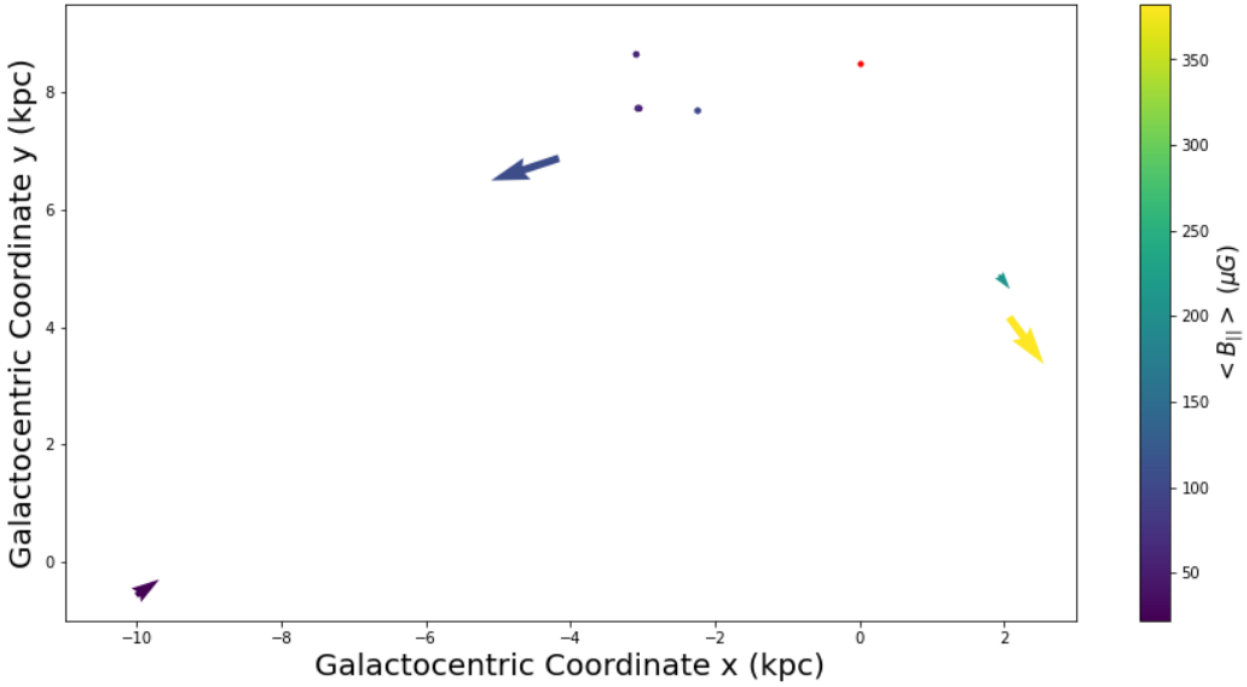

Figure 42: Determined values for the line of sight average magnetic field strength $> 20\,\mu G$ for Region 5, Method b.

4.6 Upper halo

Region 6 corresponds to the upper halo region. Since the application does not change when applying the radial limit after the limit in the z-coordinate, only the distribution obtained after applying the former one is shown in Fig. 43. Overall, the sources are strongly focused on the Solar position as well as around the expected spiral arm structure. Since the Sun is not expected to lie within this region, one cannot apply Method a to the sources in this region.

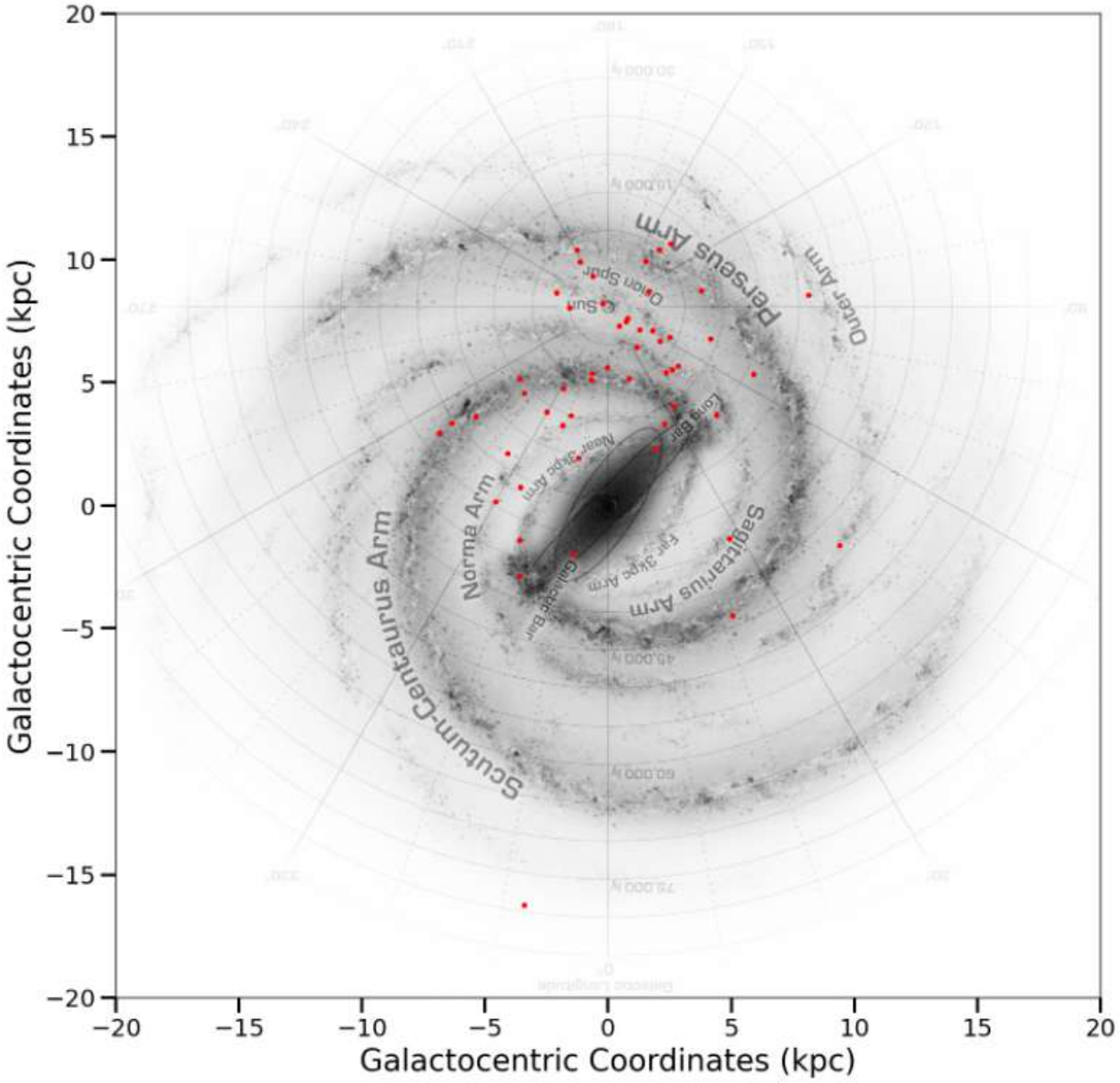

Figure 43: Distribution of sources in the lower disk region after applying the vertical and radial limits.

4.6.1 Two-pulsar measurement

Fig. 44a depicts the distribution of magnetic field strength values in this region obtained with Method b. It may be however noted that the dwindling number of valid sight lines, namely seven, does result in a strongly

questionable significance of this distribution. Thus, it is rather shown for the sake of completeness. The maximum obtained value resides around 8 µG

As for the other regions, Fig. 44b shows the geometric arrangement of the different sight lines in Galactocentric coordinates as well as their respective $|\langle B_{\parallel}\rangle|$ estimate and orientation. These sight lines are mostly isolated except for a group of four sight lines towards increasing x- and decreasing y-coordinate with respect to the Solar position.

Fig. 44c and Fig. 44d separately depict the sight lines showing larger $\left(3\,\mu\text{G} \leq |\langle B_{\parallel}\rangle| < 20\,\mu\text{G}\right)$ and smaller $\left(|\langle B_{\parallel}\rangle| < 3\,\mu\text{G}\right)$ magnetic field strength estimates respectively.

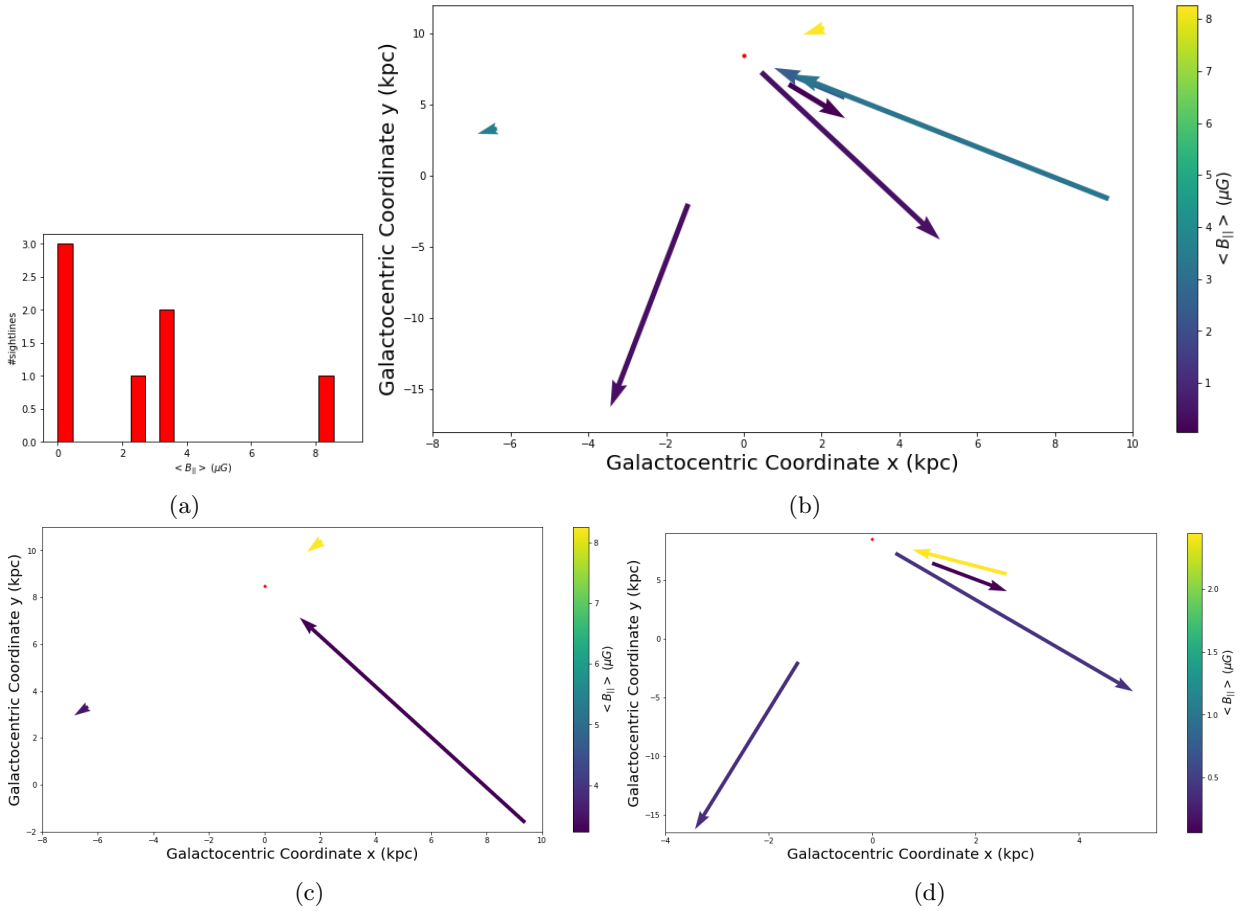

Figure 44: Determined values for the line of sight average magnetic field strength for Region 6, Method b (a) and geometric configuration (b) with separated higher $(\langle B_{\parallel}\rangle \geq 3\,\mu\text{G})$(c) and lower $(\langle B_{\parallel}\rangle < 3\,\mu\text{G})$(d) values.

One sight line is found in the upper halo region with $\left(|\langle B_{\parallel}\rangle|\right)$ estimate above 20 µG. It is shown in Fig. 59 in Appendix B with corresponding pulsars within 1 kpc of the Sun in Galactocentric x-coordinate.

4.7 Lower halo

Differently to the previous region, region seven shows changes in the number of applicable sources also for the application of the radial limits. The region represents the lower halo, and the final number of valid sources corresponds to sixty pulsars as shown in Fig. 45b. These are concentrated around the Solar position and roughly follow the assumed spiral arm structure farther away.

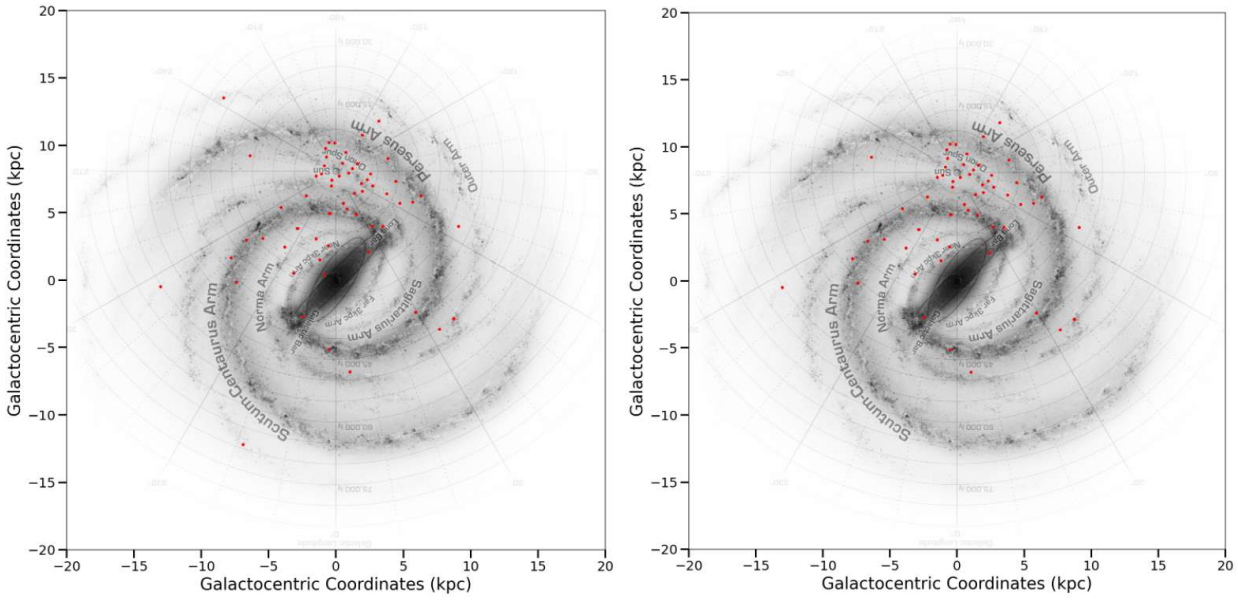

(a) (b)

Figure 45: Distribution of sources in the lower halo region after applying the vertical (a) and radial limits (b).

4.7.1 Two-pulsar measurement

As for the previous region, the small number of applicable sight lines, namely six, result in the histogram of magnetic field strength estimates in Fig. 46a not having statistical significance. The maximum observed $|\langle B_{\parallel} \rangle|$ estimate lies between 6 and 7 µG in this case.

The whole geometrical distribution of sight lines is shown in Fig. 46b. No sight line towards the Galaxy Anticenter nor towards the GC with respect to the assumed Solar position is observed. Two sight lines towards increasing x-coordinate with respect to the Solar position show the same orientation. The results should however be treated carefully due to the dwindling number of available sight lines.

Fig. 46c and Fig. 46d present the higher and lower magnetic field strength estimates separate respectively as for the previous sections.

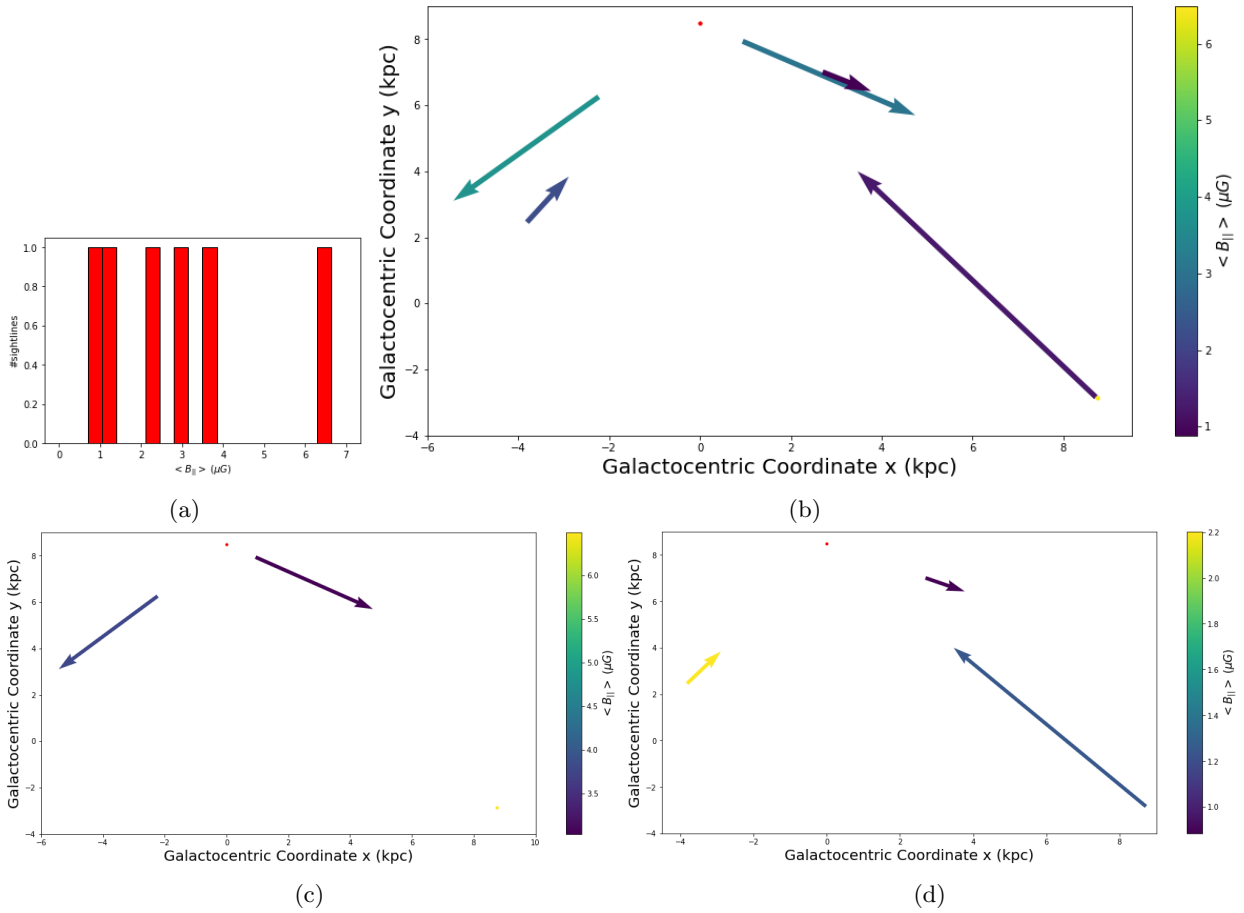

Figure 46: Determined values for the line of sight average magnetic field strength for Region 7, Method b (a) and geometric configuration (b) with separated higher ($\langle B_{\parallel} \rangle \geq 3\,\mu\mathrm{G}$)(c) and lower ($\langle B_{\parallel} \rangle < 3\,\mu\mathrm{G}$)(d) values.

4.8 Bar/Bulge

The penultimate region represents the vertically limited Bar/Bulge region. Its overall distribution of sources is shown in Fig. 47. Due to the radial boundaries, only two pulsars are found in this region. It is thus immediately predictable that only Method a can be properly applied to this region. Due to this circumstance, Method a is applied, even though the Sun does not reside within this region and thus other regions than the central region, notably along the path between the Solar position at $(0, 8.5\,\mathrm{kpc})$ and the central region, are effectively also included.

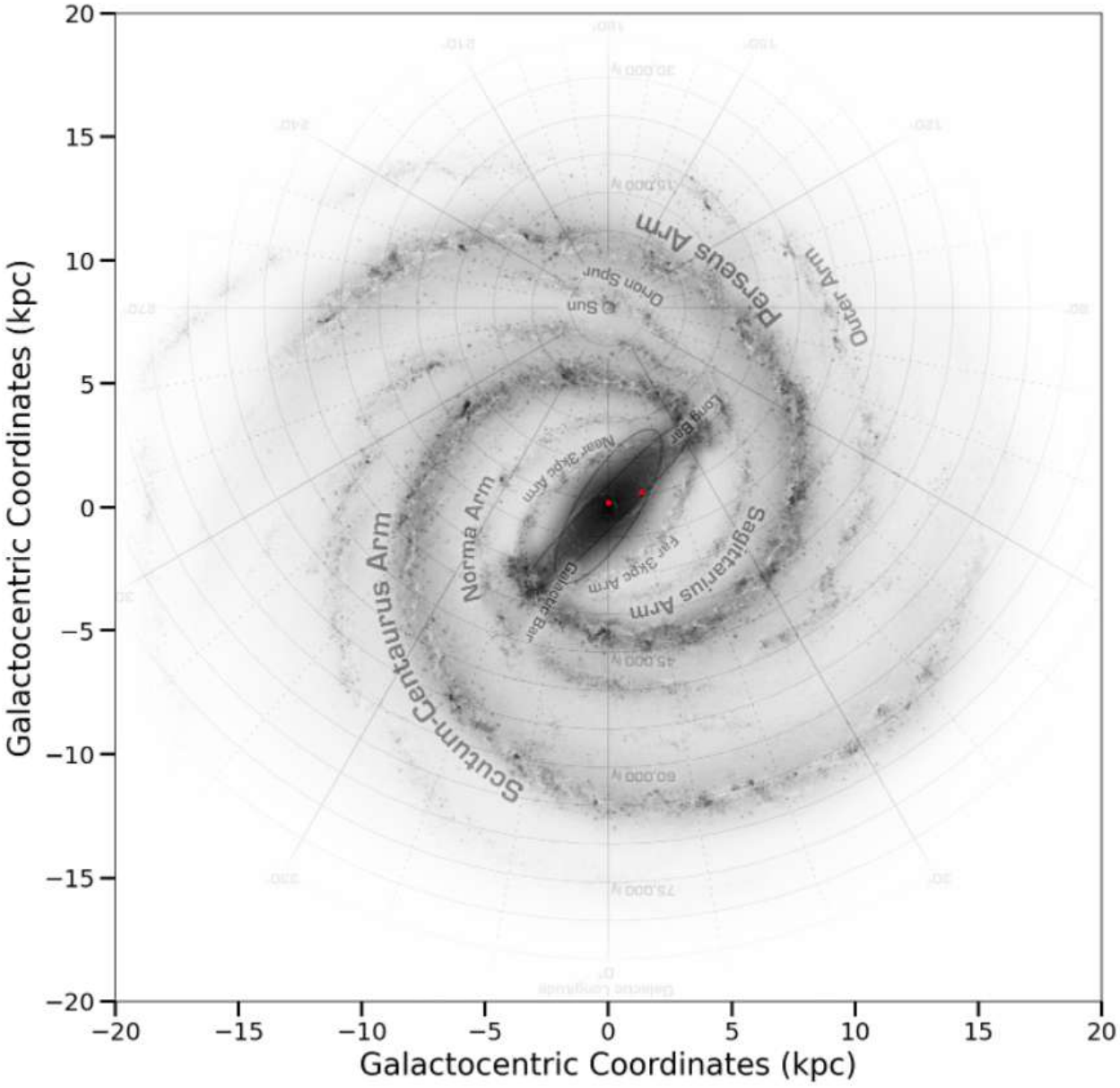

Figure 47: Distribution of sources in the bar/bulge region after applying the vertical and radial limits.

4.8.1 Single pulsar measurement

Different $|\langle B_{\parallel} \rangle|$ estimates, corresponding to the two sight lines are presented in Fig. 48a. They may be divided into one rather usual and one 'ultra-high' value. Their geometrical arrangement is depicted in Fig. 48b. The location of the start or end point is clearly located within the defined central region of the Galaxy.

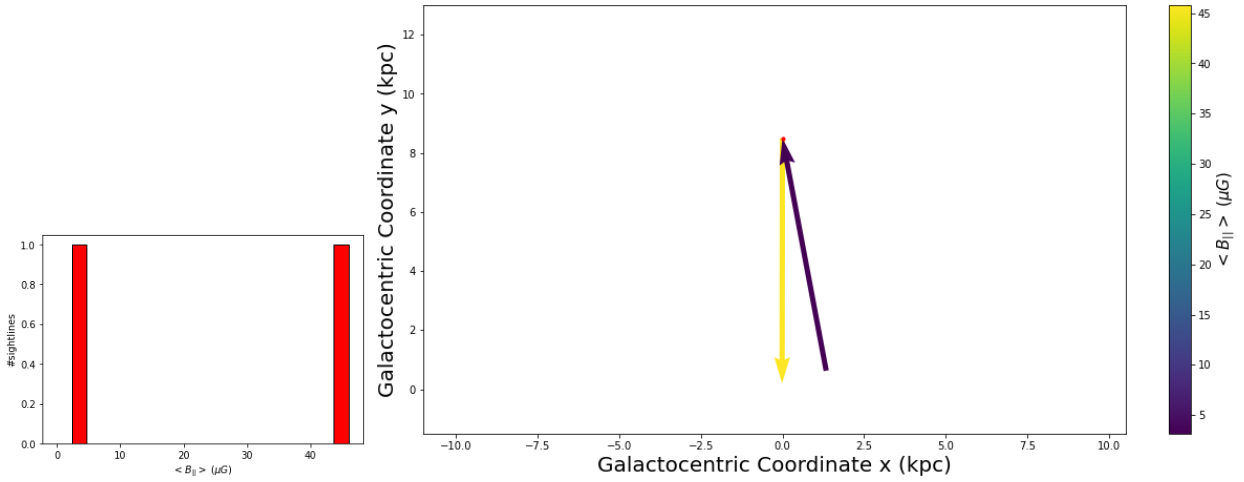

(a) (b)

Figure 48: Determined values for the line of sight average magnetic field strength for Region 8, Method a (a) and geometric configuration (b).

4.9 Extended Bar/Bulge

To include the entire central region that is usually excluded in all defined regions except partly not in the Bar/Bulge region, an additional region is defined. This definition results in an increase in the number of valid sources from two to five pulsars compared to the previous region. It may be noted that all the added sources are located at larger Galactocentric z-coordinate or distance from the Galactic plane than the previously obtained two sources. Their positions projected on the Galactic disk are shown in Fig. 49.

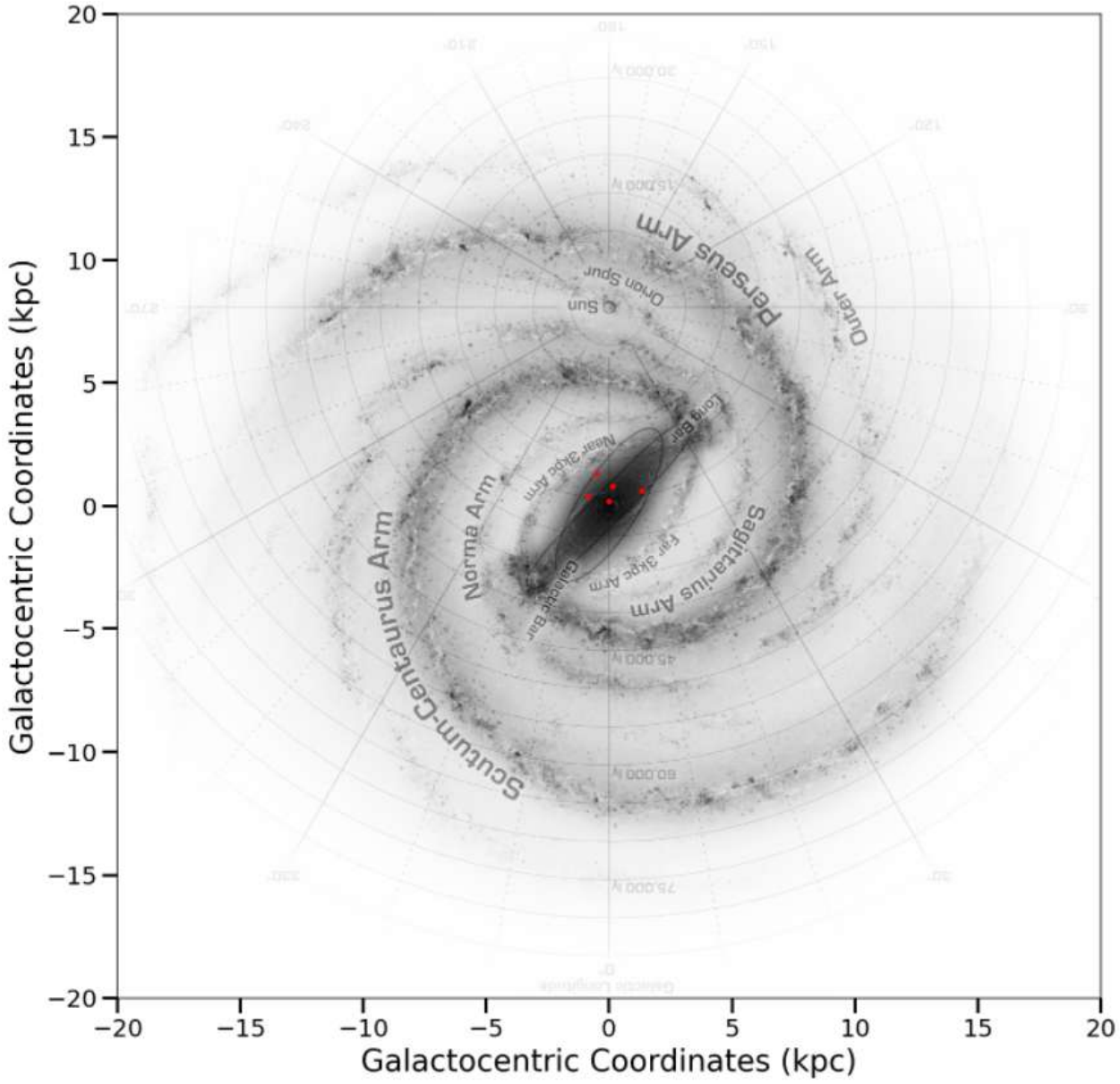

Figure 49: Distribution of sources in the bar/bulge region after applying the and radial limits.

4.9.1 Single pulsar measurement

Fig. 50a depicts the distribution of $|\langle B_{\parallel} \rangle|$ estimates within this region. The added sources provide estimates within the lower range of values. Finally, Fig. 50b shows the geometric arrangement of the included sight lines. One newly added sight line lies between the previous two sight lines whereas the other two are located towards decreasing Galactocentric x-coordinate with respect to the Solar position. Furthermore, the sources at higher vertical position provide lower $|\langle B_{\parallel} \rangle|$ estimates than the other two sight lines.

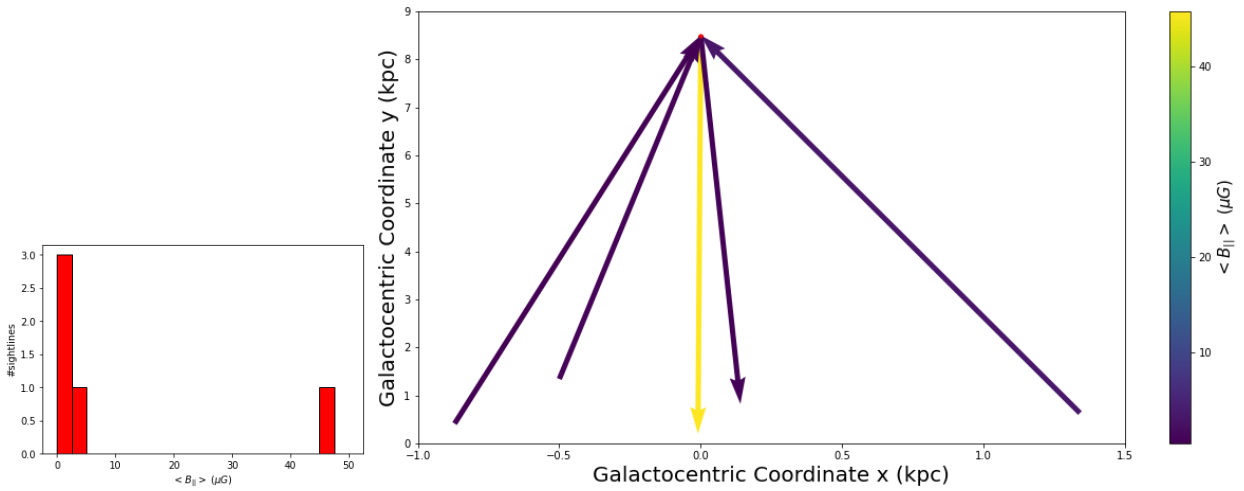

(a) (b)

Figure 50: Determined values for the line of sight average magnetic field strength for Region 8+, Method a (a) and geometric configuration (b).

5 Discussion

In the following, the different results are discussed in the context of the questions introduced in section 2.4.

5.1 Galactic Magnetic Field strength

In case of the thin disk region, pulsars present a wide distribution in the Galactic plane as may be seen in Fig. 51. Furthermore, when using Method a, the relatively long sight lines result in different contributions compensating each other over the whole path between the Solar and the pulsar's position. This allows for the study of the average magnetic field strength of this region. Since the distribution of $\langle B_{\parallel} \rangle$ estimates peaks around zero, positive and negative magnetic fields contribute approximately the same along the observed paths. A qualitative estimate of the large-scale average thin disk magnetic field strength may then be given as $B_{\mathrm{gal}} \approx 0 - 2\,\mu\mathrm{G}$. This value agrees with other studies, providing estimates equal to $1.7 \pm 1\,\mu\mathrm{G}$ (Mitra et al., 2003), $\approx 1 - 2\,\mu\mathrm{G}$ (Beck and Wielebinski, 2013), or $\sim 2\,\mu\mathrm{G}$ (Noutsos et al., 2008) for the regular, large-scale magnetic field's strength. The small number of sight lines with $\langle B_{\parallel} \rangle$ estimates larger than $3\,\mu\mathrm{G}$ indicates that, on large-scale, the GMF is not dominated by small-scale features which may provide large magnetic field strength estimates as shown in Fig. 52 and addressed later in this section. Regarding the study of the same region with Method b, it may be noted that the weaker field towards the outer Galaxy may result from the bad alignment of the few sources in this direction with respect to the magnetic field. Thereby, they only probe a small fraction of the magnetic field strength and do not allow for an estimation of the full strength. Further investigation of this region with notably a larger number of sources is required.

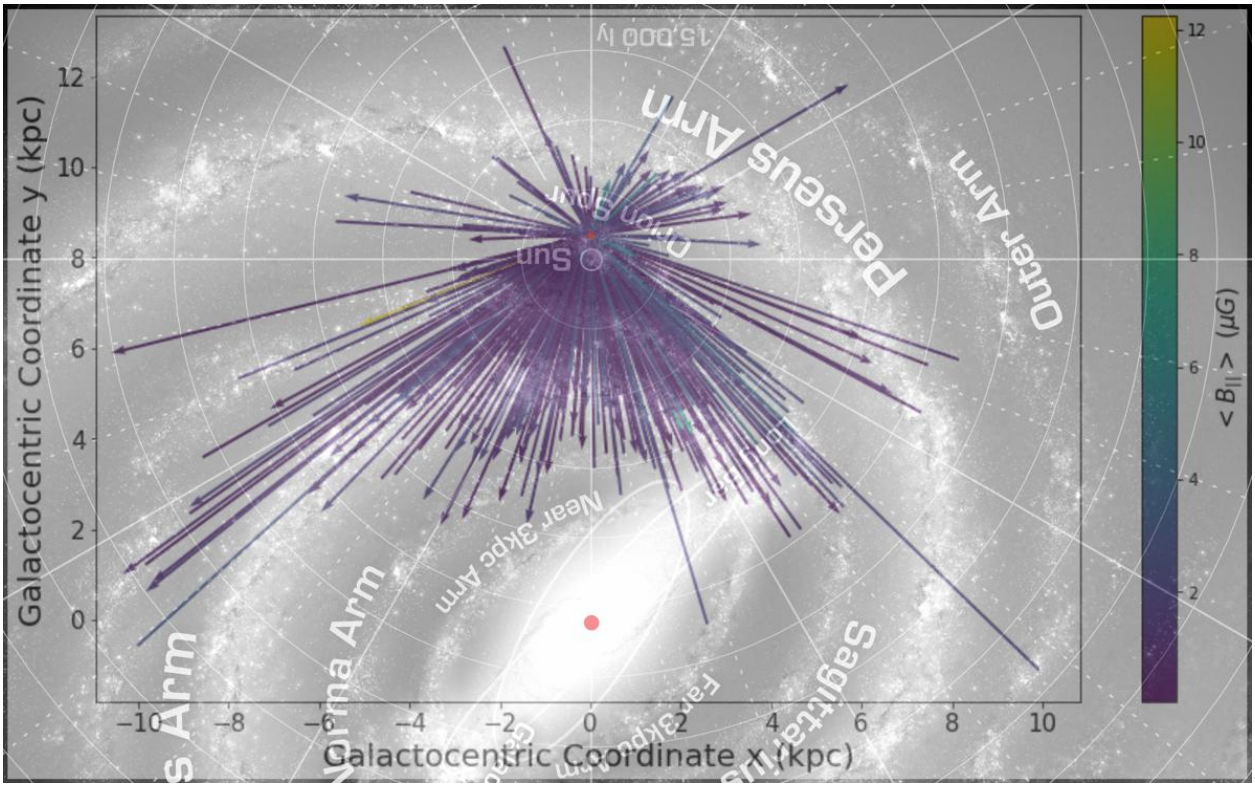

Figure 51: Results for Region 1, Method a, overplotted on the modified previously used image of the Galactic structure.

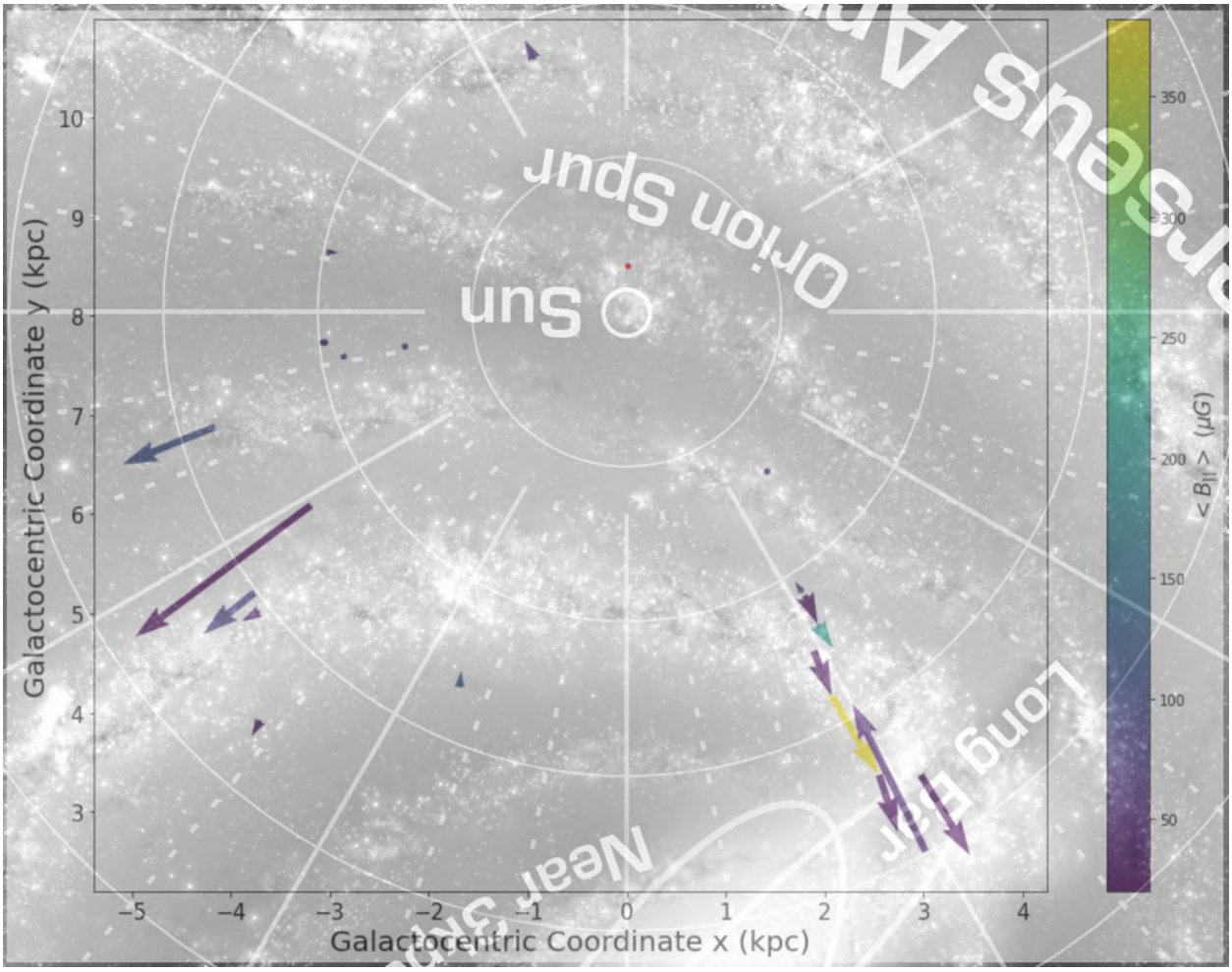

Figure 52: Results with 'ultra-high' $|\langle B_{\parallel} \rangle|$ estimates for Region 1, Method b, overplotted on the modified previously used image of the Galactic structure.

The analysis of the upper thick disk region indicates a large-scale magnetic field strength of around $B_{\mathrm{gal}} \approx 2\,\mu\mathrm{G}$ as for the previous region. Thus, the same magnetic field may dominate up to a vertical extension of 800 pc instead of only 140 pc.

Like the upper thick disk region, the lower thick disk region supports a large-scale magnetic field in the Galaxy of less than $B_{\mathrm{gal}} \approx 5\,\mu\mathrm{G}$. Furthermore, the anisotropic structure of the lower magnetic field strength estimates indicates a turbulent field with similar strength as the large-scale magnetic field.

The similar strength for the turbulent field ($B_{\mathrm{turbulent}} \approx 2\,\mu\mathrm{G}$) with respect to the large-scale field is also supported by the sight lines of varying orientation towards the GC in the upper disk region.

Studying the lower disk region provides similar $\langle B_{\parallel} \rangle$ estimates for both orientations as well as a distribution of them around zero. This indicates both components being of approximately the same strength. Moreover, the fact that most estimates lie between 0 and 2 µG suggests a low strength of the large-scale magnetic field. Values for shorter sight lines provide higher estimates, indicating more local features with stronger magnetic fields.

In addition to the generally low magnetic field strength, some exceptions are found in various regions which are discussed in the following. It may be noted that a list of sight lines with 'ultra-high' magnetic field

strength estimates, obtained using differential measurements (Method b), is given by Tab. 6 in Appendix B. 'Ultra-high' results for applying Method b to the thin disk region are depicted in Fig. 52. The sketch in Fig. 53 shows the difference in the integration paths for Method a in contrast to Method b. Most striking is the significantly shorter integration path when using Method b. Thereby, this method is more sensitive to local features and the assumption of the measured DM and RM being almost exclusively affected by the characteristics of the ISM may not hold anymore. The ISM may even only constitute a small fraction of the two measured quantities. This property of Method b can potentially cause trouble in the estimation of the magnetic field.

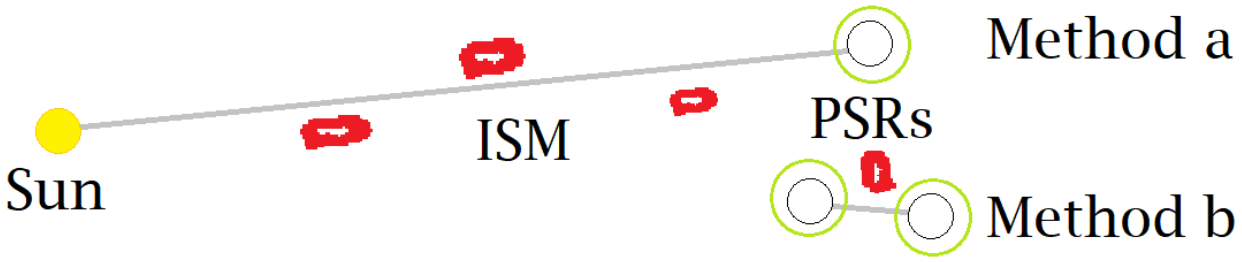

Figure 53: Sketch to represent the difference in integration path (grey) and the corresponding higher sensitivity to local ISM (red) and pulsar (green) (e.g., magnetosphere or Pulsar Wind Nebula) contributions for Method a and b.

A specific case of high magnetic field value for the sight line towards the GC (Fig. 48b and 50b) deserves further discussion. This sight line corresponds to the pulsar J1745-2900 with a magnetic field strength estimate of about 46 µG (full sight line, Method a). This value is in agreement with the results published in previous studies. According to their authors, several explanations for this unexpectedly high value are possible for this specific case. It may be entirely produced by a single HII region along the line of sight with a magnetic field of $B \approx 15$ to 70 µG (Sicheneder and Dexter, 2017). Another explanation is the influence of fluctuations of the field in the GC region due to changes in strength or orientation. These fluctuations are expected to correspond to ~ 12 µG at ~ 2 AU scales to up to ~ 400 µG at ~ 300 AU scales (Desvignes et al., 2018). A different justification for the large and time-variable RM is given by the influence of magnetised wind-wind shocks of nearby stars in the clockwise stellar disk (Ressler et al., 2019). The last reasoning connects the large RM to either the change in the magnetic field and density of a nebular filament on the line of sight or the motion of this kind of filament across the line of sight. Such a behaviour may be unrelated to the black hole at the centre of the Galaxy and rather be connected to the environment of the source on scales $\ll 0.1$ pc. This could also point to a distinct class of objects which is characterised by its RM behaviour (Katz, 2021). Thus, numerous viable explanations are available for a single object but vary between different objects, notably depending on their immediate environment and location in the large-scale structure of the Galaxy which is discussed in section 5.2.

Using Method c, a different example of a rather high magnetic field strength estimate is found for the relatively long interarm region between the Norma and the Scutum-Centaurus arm (for the Galactic structure, see Fig. 28a). In fact, Noutsos et al. (2008) find a negative spike in their magnetic field strength estimation for this region which may be explained by a significant increase in the RM in combination with a small electron density change in this region. They propose two possibilities for the origin of this feature. Either the turbulent component of the GMF or a HII region which leads to a steep electron density gradient and thus affects the measured RM. Correlation between electron density and magnetic field are also further discussed

in section 5.2.

5.2 Galactic Magnetic Field structure

The second question focuses on the overall structure of the GMF. Fig. 51 shows that the regions of higher sight line concentration in the thin disk region for Method a correspond mostly to the Galactic arms. They thus support the assumed arm model since pulsars are expected to be born in these regions. The particularly long sight line in the upper disk region towards the Galactic radius of around 20 kpc as shown in Fig. 54 points to a large-scale field of similar strength and direction along the path. It is crossing numerous arms while being oriented along them which suggests a counterclockwise orientation of the large-scale magnetic fields in the arms except for the outermost where the alignment does not hold. Estimates from the lower thick disk region with Method b support the alignment of larger values to a preferential structure/orientation in the solar vicinity which may be attributed to a spiral structure of the large-scale magnetic field. The lower disk region with Method a presents lower $|\langle B_{\text{large-scale}}\rangle|$ estimates with regions of preferred direction towards increasing galactocentric x- and y-coordinate. This configuration may also be connected to the large-scale magnetic field dominated arm as shown in Fig. 55. Support to this hypothesis comes from the same trend in this direction for the upper disk region, suggesting furthermore, a large vertical extension of this feature as well as a symmetry between the region above and below the Galactic plane. The absence of a clear signature of this trend in the results of Method b for the lower disk may be attributed to the small number of sight lines. Studying the upper disk region using Method b shows large anisotropy, suggesting a large-scale field more aligned to the Galactic disk/plane since the probed sight lines are less parallel to the Galactic plane and thus more sensitive to the turbulent GMF component compared to the large-scale component which only contributes fractionally. All regions related to the Galactic disk support the large-scale spiral structure of the GMF and an alignment of the latter with the Galactic plane. The different indicated structure with respect to the proposed spiral shape in the Bar/Bulge regions strengthens the second statement. It should however be emphasised that the sparse population of the latter regions inhibits a clear analysis, but notably Jansson et al. (2009) indicate a separation between the disk and halo field of which the Bar/Bulge region is part. The predominance of the large-scale field in the local region within the spiral arm directions is generally supported by many studies which mostly also suggest the found counterclockwise field in the local solar region (see e.g., Manchester, 1974; Rand and Lyne, 1994; Han et al., 2006).

The small number of sight lines towards the outer Galaxy may be explained by the preferred pulsar location along the spiral arms as shown in Fig. 56, with a gradually more abundant population as one considers inner parts of the Galaxy. Furthermore, low magnetic field strength estimates in this direction result from the less likely alignment of the line of sight with the field direction along the mentioned spiral arms.

The largely anisotropic arrangement when applying Method b to the thin disk region resembles the “striated” random field structure as introduced in section 2.3.3. This is especially striking for sight lines towards the GC region. In this direction, varying orientations for the upper disk region also point to the random field since the large-scale field with its spiral structure is expected to be oriented perpendicular to the respective sight lines and is therefore not contributing to the measurements. In the lower disk region, sight lines towards the GC are also approximately perpendicular to the assumed spiral structure and thus the turbulent component of the GMF dominates here. Devoting this trend to a turbulent field rather than small-scale local features is supported by the absence of extremely high estimates in this longitudinal range. Other studies also point out that the large-scale magnetic field is not measurable towards $l \sim 0°$ and $l \sim 180°$, i.e. the GC and Galactic

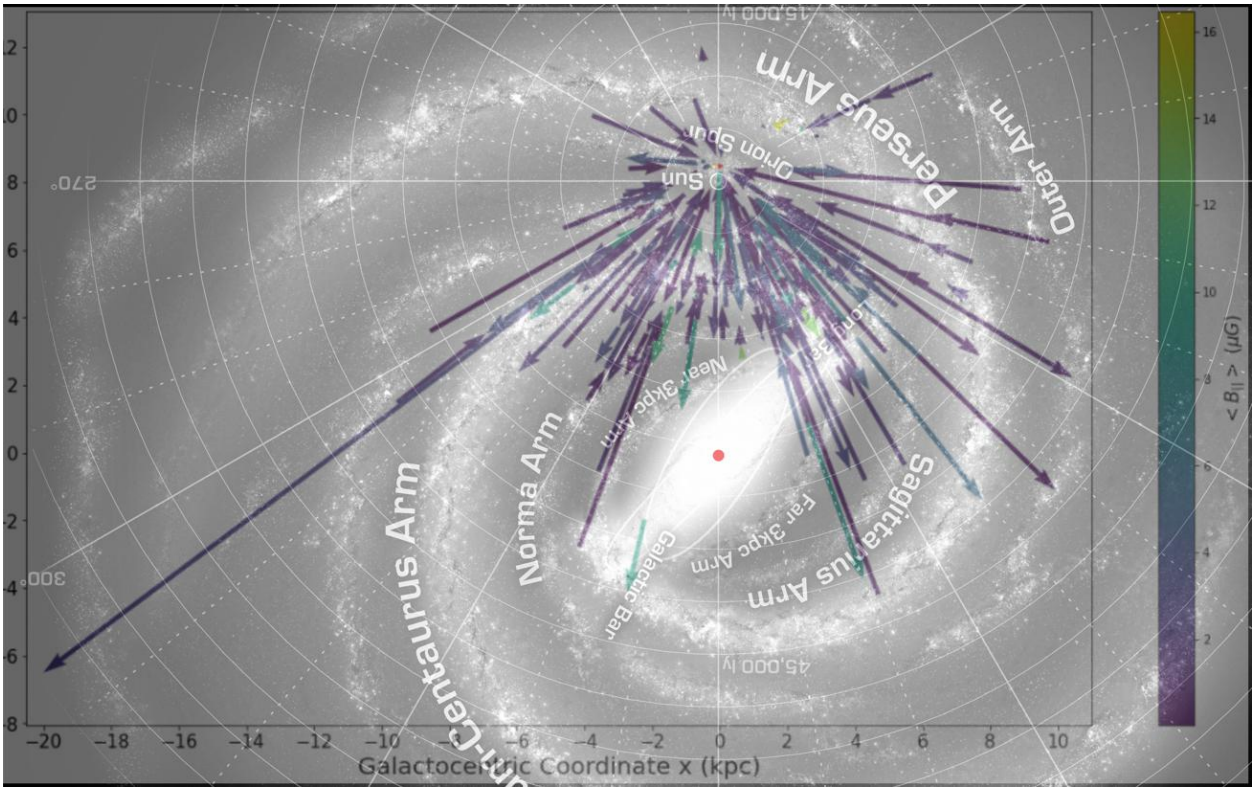

Figure 54: Results for the upper disk region, Method b, overplotted on the modified previously used image of the Galactic structure.

Anticenter respectively, using Faraday rotation due to the same perpendicular arrangement (see e.g., Han et al., 2006). Since the large-scale magnetic field is expected to be oriented perpendicular to the line of sight towards longitudinal ranges in the GC direction, the turbulent component should largely cancel out over long distances, and thus local features of the ISM or individual pulsars dominate the magnetic field measurements, these sight lines may be recommended for the study of the latter features.

The trend of larger $|\langle B_{\parallel} \rangle|$ estimates for smaller distances between subsequent pulsars is observed in the thin disk region, indicating that small-scale features are not evened out on this scale. This may be interpreted as an indication for either the coherence length of the small-scale turbulent field, or the properties of small-scale features with respect to the large-scale electron distribution and magnetic field. High magnetic strength estimates are also obtained in the upper thick disk region for noticeably short sight lines, indicating the presence of small-scale features of the ISM. In the lower disk region, the application of Method b examines the field at a smaller scale and the comparably higher $|\langle B_{\parallel} \rangle|$ estimates are attributed to the crossing of less reversals and the larger influence of local features in the ISM. Regarding orientations, the turbulent field appears to be coherent up to $\approx 1 - 2\,\mathrm{kpc}$ towards the inner Galaxy. This dominance is also seen for the sight lines towards the GC when applying Method c. There, the linear trend procedure is not applicable due to the large-scale field being oriented mainly perpendicular to the respective sight line. Thus, the turbulent field's contribution dominates and results in a 'scattered' RM distribution on scales larger than 100 pc in distance, inhibiting a physically relevant application of a large-scale trend. These sight lines are therefore omitted in section 4 according to the large scattering around the fitted linear trend when applying Method c. The non-feasibly application may be especially seen in the sight lines close to the Solar position for the

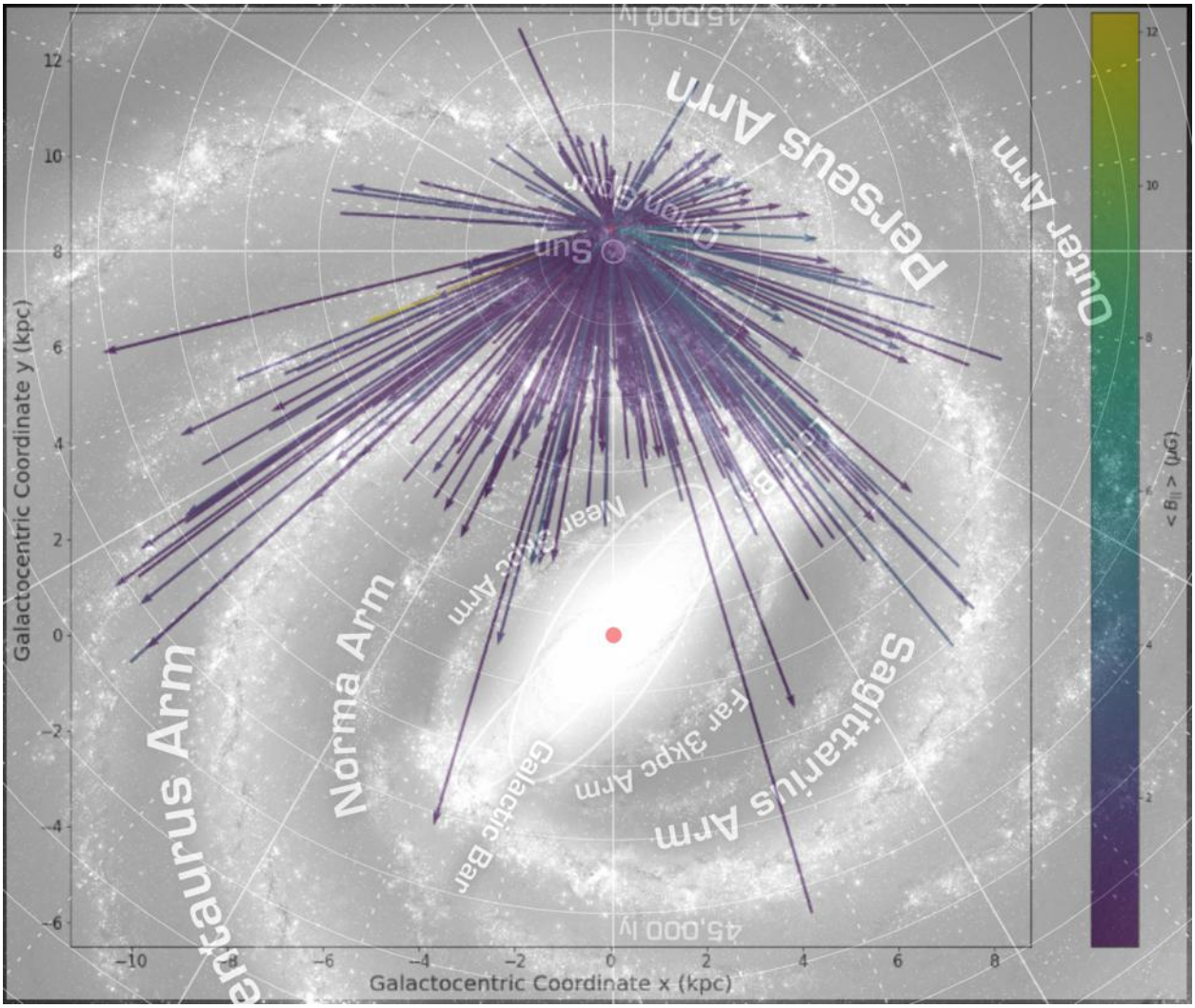

Figure 55: Results with $|\langle B_{\parallel} \rangle|$ estimates for the lower disk region, Method a, overplotted on the modified previously used image of the Galactic structure.

thin disk region with Method c. This observation is in line with the limitation of observations concerning small-scale fluctuations of the electron density and magnetic field variations using pulsars at scales ≤ 1 kpc by Stappers et al. (2011). Furthermore, it supports the findings by Seta and Federrath (2021) that electron density and magnetic field are largely uncorrelated over kpc scales, making the magnetic field estimation valid on Galactic scales but possibly problematic on sub-kpc scales.

One example should be pointed out where the RM measurement and the expected increase in DM with distance along the same sight line should lead to a field orientation directed towards the observer, but the lower DM measurement for the more distant pulsar results in a negative magnetic field estimate, i.e., a field orientation directed away from the observer. The two central sources for this line of sight are at the rather large distance of 6.32 kpc and 8 kpc from the Solar position. As already addressed in section 3, at such large distances, the transverse separation between two sources within the same defined bin can be quite large and may thus lead to different sight lines in terms of electron density within the same bin. A region of larger electron density along the line of sight towards closer sources may thus be absent in the line of sight towards

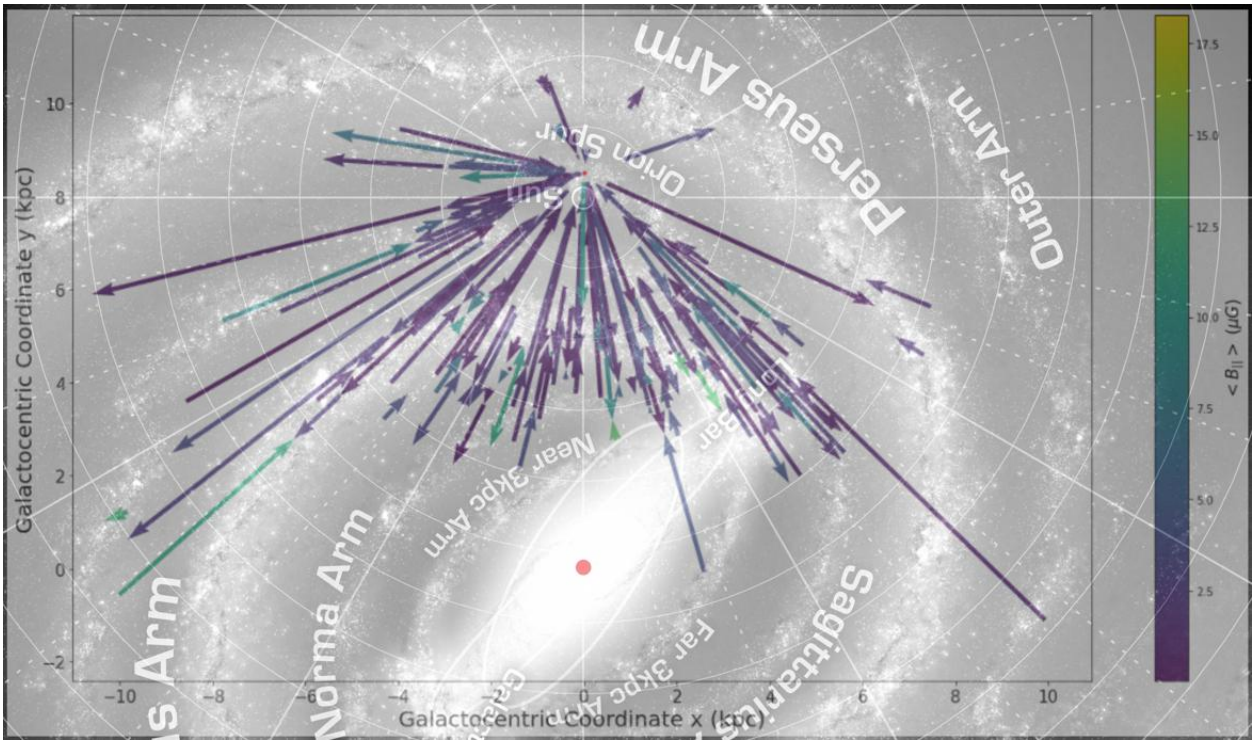

Figure 56: Results for the thin disk region, Method b, overplotted on the modified previously used image of the Galactic structure.

farther sources, resulting in an increased DM for closer sources with respect to farther ones. This case is marked with the 'sign' and 'field configuration' entries in parentheses in the results of applying Method c to the thin disk region (see section 4.1.3).

The relatively larger number of sight lines in the larger magnetic field strength range in the results of Method b compared to Method a, especially in the thin disk region, points to the dominance of local features on small scales, whereas the preferential alignment on 'mid-scales' suggests a 'striated' structure. Furthermore, the upper disk region presents a less anisotropic arrangement for larger $|\langle B_{\parallel}\rangle|$ estimates which indicates the presence of a turbulent random field with a larger influence than HII regions concerning large $|\langle B_{\parallel}\rangle|$ values. Thus, the turbulent field may be assumed to be predominately "weak" rather than "strong". The significant influence of HII regions on the direction of the magnetic field on the mentioned small-scale is a commonly found phenomenon and has a strong influence on observations (see e.g., Mitra et al., 2003; Nota and Katgert, 2010). Compared to the DM, the RM measurements are more sensitive to local features due to their dependence on the possibly correlated electron density and line of sight magnetic field. Therefore, their value is dominated by the densest and most magnetised region which may only provide a minor contribution over the path for the DM value (Katz, 2021). This does not only promote the importance of the small-scale structure of the ISM but also emphasises the requirement of a correct DM estimation to obtain the line of sight magnetic field (Katz, 2021).

Moreover, relatively larger values of the magnetic field strength may be explained by the alignment of the turbulent and large-scale field. For instance, larger values in the upper disk region with Method a show a correlation with the turbulent and the large-scale field. This hypothesis is supported by the fact

that most $|\langle B_{\parallel}\rangle|$ estimates are $\sim 2-3$ times larger than the estimated $|\langle B_{\text{large-scale}}\rangle|$ for these cases. An estimate of this order is backed by the expected value of the average turbulent magnetic field strength of $\langle B_{\text{turbulent}}\rangle \approx 3-5\,\mu\text{G}$ in the solar neighbourhood (Beck and Wielebinski, 2013).

5.3 Occurrence of reversals in the Galactic Magnetic Field

In the third and final question, the occurrence of large-scale reversals or indications for them are discussed. Following from the discussions in the framework of the previous two questions, it is clear that this investigation can only proceed through sight lines of sufficient length along the expected spiral structure to avoid the smaller scale influences. Therefore, Method c with its linear trend procedure functions as the primary source for the analysis.

A considerably long sight line in the interarm region between the Norma and the Scutum-Centaurus arm suggests a counterclockwise direction in this region.
Two other interarm regions between the Far 3 kpc/Scutum-Centaurus and the Sagittarius arm imply a clockwise large-scale magnetic field.
One sight line including almost the whole extension of the Scutum-Centaurus arm indicates a counterclockwise field in this arm. Another sight line at the inner edge of the same arm however suggests a clockwise field. The relatively short length of the latter as well as the considerably large obtained magnetic field value for this sight line imply the influence of a more local feature and strengthen the findings by the first sight line in this region. Several other studies find the same field configuration in this arm and furthermore, it is consistent with the general assumption of counterclockwise fields in the Galactic arms (see e.g., Brown et al., 2007; Noutsos et al., 2008). Together with the findings from the second mentioned interarm region, this indicates a reversal between this arm and the interarm region outer to it. This finding is consistent with other studies (Beck and Wielebinski, 2013).
Especially the three sight lines in the solar neighbourhood indicate the limitation of the method by providing reversed orientations along the almost same sight line over short distances. Two sight lines in this region suggest a counterclockwise orientation of the magnetic field, whereas the third sight line indicates a clockwise field. This supports the findings by Seta and Federrath (2021) that electron density and magnetic field are largely uncorrelated over kpc scales, making the magnetic field estimation valid on Galactic scales but possibly problematic on sub-kpc scales. To be able to make consistent statements concerning the large-scale field, one must choose sight lines of length of the scale of kpc.

6 Conclusions

This work makes use of radio pulsar measurements, notably from the ATNF pulsar catalogue, to gain insight into the magnetic field of our Galaxy, the Milky Way. It thus does not focus on the radio pulsars as objects but rather on the pulses they send into the Interstellar Medium (ISM) and the effect of the latter on their propagation. Especially, the two quantities of the Dispersion Measure (DM) and Rotation Measure (RM) prove to be highly practical tools to obtain the average line of sight magnetic field between the pulsar and the observer. They are both listed in the ATNF catalogue and may thus directly be used. In short, the DM describes the delay of electromagnetic waves through electrostatic interactions with the ISM as a function of the frequency and the present charged particles' masses. It allows for the estimation of either the distance to the pulsar or the electron density along the path to the observer. The other quantity, the RM, is connected to the physical concept of Faraday rotation. Due to this effect, the plane of polarisation of a linearly polarised wave is rotated in the presence of a magnetic field component along the line of sight. The combination of the two measures permits to probe the average magnetic field parallel to the line of sight and thus the study of the Galactic Magnetic Field (GMF). These insights may then feed GMF models with constraints and give validity to the included components and strengths.
To enable the study of the GMF, a fully-automated procedure is developed and implemented in python. This technique is shortly described in the following. The whole approach is focused on extracting physically relevant information on the GMF efficiently from the ATNF catalogue. At the core of this lies the division of the Galaxy into different regions which focuses on the expected Galactic structure. These regions notably include the thin and thick disk. Since the component of the GMF parallel to the line of sight is studied, the regions are subdivided into bins in Galactic longitude and latitude. Advantages as well as disadvantages of this methodology are thoroughly discussed. Following from this, the data is analysed on different length scales, notably with a 'differential' approach, to obtain relevant information on the GMF strength and structure. The obtained results are then comprehensively presented with a focus on the 'disk' regions due to their appropriate geometry and higher availability of sources and sight lines. This presentation is followed by the discussion of the results to come back to the physical context and relevance. Moreover, the findings are interpreted also in connection to other studies in the relevant scientific field.

After briefly recapitulating the content of this work, the three major scientific questions outlined in the motivation for this work are addressed separately hereinafter, limited to the most important conclusions.

How is the Galactic Magnetic Field strength constrained by pulsar measurements?

Pulsars are widely distributed in the Milky Way and thus allow to probe the large-scale GMF. The magnetic field strength of the large-scale field is found to be relatively low with $B \approx 0 - 2\,\mu\mathrm{G}$. However, exceptions to this large-scale trend with significantly stronger magnetic fields are present as well. These can notably be explained by local features of the ISM like HII regions, nebular filaments, or the turbulent ISM component. Despite causing extensively high magnetic field strength estimates, small-scale features appear to not dominate the GMF on large scale. The large-scale GMF likely dominates to up to $|z| \approx 800\,\mathrm{pc}$.

What kind of information about the structure of the Galactic Magnetic Field can be obtained from pulsar measurements?

In terms of structure, the applied methods support a spiral arm configuration of the large-scale GMF. This field is preferably aligned to the Galactic disk. The Bar/Bulge and halo region are expected to differ in field structure from this disk configuration. Moreover, the disk field configuration suggests the study of local features in the direction of the Galactic Centre (GC) region. In this longitudinal range, the large-scale GMF is found to be largely perpendicular to the line of sight, the turbulent component is expected to cancel out for long enough distances and thus only the local contribution remains. The mentioned turbulent component likely dominates on scales $\gtrsim 100\,\mathrm{pc}$ which mostly excludes the possibility of studying the GMF on scales smaller than 1 kpc using pulsars. Finally, the turbulent component's strength is estimated as $\langle B_{\text{turbulent}} \rangle \sim 1 - 2 \cdot \langle B_{\text{large-scale}} \rangle$.

Are field reversals present in the Galactic disk according to observations of pulsar signals?

Indication for reversals in the GMF are found but are largely limited by the sample size. Good evidence is only found for the reversal between the Scutum-Centaurus spiral arm and the interarm region outer to it. The analysis favours counterclockwise orientation of the GMF in the Galactic spiral arms.

7 Future prospects

The content of this section outlines future prospects regarding the study of the GMF with radio emission from pulsars.

Sample size

The knowledge about the Milky Way's magnetic field as detected by the RM as well as the DM has potential for further improvement in the future by means of the following exemplary developments. The increased number of known sources in the Milky Way but also beyond it allows for a better mapping of the magnetic field. For instance, the SKA-MID Band 2 programme at 1.4 GHz is expected to be able to detect around 10,000 RMs for pulsars in the Milky Way for an integration time of one hour per field. In addition, several hundreds of extragalactic pulsars may be detected. Fig. 57 shows the simulated expected distribution of pulsars in the Milky Way (Beck and Wielebinski, 2013).

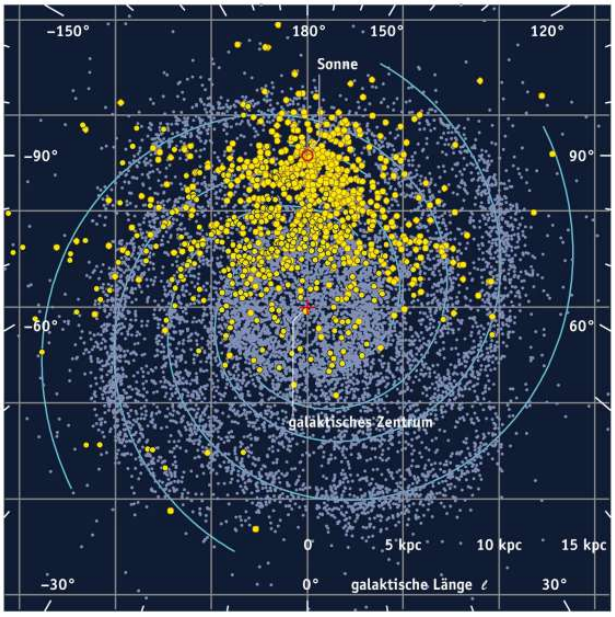

Figure 57: Simulation of pulsars in the Milky Way that can be detected with the SKA (blue), compared to about 2000 pulsars known today (yellow) (from Jim Cordes, Cornell University). Graphics: Sterne und Weltraum (Beck and Wielebinski, 2013).

To show the discrepancy between the used sample and the expected true distribution of pulsars in the Galaxy, both are shown next to each other in Fig. 58. Fig. 58a is taken from Andreasyan et al. (2016) where the authors take an approximate lower limit for the luminosity to which pulsars are detectable in the Galactic plane towards the GC. This limit is then used to estimate the percentage of undetected pulsars by using a luminosity function based on only close pulsars within 1.5 kpc from the Solar position. It may be noted that this leads to the loss of low-luminosity pulsars. Through the Q parameter, they give the average density of pulsars. For Fig. 58b, the distribution of pulsars from the ATNF catalogue is taken and the number of sources within radial annuli from the GC are counted and the final number divided by the area of each annulus to obtain the number of sources per kpc^2. The peaks that can be seen in the 'true' distribution are shifted to one further out annulus in the observed distribution. Furthermore, the local number of pulsars is relatively larger with respect to the other annuli compared to the 'true' distribution. This may be explained by the observational bias that results in an easier observation of nearby sources compared to sources farther away. Thus, the local Q value is likely estimated approximately correctly, whereas the annuli far from the Solar

position are likely underestimated. It should be noted that the number of neutron stars is expected to be significantly higher within each annuli and the classification as a pulsar strongly depends on the orientation of the magnetic axis with respect to the observer's, in this case the Solar or Earth's, position.

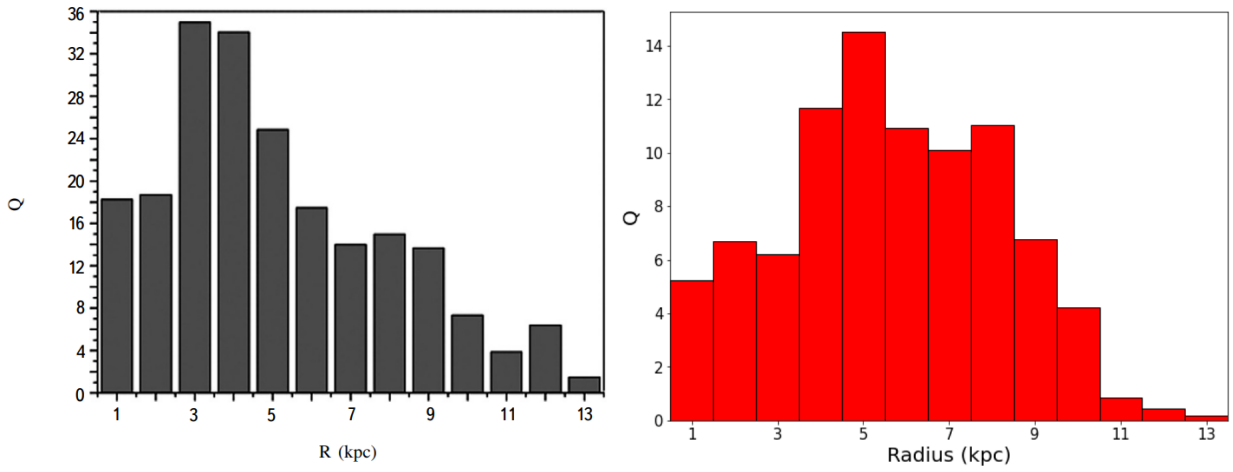

(a) (b)

Figure 58: (a) The true distribution of the density of pulsars (number of pulsars in an area of $1\,\mathrm{kpc}^2$) with respect to distance (the sun is at a distance of $R = 8.5\,\mathrm{kpc}$) (Andreasyan et al., 2016). (b) Same figure for the observed (ATNF catalogue) pulsars.

Pulsar/sight line selection

The used binning technique introduces a strong constraint on the studied sight lines. For instance, a pulsar which is slightly outside one bin but close to another pulsar within the bin is not considered for this sight line, whereas a pulsar that lies at the other longitudinal end of the bin is included in the analysis. Thus, making the used bins or the selection procedure concerning the sight lines more dynamic poses as a promising improvement of the methodology. One possibility is the decrease of longitudinal and latitudinal extension of the bin with distance which decreases the transverse distance between sources within the same bin. Another possibility is the selection of pulsars along the same line of sight according to transverse distance limits between respectively two pulsars or, when considering Method c, arbitrarily more pulsars. These geometric calculations rely on the quality of positional measurements and are thus severely improved by better observational techniques and instruments. An adapted sight line determination procedure may also improve the reliability of halo magnetic field analyses which are out of the scope of this work.

Extragalactic sources

In addition to pulsars in the Milky Way, extragalactic sources pose as widely distributed objects which are not concentrated in the Galactic disk. Observing these sources may provide constraints on the field orientation and strength towards the outer Galaxy. Furthermore, out-of-plane regions of the Milky Way, where pulsar measurements are often either strongly affected by the local environment (see e.g., Abbate et al., 2020) or not available due to the low abundance of sources, can be further studied using these sources. Some exemplary publications that expand the magnetic field study using Faraday rotation may be given as Pshirkov et al. (2011); Van Eck et al. (2011); Mao et al. (2012). The last one focused especially on the halo or out-of-plane

field. To use a similar technique as described in this work, one must use pulsating sources to extract the RM as well as the DM. Furthermore, the local environment of the source may play a significant role and may complicate the use of this method. Alternative techniques as described in section 2.3.1 can also be used to compensate for the limitation to fields parallel to the line of sight when using pulsar measurements.

'Ultra-high' estimates

Along several sight lines, as 'ultra-high' dubbed magnetic field strength estimates are found. In Appendix B, a list with the corresponding pulsars, magnetic field strength estimates, and available publications is provided. These sources may pose as subjects of further studies regarding the objects themselves or their environment. Notably, one may make use of the HII region catalogue by Anderson et al. (2014).

Radial trend of the magnetic field strength

Finally, results from using especially Method b and c may be utilised to estimate the radial trend of the magnetic field strength in the Galaxy. These two methods allow for the analysis of the magnetic field strength separated from the solar neighbourhood. Thus, a sight line that lies in either an arm or an interarm region while having sufficient length may be selected and used to estimate the large-scale magnetic field strength at its radial distance from the GC. To do so, one may have to apply an angular correction to the obtained value depending on the sight line's orientation with respect to the assumed large-scale magnetic field structure. In case a large enough number and especially spatial distribution of sufficiently long sight lines is available, this can potentially provide an estimate of the large-scale magnetic field strength with Galactocentric distance. It should be emphasised that especially the outer regions of the Galaxy require a larger number of measured pulsars than currently available.

References

Federico Abbate, Andrea Possenti, Caterina Tiburzi, Ewan Barr, Willem van Straten, Alessandro Ridolfi, and Paulo Freire. Constraints on the magnetic field in the galactic halo from globular cluster pulsars. *Nature Astronomy*, 4:704–710, 2020. ISSN 2397-3366. doi: 10.1038/s41550-020-1030-6. URL `https://doi.org/10.1038/s41550-020-1030-6`.

L. D. Anderson, T. M. Bania, Dana S. Balser, V. Cunningham, T. V. Wenger, B. M. Johnstone, and W. P. Armentrout. The WISE Catalog of Galactic H II Regions. *The Astrophysical Journal Supplement Series*, 212(1):1, May 2014. doi: 10.1088/0067-0049/212/1/1.

H. A. Andreasyan, R. R. Andreasyan, and G. M. Paronyan. Distribution of Pulsars in the Galaxy. *Astrophysics*, 59(1):57–67, March 2016. doi: 10.1007/s10511-016-9416-y.

T. G. Arshakian, R. Beck, Marita Krause, and D. Sokoloff. Evolution of magnetic fields in galaxies and future observational tests with the Square Kilometre Array. *Astronomy & Astrophysics*, 494(1):21–32, January 2009. doi: 10.1051/0004-6361:200810964.

R. Beck. Galactic magnetic fields. *Scholarpedia*, 2(8):2411, 2007. doi: 10.4249/scholarpedia.2411. revision #193987.

Rainer Beck. Galactic and Extragalactic Magnetic Fields. *Space Science Reviews*, 99:243–260, October 2001. doi: 10.1023/A:1013805401252.

Rainer Beck and Richard Wielebinski. Magnetic Fields in Galaxies. In Terry D. Oswalt and Gerard Gilmore, editors, *Planets, Stars and Stellar Systems. Volume 5: Galactic Structure and Stellar Populations*, volume 5, pages 641–723. Springer, Dordrecht, 2013. doi: 10.1007/978-94-007-5612-0_13.

Rainer Beck, Axel Brandenburg, David Moss, Anvar Shukurov, and Dmitry Sokoloff. Galactic Magnetism: Recent Developments and Perspectives. *Annual Review of Astronomy and Astrophysics*, 34:155–206, January 1996. doi: 10.1146/annurev.astro.34.1.155.

Leszek P. Błaszkiewicz, Paweł Flisek, Kacper Kotulak, Andrzej Krankowski, Wojciech Lewandowski, Jarosław Kijak, and Adam Froń. Finding the Ionospheric Fluctuations Reflection in the Pulsar Signals' Characteristics Observed with LOFAR. *Sensors*, 21(1):51, December 2020. doi: 10.3390/s21010051.

François Boulanger, Torsten Enßlin, Andrew Fletcher, Philipp Girichides, Stefan Hackstein, Marijke Haverkorn, Jörg R. Hörandel, Tess Jaffe, Jens Jasche, Michael Kachelrieß, Kumiko Kotera, Christoph Pfrommer, Jörg P. Rachen, Luiz F. S. Rodrigues, Beatriz Ruiz-Granados, Amit Seta, Anvar Shukurov, Günter Sigl, Theo Steininger, Valentina Vacca, Ellert van der Velden, Arjen van Vliet, and Jiaxin Wang. IMAGINE: a comprehensive view of the interstellar medium, Galactic magnetic fields and cosmic rays. *Journal of Cosmology and Astroparticle Physics*, 2018(8):049, August 2018. doi: 10.1088/1475-7516/2018/08/049.

Jo Bovy, Hans-Walter Rix, and David W. Hogg. The Milky Way Has No Distinct Thick Disk. *The Astrophysical Journal*, 751(2):131, June 2012. doi: 10.1088/0004-637X/751/2/131.

Hale Bradt. *Astrophysics Processes*. Cambridge University Press, 2008. ISBN 9780511451188. URL `https://www.ebook.de/de/product/15255214/hale_bradt_astrophysics_processes.html`.

Casey Brinkman, Paulo C. C. Freire, Joanna Rankin, and Kevin Stovall. No pulsar left behind - I. Timing, pulse-sequence polarimetry and emission morphology for 12 pulsars. *Monthly Notices of the Royal Astronomical Society*, 474(2):2012–2027, February 2018. doi: 10.1093/mnras/stx2842.

J. C. Brown, M. Haverkorn, B. M. Gaensler, A. R. Taylor, N. S. Bizunok, N. M. McClure-Griffiths, J. M. Dickey, and A. J. Green. Rotation Measures of Extragalactic Sources behind the Southern Galactic Plane: New Insights into the Large-Scale Magnetic Field of the Inner Milky Way. *The Astrophysical Journal*, 663 (1):258–266, July 2007. doi: 10.1086/518499.

Bernard F. Burke, Francis Graham-Smith, and Peter N. Wilkinson. *An Introduction to Radio Astronomy*. Cambridge University Press, 4 edition, 2019. doi: 10.1017/9781316987506.

L. F. Burlaga and N. F. Ness. Observations of the Interstellar Magnetic Field in the Outer Heliosheath: Voyager 1. *The Astrophysical Journal*, 829(2):134, October 2016. doi: 10.3847/0004-637X/829/2/134.

F. Camilo, S. M. Ransom, S. Chatterjee, S. Johnston, and P. Demorest. PSR J1841-0500: A Radio Pulsar That Mostly is Not There. *The Astrophysical Journal*, 746(1):63, February 2012. doi: 10.1088/0004-637X/746/1/63.

P. M. Chadwick, K. Lyons, T. J. L. McComb, K. J. Orford, J. L. Osborne, S. M. Rayner, S. E. Shaw, and K. E. Turver. Very High Energy Gamma Rays from Young Pulsars and Supernova Remnants in the Southern Hemisphere. *The Astrophysical Journal*, 537(1):414–421, July 2000. doi: 10.1086/309014.

CHIME/FRB Collaboration, Mandana Amiri, Bridget C. Andersen, Kevin Bandura, Sabrina Berger, Mohit Bhardwaj, Michelle M. Boyce, P. J. Boyle, Charanjot Brar, Daniela Breitman, Tomas Cassanelli, Pragya Chawla, Tianyue Chen, J. F. Cliche, Amanda Cook, Davor Cubranic, Alice P. Curtin, Meiling Deng, Matt Dobbs, Fengqiu Adam Dong, Gwendolyn Eadie, Mateus Fandino, Emmanuel Fonseca, B. M. Gaensler, Utkarsh Giri, Deborah C. Good, Mark Halpern, Alex S. Hill, Gary Hinshaw, Alexander Josephy, Jane F. Kaczmarek, Zarif Kader, Joseph W. Kania, Victoria M. Kaspi, T. L. Landecker, Dustin Lang, Calvin Leung, Dongzi Li, Hsiu-Hsien Lin, Kiyoshi W. Masui, Ryan McKinven, Juan Mena-Parra, Marcus Merryfield, Bradley W. Meyers, Daniele Michilli, Nikola Milutinovic, Arash Mirhosseini, Moritz Münchmeyer, Arun Naidu, Laura Newburgh, Cherry Ng, Chitrang Patel, Ue-Li Pen, Emily Petroff, Tristan Pinsonneault-Marotte, Ziggy Pleunis, Masoud Rafiei-Ravandi, Mubdi Rahman, Scott M. Ransom, Andre Renard, Pranav Sanghavi, Paul Scholz, J. Richard Shaw, Kaitlyn Shin, Seth R. Siegel, Andrew E. Sikora, Saurabh Singh, Kendrick M. Smith, Ingrid Stairs, Chia Min Tan, S. P. Tendulkar, Keith Vanderlinde, Haochen Wang, Dallas Wulf, and A. V. Zwaniga. The First CHIME/FRB Fast Radio Burst Catalog. *The Astrophysical Journal Supplement Series*, 257(2):59, December 2021. doi: 10.3847/1538-4365/ac33ab.

David H. Clark and Francis Richard Stephenson. *The historical supernovae*. Pergamon Press, 1977. ISBN 0-08-020914-9.

Dan P. Clemens, A. F. Pinnick, M. D. Pavel, and B. W. Taylor. The Galactic Plane Infrared Polarization Survey (GPIPS). *The Astrophysical Journal Supplement Series*, 200(2):19, June 2012. doi: 10.1088/0067-0049/200/2/19.

J. M. Cordes and T. J. W. Lazio. NE2001.I. A New Model for the Galactic Distribution of Free Electrons and its Fluctuations. *arXiv e-prints*, art. astro-ph/0207156, July 2002.

J. M. Cordes and T. J. W. Lazio. NE2001. II. Using Radio Propagation Data to Construct a Model for the Galactic Distribution of Free Electrons. *arXiv e-prints*, art. astro-ph/0301598, January 2003.

J. M. Cordes, J. M. Weisberg, D. A. Frail, S. R. Spangler, and M. Ryan. The galactic distribution of free electrons. *Nature*, 354(6349):121–124, November 1991. doi: 10.1038/354121a0.

Roland M. Crocker, David I. Jones, Fulvio Melia, Jürgen Ott, and Raymond J. Protheroe. A lower limit of 50 microgauss for the magnetic field near the Galactic Centre. *Nature*, 463(7277):65–67, January 2010. doi: 10.1038/nature08635.

Michaël De Becker. Lecture notes in interstellar medium, 2021a.

Michaël De Becker. Lecture notes in radio astrophysics, 2021b.

G. Desvignes, R. P. Eatough, U. L. Pen, K. J. Lee, S. A. Mao, R. Karuppusamy, D. H. F. M. Schnitzeler, H. Falcke, M. Kramer, O. Wucknitz, L. G. Spitler, P. Torne, K. Liu, G. C. Bower, I. Cognard, A. G. Lyne, and B. W. Stappers. Large Magneto-ionic Variations toward the Galactic Center Magnetar, PSR J1745-2900. *Astrophysical Journal Letters*, 852(1):L12, January 2018. doi: 10.3847/2041-8213/aaa2f8.

Paul B. Eskridge, Jay A. Frogel, Richard W. Pogge, Alice C. Quillen, Roger L. Davies, D. L. DePoy, Mark L. Houdashelt, Leslie E. Kuchinski, Solange V. Ramírez, K. Sellgren, Donald M. Terndrup, and Glenn P. Tiede. The Frequency of Barred Spiral Galaxies in the Near-Infrared. *The Astronomical Journal*, 119(2): 536–544, February 2000. doi: 10.1086/301203.

Michael Faraday. Experimental researches in electricity. nineteenth series. *Philosophical Transactions of the Royal Society of London*, 136:1–20, 1846. ISSN 02610523. URL `http://www.jstor.org/stable/108303`.

K. Ferrière. Interstellar magnetic fields in the Galactic center region. *Astronomy & Astrophysics*, 505(3): 1183–1198, October 2009. doi: 10.1051/0004-6361/200912617.

Richard P. Feynman, Robert B. Leighton, and Matthew Sands. *Strahlung und Wärme*. De Gruyter (O), 2015. ISBN 9783110437775. doi: doi:10.1515/9783110437775. URL `https://doi.org/10.1515/9783110437775`.

Francesca Figueras Siñol. Lecture notes in galactic astronomy, 2021.

P. C. Frisch, B. G. Andersson, A. Berdyugin, V. Piirola, R. DeMajistre, H. O. Funsten, A. M. Magalhaes, D. B. Seriacopi, D. J. McComas, N. A. Schwadron, J. D. Slavin, and S. J. Wiktorowicz. The Interstellar Magnetic Field Close to the Sun. II. *The Astrophysical Journal*, 760(2):106, December 2012. doi: 10.1088/0004-637X/760/2/106.

Klaus Fuhrmann. Nearby stars of the Galactic disc and halo - V. *Monthly Notices of the Royal Astronomical Society*, 414(4):2893–2922, July 2011. doi: 10.1111/j.1365-2966.2011.18476.x.

D. A. Green and F. R. Stephenson. Historical Supernovae. In K. Weiler, editor, *Supernovae and Gamma-Ray Bursters*, volume 598, pages 7–19. 2003. doi: 10.1007/3-540-45863-8_2.

Renaud Gueroult, Yuan Shi, Jean-Marcel Rax, and Nathaniel J. Fisch. Determining the rotation direction in pulsars. *Nature Communications*, 10:3232, July 2019. doi: 10.1038/s41467-019-11243-4.

J. L. Han, R. N. Manchester, A. G. Lyne, G. J. Qiao, and W. van Straten. Pulsar Rotation Measures and the Large-Scale Structure of the Galactic Magnetic Field. *The Astrophysical Journal*, 642(2):868–881, May 2006. doi: 10.1086/501444.

J. L. Han, R. N. Manchester, W. van Straten, and P. Demorest. Pulsar Rotation Measures and Large-scale Magnetic Field Reversals in the Galactic Disk. *The Astrophysical Journal Supplement Series*, 234(1):11, January 2018. doi: 10.3847/1538-4365/aa9c45.

JinLin Han. Pulsars as excellent probes for the magnetic structure in our Milky Way. In Joeri van Leeuwen, editor, *Neutron Stars and Pulsars: Challenges and Opportunities after 80 years*, volume 291, pages 223–228, March 2013. doi: 10.1017/S174392131202371X.

J.L. Han. Observing interstellar and intergalactic magnetic fields. *Annual Review of Astronomy and Astrophysics*, 55(1):111–157, 2017. doi: 10.1146/annurev-astro-091916-055221. URL `https://doi.org/10.1146/annurev-astro-091916-055221`.

M. Haverkorn, J. C. Brown, B. M. Gaensler, and N. M. McClure-Griffiths. The Outer Scale of Turbulence in the Magnetoionized Galactic Interstellar Medium. *The Astrophysical Journal*, 680(1):362–370, June 2008. doi: 10.1086/587165.

Carl Heiles. The Local Direction and Curvature of the Galactic Magnetic Field Derived from Starlight Polarization. *The Astrophysical Journal*, 462:316, May 1996. doi: 10.1086/177153.

Amina Helmi. The stellar halo of the Galaxy. *The Astronomy and Astrophysics Review*, 15(3):145–188, June 2008. doi: 10.1007/s00159-008-0009-6.

Amina Helmi. Streams, Substructures, and the Early History of the Milky Way. *Annual Review of Astronomy and Astrophysics*, 58:205–256, August 2020. doi: 10.1146/annurev-astro-032620-021917.

A. Hewish, S.J. Bell, J.D.H. Pilkington, P.F. Scott, and R.A. Collins. Observation of a rapidly pulsating radio source. *Nature*, 217:709–713, 1968. doi: 10.1038/217709a0.

S. Hutschenreuter, C. S. Anderson, S. Betti, G. C. Bower, J. A. Brown, M. Brüggen, E. Carretti, T. Clarke, A. Clegg, A. Costa, S. Croft, C. V. Eck, B. M. Gaensler, F. de Gasperin, M. Haverkorn, G. Heald, C. L. H. Hull, M. Inoue, M. Johnston-Hollitt, J. Kaczmarek, C. Law, Y. K. Ma, D. MacMahon, S. A. Mao, C. Riseley, S. Roy, R. Shanahan, T. Shimwell, J. Stil, C. Sobey, S. P. O'Sullivan, C. Tasse, V. Vacca, T. Vernstrom, P. K. G. Williams, M. Wright, and T. A. Enßlin. The Galactic Faraday rotation sky 2020. *Astronomy & Astrophysics*, 657:A43, January 2022. doi: 10.1051/0004-6361/202140486.

T. R. Jaffe, J. P. Leahy, A. J. Banday, S. M. Leach, S. R. Lowe, and A. Wilkinson. Modelling the Galactic magnetic field on the plane in two dimensions. *Monthly Notices of the Royal Astronomical Society*, 401(2): 1013–1028, January 2010. doi: 10.1111/j.1365-2966.2009.15745.x.

T. R. Jaffe, K. M. Ferrière, A. J. Banday, A. W. Strong, E. Orlando, J. F. Macías-Pérez, L. Fauvet, C. Combet, and E. Falgarone. Comparing polarized synchrotron and thermal dust emission in the Galactic plane. *Monthly Notices of the Royal Astronomical Society*, 431(1):683–694, May 2013. doi: 10.1093/mnras/stt200.

Tess R. Jaffe. Practical Modeling of Large-Scale Galactic Magnetic Fields: Status and Prospects. *Galaxies*, 7 (2):52, April 2019. doi: 10.3390/galaxies7020052.

Ronnie Jansson and Glennys R. Farrar. A New Model of the Galactic Magnetic Field. *The Astrophysical Journal*, 757(1):14, September 2012a. doi: 10.1088/0004-637X/757/1/14.

Ronnie Jansson and Glennys R. Farrar. The Galactic Magnetic Field. *Astrophysical Journal Letters*, 761(1): L11, December 2012b. doi: 10.1088/2041-8205/761/1/L11.

Ronnie Jansson, Glennys R. Farrar, Andre H. Waelkens, and Torsten A. Enßlin. Constraining models of the large scale Galactic magnetic field with WMAP5 polarization data and extragalactic rotation measure sources. *Journal of Cosmology and Astroparticle Physics*, 2009(7):021, July 2009. doi: 10.1088/1475-7516/2009/07/021.

Simon Johnston, C. Sobey, S. Dai, M. Keith, M. Kerr, R. N. Manchester, L. S. Oswald, A. Parthasarathy, R. M. Shannon, and P. Weltevrede. Two years of pulsar observations with the ultra-wide-band receiver on the Parkes radio telescope. *Monthly Notices of the Royal Astronomical Society*, 502(1):1253–1262, March 2021. doi: 10.1093/mnras/stab095.

M. Kachelrieß, P. D. Serpico, and M. Teshima. The Galactic magnetic field as spectrograph for ultra-high energy cosmic rays. *Astroparticle Physics*, 26(6):378–386, January 2007. doi: 10.1016/j.astropartphys.2006.08.004.

A. Karastergiou, A. von Hoensbroech, M. Kramer, D. R. Lorimer, A. G. Lyne, O. Doroshenko, A. Jessner, C. Jordan, and R. Wielebinski. Simultaneous single-pulse observations of radio pulsars. I. The polarization characteristics of PSR B0329+54. *Astronomy & Astrophysics*, 379:270–278, November 2001. doi: 10.1051/0004-6361:20011306.

Victoria M. Kaspi and Michael Kramer. Radio Pulsars: The Neutron Star Population & Fundamental Physics. *arXiv e-prints*, art. arXiv:1602.07738, February 2016.

J. I. Katz. The environment of FRB 121102 and possible relation to SGR/PSR J1745-2900. *Monthly Notices of the Royal Astronomical Society*, 501(1):L76–L79, February 2021. doi: 10.1093/mnrasl/slaa202.

M. J. Keith, S. Johnston, M. Kramer, P. Weltevrede, K. P. Watters, and B. W. Stappers. A high-frequency search for radio pulsars in three EGRET error boxes. *Monthly Notices of the Royal Astronomical Society*, 389(4):1881–1884, October 2008. doi: 10.1111/j.1365-2966.2008.13711.x.

M. Kerr, W. A. Coles, C. A. Ward, S. Johnston, A. V. Tuntsov, and R. M. Shannon. Extreme scattering events towards two young pulsars. *Monthly Notices of the Royal Astronomical Society*, 474(4):4637–4647, March 2018. doi: 10.1093/mnras/stx3101.

Ulrich Klein and Andrew Fletcher. *Galactic and Intergalactic Magnetic Fields*. Springer International Publishing, 1 edition, 2015. ISBN 978-3-319-08941-6. doi: 10.1007/978-3-319-08942-3.

Noel Klingler, Oleg Kargaltsev, George G. Pavlov, C. Y. Ng, Zhengyangguang Gong, and Jeremy Hare. "The Goose" Pulsar Wind Nebula of PSR J1016-5857: The Birth of a Plerion. *arXiv e-prints*, art. arXiv:2204.13167, April 2022.

Marita Krause. Large-scale magnetic field in spiral galaxies. *Memorie della Società Astronomica Italiana*, 78: 314, January 2007.

S. R. Kulkarni. Dispersion measure: Confusion, Constants & Clarity. *arXiv e-prints*, art. arXiv:2007.02886, July 2020.

D. R. Lorimer, M. Kramer, P. Müller, N. Wex, A. Jessner, C. Lange, and R. Wielebinski. A 1400-MHz pilot search for young pulsars. *Astronomy & Astrophysics*, 358:169–176, June 2000.

D. R. Lorimer, M. Bailes, M. A. McLaughlin, D. J. Narkevic, and F. Crawford. A Bright Millisecond Radio Burst of Extragalactic Origin. *Science*, 318(5851):777, November 2007. doi: 10.1126/science.1147532.

A. G. Lyne and F. Graham Smith. Pulsar rotation measures and the galactic magnetic field. *Monthly Notices of the Royal Astronomical Society*, 237:533–541, March 1989. doi: 10.1093/mnras/237.3.533.

A. G. Lyne, R. N. Manchester, and J. H. Taylor. The galactic population of pulsars. *Monthly Notices of the Royal Astronomical Society*, 213:613–639, April 1985. doi: 10.1093/mnras/213.3.613.

Y. K. Ma, S. A. Mao, A. Ordog, and J. C. Brown. The complex large-scale magnetic fields in the first Galactic quadrant as revealed by the Faraday depth profile disparity. *Monthly Notices of the Royal Astronomical Society*, 497(3):3097–3117, September 2020. doi: 10.1093/mnras/staa2105.

G. Mall, R. A. Main, J. Antoniadis, C. G. Bassa, M. Burgay, S. Chen, I. Cognard, R. Concu, A. Corongiu, M. Gaikwad, H. Hu, G. H. Janssen, R. Karuppusamy, M. Kramer, K. J. Lee, K. Liu, J. W. McKee, A. Melis, M. B. Mickaliger, D. Perrodin, M. Pilia, A. Possenti, D. J. Reardon, S. A. Sanidas, T. Sprenger, B. W. Stappers, L. Wang, O. Wucknitz, and W. W. Zhu. Modelling annual scintillation arc variations in PSR J1643-1224 using the Large European Array for Pulsars. *Monthly Notices of the Royal Astronomical Society*, 511(1):1104–1114, March 2022. doi: 10.1093/mnras/stac096.

R. N. Manchester. Pulsar Rotation and Dispersion Measures and the Galactic Magnetic Field. *The Astrophysical Journal*, 172:43, February 1972. doi: 10.1086/151326.

R. N. Manchester. Structure of the Local Galactic Magnetic Field. *The Astrophysical Journal*, 188:637–644, March 1974. doi: 10.1086/152757.

R. N. Manchester. Observational Properties of Pulsars. *Science*, 304(5670):542–547, April 2004. doi: 10.1126/science.1097649.

R. N. Manchester and J. H. Taylor. Observed and derived parameters for 330 pulsars. *The Astronomical Journal*, 86:1953–1973, December 1981. doi: 10.1086/113078.

R. N. Manchester, G. B. Hobbs, A. Teoh, and M. Hobbs. The Australia Telescope National Facility Pulsar Catalogue. *The Astronomical Journal*, 129(4):1993–2006, April 2005. doi: 10.1086/428488. URL `http://www.atnf.csiro.au/research/pulsar/psrcat`.

S. A. Mao, N. M. McClure-Griffiths, B. M. Gaensler, J. C. Brown, C. L. van Eck, M. Haverkorn, P. P. Kronberg, J. M. Stil, A. Shukurov, and A. R. Taylor. New Constraints on the Galactic Halo Magnetic Field Using Rotation Measures of Extragalactic Sources toward the Outer Galaxy. *The Astrophysical Journal*, 755(1):21, August 2012. doi: 10.1088/0004-637X/755/1/21.

H. Men, K. Ferrière, and J. L. Han. Observational constraints on models for the interstellar magnetic field in the Galactic disk. *Astronomy & Astrophysics*, 486(3):819–828, August 2008. doi: 10.1051/0004-6361:20078683.

D. Mitra, R. Wielebinski, M. Kramer, and A. Jessner. The effect of HII regions on rotation measure of pulsars. *Astronomy & Astrophysics*, 398:993–1005, February 2003. doi: 10.1051/0004-6361:20021702.

D. Moss, R. Stepanov, T. G. Arshakian, R. Beck, M. Krause, and D. Sokoloff. Multiscale magnetic fields in spiral galaxies: evolution and reversals. *Astronomy & Astrophysics*, 537:A68, January 2012. doi: 10.1051/0004-6361/201118122.

Nobel Prize Outreach AB 2022. The Nobel Prize in Physics 1974. URL `https://www.nobelprize.org/prizes/physics/1974/summary/`. (visited on 20/05/2022).

T. Nota and P. Katgert. The large-scale magnetic field in the fourth Galactic quadrant. *Astronomy & Astrophysics*, 513:A65, April 2010. doi: 10.1051/0004-6361/200911803.

A. Noutsos, S. Johnston, M. Kramer, and A. Karastergiou. New pulsar rotation measures and the Galactic magnetic field. *Monthly Notices of the Royal Astronomical Society*, 386(4):1881–1896, June 2008. doi: 10.1111/j.1365-2966.2008.13188.x.

Aristeidis Noutsos. The magnetic field of the milky way from faraday rotation of pulsars and extragalactic sources. *Space Science Reviews*, 166(1):307–324, 2012. ISSN 1572-9672. URL `https://doi.org/10.1007/s11214-011-9860-2`.

Lucy Oswald, Aris Karastergiou, and Simon Johnston. Pulsar polarimetry with the Parkes ultra-wideband receiver. *Monthly Notices of the Royal Astronomical Society*, 496(2):1418–1429, August 2020. doi: 10.1093/mnras/staa1597.

Matteo Pais, Christoph Pfrommer, Kristian Ehlert, Maria Werhahn, and Georg Winner. Constraining the coherence scale of the interstellar magnetic field using TeV gamma-ray observations of supernova remnants. *Monthly Notices of the Royal Astronomical Society*, 496(2):2448–2461, August 2020. doi: 10.1093/mnras/staa1678.

T. Passot and E. Vázquez-Semadeni. The correlation between magnetic pressure and density in compressible MHD turbulence. *Astronomy & Astrophysics*, 398:845–855, February 2003. doi: 10.1051/0004-6361:20021665.

E. Petroff, J. W. T. Hessels, and D. R. Lorimer. Fast radio bursts at the dawn of the 2020s. *The Astronomy and Astrophysics Review*, 30(1):2, December 2022. doi: 10.1007/s00159-022-00139-w.

Planck Collaboration, R. Adam, P. A. R. Ade, N. Aghanim, Y. Akrami, M. I. R. Alves, F. Argüeso, M. Arnaud, F. Arroja, M. Ashdown, and et al. Planck 2015 results. I. Overview of products and scientific results. *Astronomy & Astrophysics*, 594:A1, September 2016. doi: 10.1051/0004-6361/201527101.

P. Predehl, R. A. Sunyaev, W. Becker, H. Brunner, R. Burenin, A. Bykov, A. Cherepashchuk, N. Chugai, E. Churazov, V. Doroshenko, N. Eismont, M. Freyberg, M. Gilfanov, F. Haberl, I. Khabibullin, R. Krivonos, C. Maitra, P. Medvedev, A. Merloni, K. Nandra, V. Nazarov, M. Pavlinsky, G. Ponti, J. S. Sanders, M. Sasaki, S. Sazonov, A. W. Strong, and J. Wilms. Detection of large-scale X-ray bubbles in the Milky Way halo. *Nature*, 588(7837):227–231, December 2020. doi: 10.1038/s41586-020-2979-0.

M. S. Pshirkov, P. G. Tinyakov, P. P. Kronberg, and K. J. Newton-McGee. Deriving the Global Structure of the Galactic Magnetic Field from Faraday Rotation Measures of Extragalactic Sources. *The Astrophysical Journal*, 738(2):192, September 2011. doi: 10.1088/0004-637X/738/2/192.

V. Radhakrishnan and D. J. Cooke. Magnetic Poles and the Polarization Structure of Pulsar Radiation. *Astrophysical Letters*, 3:225, January 1969.

R. J. Rand and A. G. Lyne. New Rotation Measures of Distant Pulsars in the Inner Galaxy and Magnetic Field Reversals. *Monthly Notices of the Royal Astronomical Society*, 268:497, May 1994. doi: 10.1093/mnras/268.2.497.

M. J. Reid, K. M. Menten, A. Brunthaler, X. W. Zheng, T. M. Dame, Y. Xu, J. Li, N. Sakai, Y. Wu, K. Immer, B. Zhang, A. Sanna, L. Moscadelli, K. L. J. Rygl, A. Bartkiewicz, B. Hu, L. H. Quiroga-Nuñez, and H. J. van Langevelde. Trigonometric Parallaxes of High-mass Star-forming Regions: Our View of the Milky Way. *The Astrophysical Journal*, 885(2):131, November 2019. doi: 10.3847/1538-4357/ab4a11.

S. M. Ressler, E. Quataert, and J. M. Stone. Accretion of magnetized stellar winds in the Galactic centre: implications for Sgr A* and PSR J1745-2900. *Monthly Notices of the Royal Astronomical Society*, 482(1): L123–L128, January 2019. doi: 10.1093/mnrasl/sly201.

Marc Ribó. Lecture notes in high energy astrophysics, 2021.

R. Michael Rich. *The Galactic Bulge*, pages 271–346. Springer Netherlands, Dordrecht, 2013. ISBN 978-94-007-5612-0. doi: 10.1007/978-94-007-5612-0_6. URL `https://doi.org/10.1007/978-94-007-5612-0_6`.

A. C. Robin, C. Reylé, S. Derrière, and S. Picaud. A synthetic view on structure and evolution of the Milky Way. *Astronomy & Astrophysics*, 409:523–540, October 2003. doi: 10.1051/0004-6361:20031117.

Keith Robinson. *Spectroscopy: The Key to the Stars*. Springer, New York, NY, 1 edition, 2007. ISBN 978-0-387-68288-4. doi: 10.1007/978-0-387-68288-4.

S. Roy, A. Pramesh Rao, and R. Subrahmanyan. Magnetic field near the central region of the Galaxy: rotation measure of extragalactic sources. *Astronomy & Astrophysics*, 478(2):435–442, February 2008. doi: 10.1051/0004-6361:20066470.

George B. Rybicki and Alan P. Lightman. *Radiative processes in astrophysics*. John Wiley & Sons, Ltd, 1979.

D. H. F. M. Schnitzeler. The latitude dependence of the rotation measures of NVSS sources. *Monthly Notices of the Royal Astronomical Society*, 409(1):L99–L103, November 2010. doi: 10.1111/j.1745-3933.2010.00957.x.

D. H. F. M. Schnitzeler, R. P. Eatough, K. Ferrière, M. Kramer, K. J. Lee, A. Noutsos, and R. M. Shannon. Radio polarimetry of Galactic Centre pulsars. *Monthly Notices of the Royal Astronomical Society*, 459(3): 3005–3011, July 2016. doi: 10.1093/mnras/stw841.

Amit Seta and Christoph Federrath. Magnetic fields in the milky way from pulsar observations: effect of the correlation between thermal electrons and magnetic fields. *Monthly Notices of the Royal Astronomical Society*, 502(2):2220–2237, 01 2021. ISSN 1365-2966. doi: 10.1093/mnras/stab128. URL `http://dx.doi.org/10.1093/mnras/stab128`.

R. Shanahan, S. J. Lemmer, J. M. Stil, H. Beuther, Y. Wang, J. Soler, L. D. Anderson, F. Bigiel, S. C. O. Glover, P. Goldsmith, R. S. Klessen, N. M. McClure-Griffiths, S. Reissl, M. Rugel, and R. J. Smith. Strong Excess Faraday Rotation on the Inside of the Sagittarius Spiral Arm. *Astrophysical Journal Letters*, 887 (1):L7, December 2019. doi: 10.3847/2041-8213/ab58d4.

Egid Sicheneder and Jason Dexter. A single H II region model of the strong interstellar scattering towards Sgr A*. *Monthly Notices of the Royal Astronomical Society*, 467(3):3642–3647, May 2017. doi: 10.1093/mnras/stx103.

C Sobey, A V Bilous, J-M Grießmeier, J W T Hessels, A Karastergiou, E F Keane, V I Kondratiev, M Kramer, D Michilli, A Noutsos, M Pilia, E J Polzin, B W Stappers, C M Tan, J van Leeuwen, J P W Verbiest, P Weltevrede, G Heald, M I R Alves, E Carretti, T Enßlin, M Haverkorn, M Iacobelli, W Reich, and C Van Eck. Low-frequency Faraday rotation measures towards pulsars using LOFAR: probing the 3D Galactic halo magnetic field. *Monthly Notices of the Royal Astronomical Society*, 484(3):3646–3664, 01 2019. ISSN 0035-8711. doi: 10.1093/mnras/stz214. URL `https://doi.org/10.1093/mnras/stz214`.

B. W. Stappers, J. W. T. Hessels, A. Alexov, K. Anderson, T. Coenen, T. Hassall, A. Karastergiou, V. I. Kondratiev, M. Kramer, J. van Leeuwen, J. D. Mol, A. Noutsos, J. W. Romein, P. Weltevrede, R. Fender, R. A. M. J. Wijers, L. Bähren, M. E. Bell, J. Broderick, E. J. Daw, V. S. Dhillon, J. Eislöffel, H. Falcke, J. Griessmeier, C. Law, S. Markoff, J. C. A. Miller-Jones, B. Scheers, H. Spreeuw, J. Swinbank, S. Ter Veen, M. W. Wise, O. Wucknitz, P. Zarka, J. Anderson, A. Asgekar, I. M. Avruch, R. Beck, P. Bennema, M. J. Bentum, P. Best, J. Bregman, M. Brentjens, R. H. van de Brink, P. C. Broekema, W. N. Brouw, M. Brüggen, A. G. de Bruyn, H. R. Butcher, B. Ciardi, J. Conway, R. J. Dettmar, A. van Duin, J. van Enst, M. Garrett, M. Gerbers, T. Grit, A. Gunst, M. P. van Haarlem, J. P. Hamaker, G. Heald, M. Hoeft, H. Holties, A. Horneffer, L. V. E. Koopmans, G. Kuper, M. Loose, P. Maat, D. McKay-Bukowski, J. P. McKean, G. Miley, R. Morganti, R. Nijboer, J. E. Noordam, M. Norden, H. Olofsson, M. Pandey-Pommier, A. Polatidis, W. Reich, H. Röttgering, A. Schoenmakers, J. Sluman, O. Smirnov, M. Steinmetz, C. G. M. Sterks, M. Tagger, Y. Tang, R. Vermeulen, N. Vermaas, C. Vogt, M. de Vos, S. J. Wijnholds, S. Yatawatta, and A. Zensus. Observing pulsars and fast transients with LOFAR. *Astronomy & Astrophysics*, 530:A80, June 2011. doi: 10.1051/0004-6361/201116681.

X. H. Sun, W. Reich, A. Waelkens, and T. A. Enßlin. Radio observational constraints on Galactic 3D-emission models. *Astronomy & Astrophysics*, 477(2):573–592, January 2008. doi: 10.1051/0004-6361:20078671.

Swinburne University of Technology. Pulsar dispersion measure. `https://astronomy.swin.edu.au/cosmos/p/pulsar+dispersion+measure`. Accessed: 2021-11-05.

J. H. Taylor and J. M. Cordes. Pulsar Distances and the Galactic Distribution of Free Electrons. *The Astrophysical Journal*, 411:674, July 1993. doi: 10.1086/172870.

J. H. Taylor, R. N. Manchester, and A. G. Lyne. Catalog of 558 Pulsars. *The Astrophysical Journal Supplement Series*, 88:529, October 1993. doi: 10.1086/191832.

R. C. Thomson and A. H. Nelson. The interpretation of pulsar rotation measures and the magnetic field of the galaxy. *Monthly Notices of the Royal Astronomical Society*, 191:863–870, June 1980. doi: 10.1093/mnras/191.4.863.

Diego F. Torres, Yousaf M. Butt, and Fernando Camilo. Recently Discovered Pulsars and Unidentified Egret Sources. *Astrophysical Journal Letters*, 560(2):L155–L158, October 2001. doi: 10.1086/324379.

C. L. Van Eck, J. C. Brown, J. M. Stil, K. Rae, S. A. Mao, B. M. Gaensler, A. Shukurov, A. R. Taylor, M. Haverkorn, P. P. Kronberg, and N. M. McClure-Griffiths. Modeling the Magnetic Field in the Galactic Disk Using New Rotation Measure Observations from the Very Large Array. *The Astrophysical Journal*, 728(2):97, February 2011. doi: 10.1088/0004-637X/728/2/97.

W. H. T. Vlemmings. A new probe of magnetic fields during high-mass star formation. Zeeman splitting of 6.7 GHz methanol masers. *Astronomy & Astrophysics*, 484(3):773–781, June 2008. doi: 10.1051/0004-6361:200809447.

J. M. Weisberg, J. M. Cordes, B. Kuan, K. E. Devine, J. T. Green, and D. C. Backer. Arecibo 430 MHz Pulsar Polarimetry: Faraday Rotation Measures and Morphological Classifications. *The Astrophysical Journal Supplement Series*, 150(1):317–341, January 2004. doi: 10.1086/379802.

J. L. West, S. Safi-Harb, T. Jaffe, R. Kothes, T. L. Landecker, and T. Foster. The connection between supernova remnants and the Galactic magnetic field: A global radio study of the axisymmetric sample. *Astronomy & Astrophysics*, 587:A148, March 2016. doi: 10.1051/0004-6361/201527001.

J. M. Yao, R. N. Manchester, and N. Wang. A New Electron-density Model for Estimation of Pulsar and FRB Distances. *The Astrophysical Journal*, 835(1):29, January 2017. doi: 10.3847/1538-4357/835/1/29.

F. Yusef-Zadeh, D. A. Roberts, W. M. Goss, D. A. Frail, and A. J. Green. Detection of 1720 MHz Hydroxl Masers at the Galactic Center: Evidence for Shock-excited Gas and Milligauss Fields. *Astrophysical Journal Letters*, 466:L25, July 1996. doi: 10.1086/310165.

Appendix A

Review of the methodology

This section provides a brief overview of the potential limits of the applied developed methodology. Therefore, it should be treated as an extension of section 5.

Geometric limitations

Geometrically, the analysis evolves around the assumed Solar position at (XX,YY,ZZ) = $(0.0, 8.5\,\mathrm{kpc}, 0.0)$ in Galactocentric coordinates. Thus, the Sun is supposed to lie within the Galactic plane. Studies of e.g., parallax data however suggest a position around (XX,YY,ZZ) = $(0.0, 8.15 \pm 0.15\,\mathrm{kpc}, 5.5 \pm 5.8\,\mathrm{pc})$ (Reid et al., 2019). In terms of vertical position, a relatively small difference to the assumed location, but a potentially significantly different radial distance to the GC of up to 0.5 kpc therefore may exist.

To study different sight lines, pre-defined longitudinal bins are used (see section 3.3). The areal increase that follows from this definition and the resulting possible increased distance between sources within individual bins is already briefly introduced in section 3.3. Due to its major importance for the methodology, it is however developed further here.
One may argue that the definition of the different bins in this way is a necessity regarding the decrease in the number of sources with distance from the Solar position (see section 4.1). Thus, the bins could be seen as "adapting naturally" to the changing conditions. Without this property, an analysis may be largely limited to very local regions.
On the other hand, a large azimuthal and vertical distance between various sources within the same bin may result in questionable relevance of the obtained magnetic field estimates. This limitation is especially relevant for regions with large vertical extension, i.e., other regions than the thin disk region. The sources may not be radially aligned and thus the magnetic field estimation does not proceed along the line of sight as required for the application of RMs.
Both aspects could potentially be improved by means of a more variable or dynamical definition of the individual bins, e.g., with distance, in future applications. It should however be noted that the possibility of introducing an artificial and potentially biased geometry must be considered.

Methods

More method-specific issues are discussed in the following paragraphs.

Method b A notable limitation of Method b is the dependence on two unique pulsars. Thus, the obtained values may depend on small-scale features in vicinity of one of them. Therefore, this method potentially gives more relevant results for comparably small regions or small distances between subsequent pulsars.

Method c Due to the dependence of the possible application of this method on availability of aligned sources, a major limit is set by the Galactic distribution of observed sources. Therefore, the method may unfold its potential once more observations of new sources are available as noted in section 7.

Code availability

The developed code described in this work may be shared on reasonable request to the corresponding author.

Appendix B

Complementary results

Figures concerning additional results for Method a, b, and/or c.

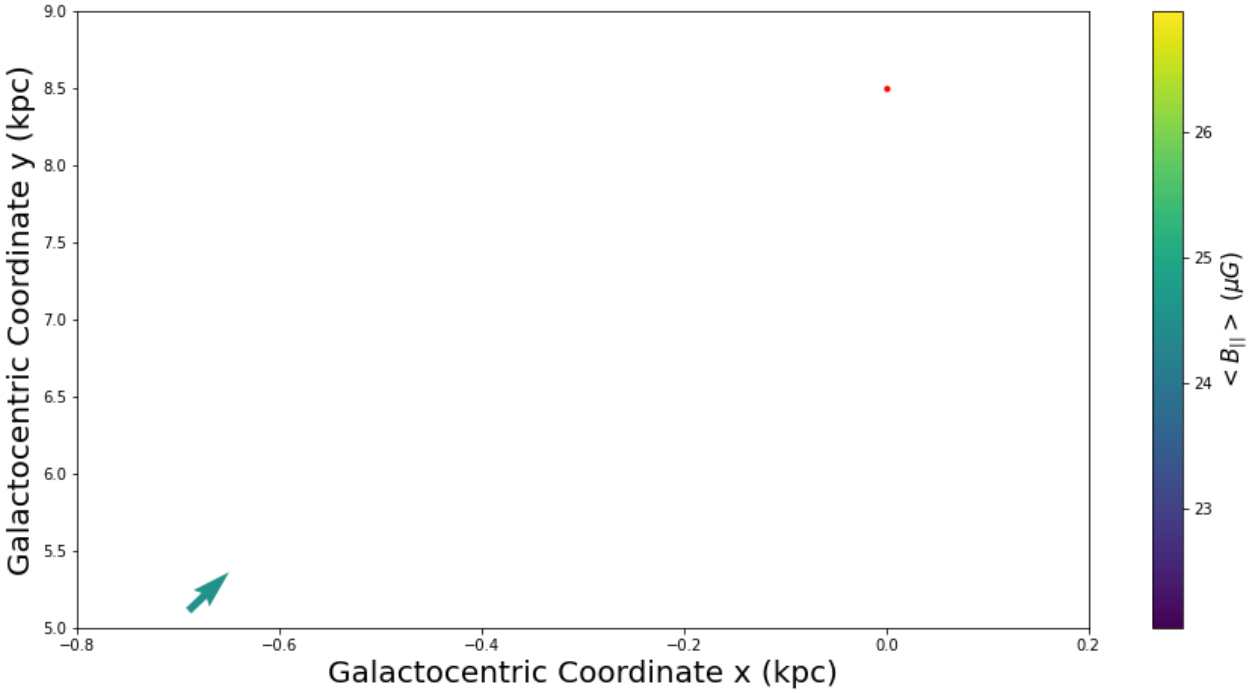

Figure 59: Determined values for the line of sight average magnetic field strength $> 20\,\mu$G for Region 6, Method b.

PSR0	PSR1	$\lvert\langle B_{\parallel}\rangle\rvert$ (µG)	publications
J1837-0559	J1839-0643	22.275	-
J1839-0643	J1842-0612	382.065	-
J1842-0612	J1834-0602	22.207	-
J1838-0453	J1841-0500	43.120	1: Camilo et al. (2012)
B1839-04 / J1842-0359	J1842-0415	42.009	1: no SNR assoc Lorimer et al. (2000)
B1839-04 / J1842-0359	J1841-0345	92.400	0: nr
J1841-0345	B1842-04 / J1845-0434	23.590	0: no SNR assoc Lorimer et al. (2000)
B1842-04 / J1845-0434	J1847-0438	208.756	-
J1843-0211	J1842-0153	20.043	-
B1854+00 / J1857+0057	J1848+0127g	35.223	-
J0627+0706	J0646+0905	46.328	0: Brinkman et al. (2018)
J0901-4624	J0905-4536	45.306	0: nr
J1013-5934	J1016-5857	35.451	1: Klingler et al. (2022)
J1016-5857	B1011-58 / J1012-5857	65.093	0: see previous
J1049-5833	J1043-6116	90.502	-
J1103-6025	J1105-6107	100.992	1: Chadwick et al. (2000)
J1112-6103	B1112-60 / J1114-6100	106.015	0: nr; 1: Johnston et al. (2021)
B1323-62 / J1327-6222	B1323-627 / J1327-6301	21.410	-
B1356-60 / J1359-6038	J1403-6310	81.765	0: Oswald et al. (2020)
J1416-6037	J1412-6111	23.386	-
J1513-5739	J1515-5720	24.866	-
J1638-4608	J1637-4642	125.110	1: Torres et al. (2001)
J1652-1400	J1643-1224	24.726	1: Mall et al. (2022)
J1805-1504	J1808-1517	23.537	-
B1630-44 / J1633-4453	J1637-4450	288.547	-
J1849+0409	J1822+0705	89.806	-
B1055-52 / J1057-5226	J1141-3107	83.502	0: Kerr et al. (2018)
J1349-6130	J1347-5947	21.718	-
J1424-5822	J1434-6006	42.892	-
J1705-3950	B1650-38 / J1653-3838	413.952	0: nr
B0840-48 / J0842-4851	J0901-4624	61.349	1: nr
J1410-6132	J1413-6222	22.239	0: Keith et al. (2008)

Table 6: Sight lines with 'ultra-high' $\lvert\langle B_{\parallel}\rangle\rvert$ estimates (nr = no relevant publications).

List of Figures

List of Tables

List of Abbreviations

CCW = counterclockwise
CW = clockwise
DM = Dispersion Measure
GC = Galactic Centre
GMF = Galactic Magnetic Field
ISM = Interstellar Medium
RM = Rotation Measure